

EFFECTS OF PERTURBATIONS ON SPACE DEBRIS IN SUPERSYNCHRONOUS STORAGE ORBITS

Dr. Kim Luu
Dr. Chris Sabol

October 1998

199905035
SCO 50406661

Final Report

APPROVED FOR PUBLIC RELEASE; DISTRIBUTION IS UNLIMITED.



AIR FORCE RESEARCH LABORATORY
Space Vehicles Directorate
3550 Aberdeen Ave SE
AIR FORCE MATERIEL COMMAND
KIRTLAND AIR FORCE BASE, NM 87117-5776

Using Government drawings, specifications, or other data included in this document for any purpose other than Government procurement does not in any way obligate the U.S. Government. The fact that the Government formulated or supplied the drawings, specifications, or other data, does not license the holder or any other person or corporation; or convey any rights or permission to manufacture, use, or sell any patented invention that may relate to them.

This report has been reviewed by the Public Affairs Office and is releasable to the National Technical Information Service (NTIS). At NTIS, it will be available to the general public, including foreign nationals.

If you change your address, wish to be removed from this mailing list, or your organization no longer employs the addressee, please notify AFRL/VSSS, 3550 Aberdeen Ave SE, Kirtland AFB, NM 87117-5776.

Do not return copies of this report unless contractual obligations or notice on a specific document requires its return.

This report has been approved for publication.

Kim Luu

KIM LUU, Ph.D.
Project Manager

L. Kevin Slimak

L. KEVIN SLIMAK, DR-IV
Chief, Surveillance and Control Division

FOR THE COMMANDER

C. M. Anderson

CHRISTINE M. ANDERSON, SES
Director, Space Vehicles Directorate

REPORT DOCUMENTATION PAGE

*Form Approved
OMB No. 074-0188*

Public reporting burden for this collection of information is estimated to average 1 hour per response, including the time for reviewing instructions, searching existing data sources, gathering and maintaining the data needed, and completing and reviewing this collection of information. Send comments regarding this burden estimate or any other aspect of this collection of information, including suggestions for reducing this burden to Washington Headquarters Services, Directorate for Information Operations and Reports, 1215 Jefferson Davis Highway, Suite 1204, Arlington, VA 22202-4302, and to the Office of Management and Budget, Paperwork Reduction Project (0704-0188), Washington, DC 20503.

1. AGENCY USE ONLY (Leave blank)			2. REPORT DATE October 1998		3. REPORT TYPE AND DATES COVERED Final; August 1995 to August 1998	
4. TITLE AND SUBTITLE Effects of Perturbations on Space Debris in Supersynchronous Storage Orbits			5. FUNDING NUMBERS PE: 62601F PR: 8809 TA: TA WU: 01			
6. AUTHOR(S) Dr. Kim Luu Dr. Chris Sabol						
7. PERFORMING ORGANIZATION NAME(S) AND ADDRESS(ES) AFRL/VSSS 3550 Aberdeen Ave SE Kirtland AFB, NM 87117-5776				8. PERFORMING ORGANIZATION REPORT NUMBER AFRL-VS-PS-TR-1998-1093		
9. SPONSORING / MONITORING AGENCY NAME(S) AND ADDRESS(ES)				10. SPONSORING / MONITORING AGENCY REPORT NUMBER		
11. SUPPLEMENTARY NOTES						
12a. DISTRIBUTION / AVAILABILITY STATEMENT Approved for public release; distribution is unlimited.					12b. DISTRIBUTION CODE	
13. ABSTRACT (Maximum 200 Words) The current mitigation measure supported to address the space debris situation in the geosynchronous (GEO) region is to boost satellites into supersynchronous orbits in the time before stationkeeping fuel is expected to be exhausted. Because this solution does not remove mass from space, debris generation by fragmentation events remains a possibility. This study examines the consequences of collisions in the storage orbits and possible interaction with GEO. Pertinent background information on GEO debris, including summaries of the sources and management strategies, is covered first. Next, the methods and tools by which the effects of collisions can be analyzed are discussed. A low-velocity breakup model is needed to provide the delta-velocities imparted to the fragment debris; a simple hybrid model is applied here. An analytical study of the effects of perturbations, including solar and lunar third body gravitation, Earth oblateness through degree and order four, and solar radiation pressure, follows in order to evaluate the magnitude of these disturbing forces on the fragmentation debris. Validation of these results is achieved by conducting a numerical analysis using proven numerical and semianalytical orbit propagators. The results show that currently practiced reorbiting distances above GEO do not isolate debris from GEO after the occurrence of collisions in storage orbits.						
14. SUBJECT TERMS Space Debris, Orbital Debris, Perturbation Analysis, Mitigation Studies, Risk Assessment, Geosynchronous Earth Orbits					15. NUMBER OF PAGES 124	
					16. PRICE CODE	
17. SECURITY CLASSIFICATION OF REPORT Unclassified		18. SECURITY CLASSIFICATION OF THIS PAGE Unclassified		19. SECURITY CLASSIFICATION OF ABSTRACT Unclassified		20. LIMITATION OF ABSTRACT Unlimited

Contents

1	Introduction	1
1.1	Space Debris in GEO	2
1.2	Physical Characteristics of GEO	3
1.3	Debris Sources	4
1.3.1	Cataloged Objects	4
1.3.2	Uncataloged Objects	5
1.4	Debris Management	6
1.4.1	Passive Methods	6
1.4.2	Active Methods	7
1.5	Summary	10
2	Research Overview	11
2.1	Identification of Problem	11
2.2	Earlier Studies	12
2.2.1	NASA Study	13
2.2.2	NASDA Study	13
2.2.3	ESA Study	15
2.2.4	Remarks and Comparison	16
2.3	Approaches and Tools	17
2.3.1	Low-Velocity Collision Models	17
2.3.2	Analytic Approach	19

2.3.3	Numeric Approach	22
2.4	Chosen Methodology	23
3	Perturbation Models	24
3.1	Equinoctial Elements	24
3.2	Equinoctial Reference Frame	26
3.3	Direction Cosines	27
3.4	Lagrange's Planetary Equations	28
3.5	Geopotential Disturbing Function	29
3.6	Third Body Disturbing Function	32
3.7	Solar Radiation Pressure Disturbing Function	35
4	Perturbation Analysis and Results	37
4.1	General Methodology	37
4.1.1	Formulation of Lagrange's Planetary Equations	37
4.1.2	Analysis of Lagrange's Planetary Equations	39
4.2	Geopotential	42
4.2.1	Geopotential Analysis	44
4.2.2	Geopotential Model Validation	48
4.2.3	Summary of Geopotential Perturbation Effects	54
4.3	Solar Third Body	57
4.3.1	Solar Third Body Analysis	57
4.3.2	Solar Third Body Model Validation	59
4.3.3	Summary of Solar Third Body Perturbation Effects	63
4.4	Lunar Third Body	65
4.4.1	Lunar Third Body Analysis	65
4.4.2	Lunar Third Body Model Validation	66
4.4.3	Summary of Lunar Third Body Perturbation Effects	70
4.5	Solar Radiation Pressure	71

4.5.1	SRP Analysis	71
4.5.2	SRP Model Validation	72
4.5.3	Summary of SRP Perturbation Effects	75
4.6	Cumulative Effects	76
5	Application to the Reorbiting Problem	82
5.1	Breakup Model	82
5.2	Reorbiting Altitudes	86
5.2.1	15 Degrees Inclination Case	87
5.2.2	7.5 Degrees Inclination Case	90
6	Conclusions and Future Work	94
6.1	Conclusions	94
6.2	Future Work	96

List of Figures

3.1	Direct Equinoctial Reference Frame	25
3.2	Geometry of Third Body Perturbations.	33
4.1	Variations from Osculating Values.	41
4.2	Semimajor Axis History for 4x4 and 8x8 Geopotential at GEO.	44
4.3	Eccentricity History for 4x4 and 8x8 Geopotential at GEO.	45
4.4	Geopotential Short-Periodic Variations in Semimajor Axis.	50
4.5	Geopotential Long-Periodic Variations in Semimajor Axis.	51
4.6	Geopotential Short-Periodic Variations in Eccentricity.	52
4.7	Geopotential Long-Periodic Variations in Eccentricity at Zero Inclination.	53
4.8	Geopotential Long-Periodic Variations in Eccentricity at 15° Inclination.	54
4.9	Geopotential Induced Variations in Radial Direction.	55
4.10	Solar Third Body Short-Periodic Variations in Semimajor Axis.	60
4.11	Solar Third Body Short-Periodic Variations in Eccentricity.	61
4.12	Solar Third Body Long-Periodic Variations in Eccentricity.	62
4.13	Solar Third Body Induced Variations in Radial Direction.	63
4.14	Lunar Third Body Short-Periodic Variations in Semimajor Axis.	67
4.15	Lunar Third Body Short-Periodic Variations in Eccentricity.	68
4.16	Lunar Third Body Long-Periodic Variations in Eccentricity.	69
4.17	Lunar Third Body Induced Variations in Radial Direction.	70
4.18	SRP Long-Periodic Variations in Semimajor Axis.	73
4.19	SRP Long Periodic Variations in Eccentricity.	74

4.20 SRP Induced Variations in Radial Direction.	75
4.21 Cumulative Effect: Variations in Radial Direction.	77
4.22 Total Perturbation LP Effects in Semimajor Axis at Zero Inclination.	77
4.23 Total Perturbation LP Effects in Eccentricity at Zero Inclination.	78
4.24 Total Perturbation LP Effects in Semimajor Axis at 15 Degrees Inclination.	79
4.25 Total Perturbation LP Effects in Eccentricity at 15 Degrees Inclination.	80

List of Tables

2.1	GEO Perturbation Effects From NASDA Study.	14
2.2	Comparison of the Reorbiting Equations.	16
4.1	Setting Descriptions for Propagators in Test Case.	43
4.2	Significant Periodic Effects from Geopotential Perturbations.	49
4.3	Analytical Expressions for Significant Geopotential Terms.	56
4.4	Significant Periodic Effects from Solar Third Body Perturbations.	60
4.5	Analytical Expressions for Significant Solar Third Body Terms.	64
4.6	Significant Periodic Effects from Lunar Third Body Perturbations.	67
4.7	Analytical Expressions for Significant Lunar Third Body Terms.	71
4.8	Significant Periodic Effects from SRP Perturbations.	73
4.9	Analytical Expressions for Significant SRP Terms.	76
4.10	Comparison of Models at Different Altitudes.	81
5.1	Data From Collisions Between Objects 15 Degrees Apart.	85
5.2	Data From Collisions Between Objects 7.5 Degrees Apart.	85
5.3	GEO Region Case 1 with Collisions Between Objects 15 Degrees Apart.	87
5.4	GEO Region Case 2 with Collisions Between Objects 15 Degrees Apart.	88
5.5	GEO Region Case 3 with Collisions Between Objects 15 Degrees Apart.	89
5.6	GEO Region Case 1 with Collisions Between Objects 7.5 Degrees Apart.	91
5.7	GEO Region Case 2 with Collisions Between Objects 7.5 Degrees Apart.	92
5.8	GEO Region Case 3 with Collisions Between Objects 7.5 Degrees Apart.	93

6.1 Summary of Reorbiting Analysis.	96
---	----

Executive Summary

The accumulation of space debris in the geosynchronous region (GEO) has raised attention among spacefaring nations. The current mitigation measure supported and voluntarily practiced is to boost satellites into supersynchronous orbits in the time before stationkeeping fuel is expected to be exhausted and to passivate satellites of all stored and generated energy sources to prevent explosions, which are by far the largest source of fragmentation debris. Because this solution does not remove mass from space, debris generation by other fragmentation events remains a possibility. The collision hazard between inactive satellites in the supersynchronous region raises questions about the consequences of collisions in this regime and possible interaction with GEO.

In considering the use of supersynchronous orbits for satellite disposal, the first concern is to determine the minimum safe distance above GEO such that objects in the disposal orbits will not interfere with the GEO population in the future. This involves defining the useful GEO area and studying the perturbation effects on objects in supersynchronous orbits. Thus far, research has focused on propagating the orbits of intact objects. However, in the aftermath of a collision, pieces of varying sizes and shapes can be found in orbits quite different from the parent objects' orbits.

This document summarizes background information on debris in the GEO region, sources and management strategies, and then addresses the following questions: Will orbits of fragments from a collision in a storage orbit occupy GEO altitudes at some time after the collision? If so, at what altitude should the storage orbit occupy such that collision fragments will not interfere with the GEO population? The methods and tools by which the effects of collisions in the supersynchronous region can be analyzed are discussed. A low-velocity collision model is employed to provide delta-velocities imparted to the fragments. An analytical study of perturbation effects, including solar and lunar third body gravitation, Earth oblateness through degree and order four, and solar radiation pressure, follows in order to evaluate the magnitude of these disturbing forces on the fragmentation debris. Validation of these results by numerical analysis using proven numerical and semianalytical

orbit propagators is discussed. The results show that currently practiced reorbiting distances above GEO do not isolate debris from GEO after the occurrence of collisions in the storage orbit.

This report is based on the dissertation work of the primary author which was funded by the Air Force Palace Knight Program. The opinions expressed in this document are those of the author and do not reflect those of the Air Force, the Department of Defense, nor the United States government.

Chapter 1

Introduction

Space debris can be defined as “any man-made Earth-orbiting object which is non-functional with no reasonable expectation of assuming or resuming its intended function or any other function for which it is or can be expected to be authorized, including fragments and parts thereof.” [29] Specifically, orbital debris include [46]

- Nonfunctional spacecraft
- Rocket bodies
- Mission-related debris
 1. Exhaust products
 2. Objects released in spacecraft deployment and operations
 3. Refuse from manned missions
- Fragmentation debris
 1. Explosion fragments
 2. Collision fragments
 3. Products of deterioration

The term orbital debris is often used interchangeably with space debris, as is the case in this writing. It is a subject that is gaining public recognition in recent years, with short articles

now appearing even in local newspapers. Despite its novelty status in the public conscience, orbital debris has been a topic of research for decades now. Space agencies regard it as a space hazard which previously included such things as meteoroids and radiation, problems to be studied and to find protection against. Unlike the other space hazards mentioned, however, debris is man-generated, and therefore, to a certain extent, the debris situation is ours to assess, control, and counteract. The background information on orbital debris is extensive, as it concerns all regions of near-Earth space currently in use. The rest of this introduction briefly summarizes the debris situation in the geosynchronous Earth orbits (GEO) region. This is followed by discussions of debris sources and proposed management schemes.

1.1 Space Debris in GEO

The focus of this research is on the GEO debris environment, which differs on significant points from the situation in low Earth orbits (LEO) as described in this section. The great majority of the cataloged debris is in LEO. Undoubtedly, most debris, cataloged as well as uncataloged, is in LEO due to its extensive use and the wider range of altitudes that comprises LEO. However, at GEO altitudes, only objects larger than 1 m in diameter are regularly tracked and cataloged, whereas 10–50 cm is the limit in LEO [29]; therefore, a whole population of smaller pieces potentially exists in GEO undetected. It is also possible that fragmentation events, especially if the parent objects' orbits do not markedly change and resulting debris are small, occur unnoticed [39].

Another difference is that relative velocity between objects in GEO averages about 500 m/s [26], compared to about 10 km/s for LEO [49]. Since probability of collision is a function of the average relative velocity between objects as well as spatial density, greater attention is directed at LEO, particularly at the crowded 900–1000 km and 1400–1500 km altitude bands [46]. With manned missions currently limited to LEO, a good deal of debris research aims at evaluating the risk to and protecting the Space Shuttle and the planned International Space Station [47]. Finally, the proximity of LEO allows for active retrieval of satellites so that their space-exposed surfaces, which are records of impacts from debris, may be studied. The result of these distinctions is that there are more measurement data and environment models for LEO than for the debris in GEO.

Then, too, atmospheric drag acts as a natural cleanser for parts of LEO. Satellites below 500 km altitude will deorbit within several years [32]. LEO satellites operating above 500 km can reduce their orbital lifetime by reorbiting at end of life (EOL) to lower altitudes or simply by lowering their perigee as appropriate to utilize atmospheric drag. In GEO, orbital lifetimes exceeds thousands of years, and deorbiting is not economically feasible with current technology. Barring great advances in propulsive technology, the population, intact or otherwise, in GEO is more or less permanent. With this difference in mind, debris management strategies for GEO must be tailored to the situation there. The rest of this document discusses only issues pertaining to GEO.

1.2 Physical Characteristics of GEO

The primary distinguishing feature of GEO is that satellites placed there have an orbital period of about 1436.2 min, one sidereal day. A distinction can be made between the geosynchronous region and the particular circular orbits at about 35,786 km altitude and zero inclination, which are referred to as geostationary orbits (GSO). GSO satellites appear to be fixed in the sky over locations on Earth's equator. Consequently, antennas at ground relay stations can be small, nonmoving, high-gain, and low-cost, thus extending satellite coverage to millions of direct users for whom the expense of tracking antennas is out of reach [61]. Satellites in other GEO orbits have "figure eight" groundtracks, which grow larger with higher inclinations. The many uses of GEO include communications, meteorology, and governmental and military support.

Due to tesseral harmonics effects, satellites must perform longitudinal, i.e., east-west, stationkeeping maneuvers to avoid drifting out of GSO. The ellipticity of the Earth's equator produces four equilibrium points in GSO, two stable points at 75.3°E and 255.3°E and two unstable points at 165.3°E and 345.3°E . Uncontrolled satellites migrate toward the stable points. Lunar and solar gravity torque the satellite orbit plane toward the ecliptic [26]; thus, GSO satellites must also perform north-south stationkeeping maneuvers to control inclination. The orbital inclinations of uncontrolled satellites increase from 0° to almost 15° in 27 years and then back to 0° in another 27 years [62]. Long term propagations show radial stability throughout the region, defined as 2000 km above and below GSO altitude [26]. Uncontrolled, intact GEO and GSO objects will

remain in the GEO region for at least several centuries. Due to this, the accumulation of debris is of concern for many GEO operators.

1.3 Debris Sources

The first GEO satellite, Syncom 3, was launched in 1964. It relayed signals to broadcast the Tokyo Olympics to half of the Earth [52]. Within three decades, hundreds of satellites have been placed into GEO with an average of about 25 new payloads per year at present [42]. Along with this population of active and inactive payloads is an assortment of rocket bodies, mission-related debris, and fragmentation debris. GEO objects can be divided into two classes: those that are large enough to be cataloged and those that are not.

1.3.1 Cataloged Objects

Objects that can be identified and regularly tracked are listed in the US Space Command satellite catalog along with their two-line element (TLE) sets. This catalog is not generally available to the public, but portions of it can be obtained through other sources. From the NASA-issued TLE, there were 632 cataloged objects in GEO in March 1997, if GEO is defined by [30]

- eccentricity smaller than 0.1,
- mean motion between 0.9 and 1.1 revolutions per sidereal day, corresponding to a radius of approximately $42,164 \pm 2800$ km, and
- inclination smaller than 20° .

These objects include active and inactive payloads, apogee kick motors, and other propulsive stages. Additionally, there are 40 objects which are listed as geostationary or near-stationary in the *RAE Table of Earth Satellites* but are not in the NASA TLE list [30]. Objects are occasionally mislabeled or lost from tracking.

1.3.2 Uncataloged Objects

Of the smaller debris types, mission-related and fragmentation debris, these are known to exist but cannot be tracked. Solid rocket motors eject large quantities, as many as 10^{20} in a single firing, of aluminum oxide (Al_2O_3) particles. These particles are usually no larger than $10 \mu\text{m}$ in diameter with large area-to-mass ratios. Thus, they are strongly affected by solar radiation pressure, which causes eventual deorbiting [32]. Other mission-related debris too small to be detected are objects released during spacecraft deployment and operations, such as lens covers, shrouds, springs, and explosive bolt pieces. Fragmentation debris also exist. Three explosions have been reported in GEO thus far [67]. One was a USSR Ekran satellite photographed in June 1978 as it exploded from a suspected nickel-hydrogen battery failure [39]. The other events are the explosions of two Titan 2 transtage, including one on 21 Feb 1992 that had been in orbit since 1968 [50]. In general, explosions may be categorized by their causes:

- Propulsion-related
- Deliberate actions
- Accidental detonations
- Electrical failures

It is suspected that more explosions may have occurred unrecorded or unconfirmed [39, 50]. In LEO, explosions have been the most prolific source of cataloged debris. Additionally, long term exposure to radiation and thermal cycling causes loss of flexibility in plastics and polymers which can lead to structural failures and gradual fragmentation [32]. The large number of objects in GEO and their long orbital lifetime form a steady source pool for fragmentation debris. As the number of satellites and fragments increase, accordingly the probability of collisions of every type, i.e., satellite-satellite, satellite-fragment, and fragment-fragment, will increase. Some theorize that beyond a certain average debris flux for a region, the debris environment could reach a state of being self-regenerative [40], although this hypothesis is still the subject of much debate.

1.4 Debris Management

There are no international treaties or laws regulating the growth of orbital debris. However, various spacefaring groups are individually drawing up and enforcing their own debris mitigation guidelines. A survey of industry and civil government agencies and organizations, conducted by the AIAA Orbital Debris Study Group and published in 1992, shows that several groups have voluntarily adopted various methods designed to mitigate the growth of orbital debris. This suggests that there are some debris minimizing techniques with acceptable cost-to-benefit ratios, an important criterion. Unfortunately, the Study Group concluded that current measures are insufficient to control the debris environment [63].

In the following sections, active and passive methods for orbital debris management are described. In particular, it is important to consider the methods' technological maturity and economic feasibility. Debris management aims to minimize risk to satellites directly and indirectly through control of the growth of debris.

1.4.1 Passive Methods

Passive methods are grouped together by one common feature: these methods do not seek to control debris generation. Some passive methods are

- shielding of satellites,
- ground-initiated collision avoidance, and
- on-board collision avoidance systems.

Shielding requirements in the early space-launching days were based on the natural micrometeoroid flux through near-Earth space. The planned International Space Station's shielding now accounts for the debris environment as well as for meteoroids [47]. Likewise, some satellite designers now include debris hazard analysis [4]. However, there is obviously a limit, imposed by economics as well as technology, beyond which additional shielding is not feasible.

The second method uses ground facilities to propagate the orbit of a satellite of interest as well as those of nearby cataloged objects to predict possible collisions. This is practiced by

some satellite operators [58]. Complications arise from uncertainties in the orbit determination and propagation processes as well as the satellite operators' desire to conserve fuel and thus to avoid unnecessary maneuvers. There is also some concern that ground control-initiated avoidance maneuvers cannot be relied upon since only about 10% of the hazardous LEO debris population is cataloged [65]. The situation is likely worse in GEO where typically only objects larger than 1 m in diameter are cataloged.

On-board collision avoidance systems are not technically feasible at present. There are two main problems. First, tracking objects and determining their orbits from a spacecraft present many difficulties. Secondly, it is doubtful whether the spacecraft would have enough time after detection of a possible collision hazard to maneuver out of harm's way [47].

1.4.2 Active Methods

Active methods attempt to directly influence the debris environment. They include

- minimization of space operations debris,
- minimization of risk of explosions,
- reorbiting spacecraft at EOL, and
- active collection or removal.

There are various proposals to decrease space operation debris on future launches. Simple solutions include securing parts, such as shrouds and lens covers, to the spacecraft or rocket body. Other techniques considered are "bagging" fragments from pyrotechnic devices and developing particle-free propellants and explosive bolts. Prelaunch planning of future space operations could include the use of programs such as Collision Avoidance on Launch to reduce the risk of collisions during the mission [63]. The variability of launch times and dates are limited by economic feasibility and mission requirements. Development of new propellants requires time and resources. However, securing parts to the spacecraft is easier to implement and thus has been applied in some cases [49].

To minimize chances for explosions of discarded rocket bodies, an easy, inexpensive, and effective technique is to vent residual fuel and pressurants. This is already widely practiced, but

it is not an established policy by all space agencies or companies. Furthermore, there is already a considerable number of propulsive stages left in orbit by previous missions with residual fuel, and these continue to present an explosion hazard as illustrated by some explosions that have occurred over a decade after the mission was launched [31]. Also, any object left in orbit has the potential to be fragmented by collision.

Inactive payloads form a reservoir of possible sources for fragmentation debris. Disposal or removal of satellites at EOL is more important for GEO where orbit lifetimes extend beyond thousands of years. There are several options for reorbiting from GEO:

- Deorbit
- Escape trajectory
- Stable longitudes
- Stable plane
- Lower altitude
- Raise altitude

Deorbiting GEO spacecraft by current propulsion technology poses unfavorable economic penalties. In fact, for circular orbits above 25,000 km, Earth-escape maneuvers are less expensive than deorbiting maneuvers [51]. Passive devices may be deployed or inflated to increase the area-to-mass ratio which increases the rate of orbital decay, but this raises technical difficulties and also increases probabilities of collision from the enlarged satellite cross-sectional area.

One permanent solution is for active satellites to make a propulsive maneuver at EOL to an Earth-escape trajectory. However, this is a very costly option. An alternative to propulsive burns to escape Earth orbit is the use of solar sails to raise the satellite's altitude. There are technical difficulties in the deployment and control of these solar sails, however, and the technology has not been tested in space. Electric propulsion also has been studied as a feasible means to boost GEO satellites into a heliocentric orbit [57].

In the GSO, there are two stable points, one at 75.3°E, which is over the Indian Ocean and south of Bombay, India, and the other at 255.3°E, which is over the Pacific Ocean and south of Denver, Colorado. Because uncontrolled GEO satellites will migrate toward the closest stable point and continue to oscillate about it with periods of several years, there is some longitudinal bunching about these points. A relatively inexpensive disposal option is to move satellites at EOL to either one of these points. However, objects must be placed with negligible position and velocity errors; small errors in the rendezvous maneuver can result in large oscillations around the stable points [13]. The situation is further complicated by the presence of active satellites in the near vicinity of these points. A collision between dead payloads at the stable points could scatter fragments throughout GEO. Most researchers do not favor this option due to the drawbacks.

For GEO, a “stable” plane exists, inclined 7.4° to the equator [28]. The inclination of satellites launched into this inclined orbit remains within about 1.2° without any stationkeeping. Therefore, relative velocity between satellites in the stable plane is small compared to the average relative velocity between random GEO satellites with inclinations as low as 0° and as high as 15°. The wobbling of the stable plane can be further decreased by placing satellites at specific ascending nodes [33]. Since plane change maneuvers are generally costly, one suggestion is to place satellites into the stable plane at the beginning of their operational lifetime. In doing so, however, the advantages of geostationary, as opposed to geosynchronous, orbits would be lost.

Subsynchronous disposal orbits are another option. The probability of collision decreases as a function of range away from GEO; it is two orders of magnitude less at 100 km below GEO altitude [13]. The major objection to this solution is that disposal orbits below GEO might complicate future launches as new payloads pass through these subsynchronous orbits on their way to GEO.

A cost-effective alternative that has been practiced by several GEO users is to remove the satellites at EOL to supersynchronous storage orbits, also called disposal or graveyard orbits. To place an average-sized GEO spacecraft about 300 km above GEO altitude requires only 5–10 kg of propellant which translates to a 1–2 months reduction in the satellite’s mission lifetime [13]. The probability of collision is then reduced by two- or three-orders of magnitude [42]. This solution

too has difficulties. As the population increases in the disposal orbits, the probability of collisions between inactive payloads increases. Fragments from collisions in storage orbits may be thrown into orbits that intersect GEO. However, this is the only economically feasible option with acceptable drawbacks currently available. Despite this, some feel that disposal orbits are only an intermediate solution [46, 56].

These are self-disposal options, and they are not without risks. There is some danger of malfunction in all propulsive systems and more so for systems that already have been subjected to the harsh, natural environment of space for several years. Further, propellant gauging is often inaccurate, leaving some satellites at EOL with insufficient fuel for the disposal maneuvers. It has been noted that a partially successful disposal maneuver may create a worse situation than none at all [63]. However, to remove inactive GEO satellites that were not reorbited, active retrieval with an orbital maneuvering vehicle or by attaching a propulsion system or a passive device to increase area-to-mass ratio is necessary. The technology required for active retrieval in GEO is available, but it is not cost-effective at the present time.

1.5 Summary

The orbital debris situation in GEO is of particular concern to some. Many feel that keeping collision probabilities low by not augmenting the drifting GEO population is of great importance. Besides the sheer number of GEO objects, their distribution is also a factor. Due to orbital perturbations, the effect of orbital concentration, or bunching, at certain longitudes is already significant [14]. Satellite retrieval or disposal after their active lifetime is presently not practicable in GEO. Therefore, active EOL disposal schemes are the only economically feasible option at the present, but none are consistently practiced by all launching groups.

Chapter 2

Research Overview

Since there are no natural sinks for debris in GEO, the accumulation of inactive satellites and other operational debris in this valuable regime has raised particular concern among the many and diverse GEO satellite operators. The practice of raising the altitude of satellites, placing them out of GEO before stationkeeping fuel is expected to be depleted, is mainly for the purpose of maintaining continuous operation, but it is also a cost-effective mitigation measure that many operators are voluntarily implementing. One immediate drawback is that the usage of supersynchronous orbits (SSO) as a storage area for debris may preclude future plans to utilize it in a more productive manner. However, future technology may allow for different and more permanent mitigation measures for GEO and perhaps even for active removal of debris from GEO and SSO, if the need arises.

2.1 Identification of Problem

In considering the extensive use of SSO for satellite disposal, the first concern is to determine the minimum safe distance above GEO such that objects in the disposal orbits will not interfere with the GEO population in the future. This involves both defining the useful GEO area and studying the perturbation effects on objects in SSO. Since there are numerous uncontrolled objects in GEO as well, perturbation analysis for these objects is also relevant. Various reorbiting guidelines have been proposed by different spacefaring nations and agencies.

Previous studies have focused on propagating the orbits of intact objects in GEO and SSO. However, in the aftermath of a collision in SSO, pieces of varying sizes and shapes can be found in orbits quite different from the parent objects' orbits. Depending on the altitude of the parent objects in the storage orbits before the breakup, these pieces may intersect GEO by the impact of the collision, or subsequent perturbing forces over time may cause the pieces to mingle with the GEO population.

This research examines the aftermath of collisions in SSO, and in particular, the orbits of the fragmentation debris. A typical reorbiting altitude is selected to determine the semimajor axis of the parent objects' orbits, assumed circular. Since collisions produce a wide variety of debris sizes and shapes, an average piece is chosen such that studies of the orbit of this one representative piece will provide insight into the relative spatial distributions of smaller and larger fragmentation debris. Searching for a worst case scenario, the orbit of this fragment is analyzed to determine if at some point after the collision it will drift into some part of the GEO region. Reiterating this process with varying reorbiting altitudes will determine a minimum altitude for the storage orbits such that an unacceptable fraction of the collision fragments will not interfere with the GEO population.

2.2 Earlier Studies

The effects of orbit perturbations in the GEO region have been well-studied for many purposes. A main concern of satellite operators is determining the necessary stationkeeping maneuvers and the amount of fuel required. For orbital debris analysis, the motion of uncontrolled satellites is important in estimating collision hazards and predicting trends based on the rates of orbital decay, key components of environmental models.

By the early 1980s, various GEO operators had established policies for reorbiting at EOL [61]. These reorbiting guidelines, however, differ among the satellite operators, and in some cases, they differ significantly [13, 60]. Other policies do not specify the reorbiting altitude but instead prescribe conditions upon which the reorbiting altitude may be calculated as appropriate for individual satellites. The Russian Space Agency, for instance, requires only that reorbited spacecraft be placed such that it will not approach GEO any closer than 200 km [1]. As more studies

are conducted and published, movement toward consensus on reorbiting altitudes, given either as a fixed number for all cases or as an expression with variables that are influenced by individual spacecraft characteristics, may be possible. Many now support 300 km as the minimum reorbiting distance [46, 13]. Three agencies have published detailed studies leading to their guidelines which are summarized in this section. These studies mostly have focused on defining the useful GEO area and then finding the minimum altitude above it such that debris in the disposal orbit will not likely interact with the GEO population.

2.2.1 NASA Study

The NASA Safety Standard [45] defines the GEO region as 300 km above and below 35,788 km altitude. The region above 36,088 km altitude is designated as the disposal region for GEO satellites. The Safety Standard and a study by Loftus [41] conclude that the perigee altitude in the storage orbit should be at least

$$\text{GEO} + 300 \text{ km} + 2,000 \text{ km kg/m}^2 \times A/m \quad (2.1)$$

with the area-to-mass ratio in m^2/kg . The first term accounts for perturbations at GEO (50 km) and at the disposal orbit (50 km), operational excursions (50 km), imperfect insertion at the disposal orbit (50 km), and a safety margin (100 km). The second term is the varying effects of solar radiation pressure (SRP) which depends on the objects' area-to-mass ratio.

2.2.2 NASDA Study

Currently, NASDA requires reorbiting by 150 km beyond GEO but targets a desired reorbiting distance of 500 km [35, 36]. However, perturbation studies [34] have led to working expressions for reorbiting distances based on individual satellite characteristics:

$$\Delta a = 186 \text{ km} + 0.011 \text{ kg/m}^2 \times a \times C_r \times A/m \quad (2.2)$$

where

$$\Delta a = \text{reorbiting distance (km)}$$

Table 2.1: GEO Perturbation Effects From NASDA Study.

Perturbation Source	Radial Variation
Earth oblateness	35 km
Solar third body	53 km
SRP	45 km
Total	133 km

a = semimajor axis of the disposal orbit (km)

C_r = radiation pressure coefficient of the satellite

A = effective cross-sectional area (m^2)

m = satellite mass (kg)

This equation is explained as follows. The 186 km in Equation 2.2 is the sum of the radial variation that a GEO satellite experiences due to all perturbations, as detailed in Table 2.1, and the radial variation for a reorbited satellite in SSO due to solar gravitation (53 km). Also in SSO, Earth oblateness is a much smaller effect because the resonance between the rotation of the Earth and the mean motion of the satellite is shallow; thus, the NASDA study allots 0 km in radial variation for Earth oblateness in SSO. The entire second term accounts for the effects of SRP on a reorbited satellite. The values in Table 2.1 were computed using the following conditions:

$$e \text{ (eccentricity)} = 0.001$$

$$A/m = 0.005 \text{ m}^2/\text{kg}$$

$$C_r = 1.5$$

This equation has since been revised [35, 36]. The new expression is

$$\Delta a = 200 \text{ km} + 0.022 \text{ kg/m}^2 \times a \times C_r \times A/m \quad (2.3)$$

While reasons for the 14 km increase in the first term were not explicitly stated, variations in assumed satellite orbital elements, namely semimajor axis and eccentricity, will explain it. The

additional factor of 2 in the second term is to account for the long term variation in the eccentricity vector. The original expression only accounted for the yearly variation in eccentricity vector.

2.2.3 ESA Study

An ESA study [5] suggests radial limits of 50 km above and below geosynchronous altitude to define the boundaries of GEO. This definition is based on the actual radial variations of controlled satellites in GEO. The initial formula given for calculating reorbiting distance to null the collision rate over 20 years, as explained further in Reference [5], is

$$da = 1271 \text{ kg/m}^2 A_e + 56 \text{ km} \quad (2.4)$$

in which da is the minimum reorbiting distance above GEO in km and A_e is the effective area-to-mass ratio in m^2/kg . The formula is explained, as follows. $1271 A_e$ accounts for radial variations due to SRP ($\pm 928 A_e$ km) and the coupling effects of SRP and the gravitational forces of Earth and the Moon on the motion of the eccentricity vector ($\pm 343 A_e$ km). The 56 km is the sum of the width of a 0.1° GSO ring (37 km) and 19 km to account for the perturbing effects of Earth and the Moon. Recognizing that the eccentricity variation might exceed the aforementioned bounds after 20 years, a final formula with additional buffers is given:

$$da = 1600 \text{ kg/m}^2 A_e + 65 \text{ km} \quad (2.5)$$

No additional explanation is given to account for this revision.

More recently, Flury [22] states that ESA recommends a minimum reorbiting distance above GEO of 300 km. This number is primarily based on perturbation effects in SSO. The small perturbations, Earth's gravity (J_2 , etc.) and third body effects (solar and lunar) cause a ± 30 km variation while SRP effects vary with area-to-mass ratio. For $A/m = 0.1 \text{ m}^2/\text{kg}$, a very conservative value, the total radial variation due to all perturbations is ± 200 km. Smaller area-to-mass ratios result in smaller variations. Therefore, 300 km is deemed to be enough to account for all perturbations acting on most, if not all, GEO-type spacecraft and includes a 100 km buffer zone. The buffer covers GEO perturbations for uncontrolled objects and the operational zone for active satellites.

Table 2.2: Comparison of the Reorbiting Equations.

Study	NASA	NASDA	ESA
Year	1992	1996	1996
GEO Perturbations			
Geopotential		35	
Third Body		53 (solar)	
SRP		45	
GEO Total	50	133	100
SSO Perturbations			
Geopotential	50	0	30
Third Body		53 (solar)	
SRP	20	11	7
SSO Total	70	64	37
Other	200	14	0
Reorbiting Distance	320 km	211 km	137 km

2.2.4 Remarks and Comparison

To compare the reorbiting equations with ESA's flat 300 km recommended distance, values for some quantities are assumed. For an average area-to-mass ratio of $0.01 \text{ m}^2/\text{kg}$, Loftus's formula, Equation 2.1, gives 320 km as the appropriate distance to reorbit. The latest NASDA formula, Equation 2.3, gives about 211 km for the same area-to-mass ratio, $C_r = 1.2$, and $a = 42,377 \text{ km}$. Loftus's guideline is noticeably more conservative but also closer to the 300 km recommendation.

Next, compare the individual components of the reorbiting equations as far as possible. In particular, each perturbation effect is separated out to gain further insight on the differences between independent studies. Table 2.2 summarizes the studies discussed above with $A/m = 0.01 \text{ m}^2/\text{kg}$, $a = 42,377 \text{ km}$, and $C_r = 1.2$. Distances are radial and in km.

Table 2.2 is missing some numbers that could not be deduced from the published studies so it is difficult to focus on specifics. The studies differ on GEO perturbations by 83 km, while SSO totals are within 33 km. It is possible that another independent study will help in understanding these discrepancies. Note that the reorbiting distances, as reflected in this table, are based on specific area-to-mass ratios. Some studies prefer to use an extremely conservative value and then recommend one reorbiting distance for all satellites. Others leave the final distance up to the satellite operators to choose based on information for individual satellites. Finally, note that objects are assumed to remain intact in these studies.

2.3 Approaches and Tools

This section outlines possible methods and tools to study the effects of collisions in SSO. Although this research employed one particular method, alternatives are described to provide ideas for refinement of this work in the future. One part of this problem involves using a low-velocity collision model to obtain the typical fragment characteristics and delta-velocities imparted to the fragments. Currently, low-velocity models are few, and those in existence have incorporated little, if any, empirical data, which is even more scarce. The collision model provides an idea of the initial orbits of the fragments; the other major piece of the puzzle is determining the evolution of these orbits over time. One approach is to conduct an analytic study on the effects of perturbations on the breakup pieces to gauge the extent, if any, to which the breakup debris will inhabit the GEO region. The varying parameter is the altitude at which the breakup that produced these fragments occurred. From the results, a minimum reorbiting distance above GEO can be approximated. The perturbation studies can also be carried out numerically, but searching for the worst-case scenario involves methodical guessing of the initial orbit orientation since the breakup model would at most provide only information on semimajor axis and eccentricity.

2.3.1 Low-Velocity Collision Models

An important tool in studying this problem is a collision model for the SSO regime. In particular, information on the typical characteristics of and delta-velocities imparted to the fragments

produced from nonhypervelocity collisions is desired. The direction of the delta-velocities is often assigned randomly; consequently, the delta-velocity can be applied in the direction that produces a new orbit with minimal radial distance, since the worst possible case is desired. Unfortunately, the vast majority of research in impact breakup modeling centers on hypervelocity collisions associated with objects in LEO. Most ground test and on-orbit breakup data are also geared for the hypervelocity regime. The first decision then is whether to develop a new collision model for use in this study or to try to utilize one of the few largely unvalidated models available. The few documented GEO models are discussed next.

Long term evolution programs for GEO generally include nonhypervelocity collision models as a source of debris generation from the on-orbit population. Logically then, searching for appropriate collision models begins with GEO environmental models. One such program, developed at the University of Colorado, is ODESI, which includes two nonhypervelocity collision models [43]. The first is a simplistic spherical model that is statistically-based. Assuming that users have good data for the number of fragments produced and the delta-velocities imparted, the model breaks the parent object up in equal-sized pieces and randomly generates directions for the delta-velocities. For the velocity imparted to breakup fragments, this is usually determined using on-orbit breakup data. That is, with knowledge of the orbits of the breakup pieces and also of the parent object's orbit before impact, delta-velocities can be estimated. However, it is unlikely that a large number of fragments from GEO or SSO collisions could be detected or tracked. With no better numbers readily available, the study assumed delta-velocities that were equal to the relative velocities between the colliding objects. The second model is a finite element approach, using the general purpose MSC/NASTRAN program in conjunction with MSC/DYTRAN to simulate the dynamic, nonlinear behavior of spacecraft material. The results from this model depend heavily on the grid size employed; fragments produced cannot be smaller than the element grid size. The published study includes results from a 0.5 cm grid and using one specific GEO satellite. It has not been determined whether a smaller grid size would be more appropriate. Moreover, this model does not provide the velocities imparted to the fragments.

Another model was developed at the NTT Radio Communication Systems Laboratory in Yokosuka, Japan. Fragment mass distribution may be chosen to be either uniform or following a power law, similar to hypervelocity cases. Some low velocity impact tests performed suggests that mass distribution is well modeled by the power law distribution [68]. The velocity distribution can then be generated numerically using a model based on the principle of conservation of momentum and energy [69]. Experimental results on the velocity distribution are pending.

2.3.2 Analytic Approach

To determine a suitable storage altitude in SSO, two questions are considered:

- What is the maximum altitude traversed by typical GEO objects, operational as well as uncontrolled?
- What is the minimum altitude reached by an object ejected from a collision in the storage orbit?

The first concerns the definition of a GEO region, the protection of which is the primary motivation. The answer partly depends on the activities of operational satellites and is found in some the earlier studies of GEO reorbiting requirements.

For the uncontrolled objects, study begins by examining the equation of motion for a two-body system with perturbations:

$$\ddot{\vec{r}} = -\frac{\mu}{r^3} \vec{r} + \vec{f}_p \quad (2.6)$$

for which

$\ddot{\vec{r}}$ = second derivative of position vector with respect to time

\vec{r} = position vector of the satellite with origin at center of Earth

μ = gravitational parameter of central body

$\approx Gm_{\oplus}$

\vec{f}_p = perturbing acceleration per mass unit

Perturbations may also be studied from a n-body approach, but anticipated difficulties are many. Variation of parameters (VOP) is the usual tool selected to manage Equation 2.6, and for this, there is the choice of classical Lagrangian VOP, Gaussian VOP, and Hamiltonian VOP. The last requires some familiarity with Hamiltonian mechanics. Variation of coordinates, also known as Encke's method, is another option [15].

The perturbing acceleration is the sum of individual accelerations from several sources. Objects in GEO and SSO are heavily influenced by the following perturbations:

- Earth gravity harmonics
- Third body gravitation, solar and lunar
- Solar radiation pressure

Earth gravity harmonics are the terms of a mathematical expansion representing the Earth's deviations from a perfect sphere. The largest terms of the zonal and tesseral harmonics are J_2 and J_{22} , respectively. J_2 arises from Earth equatorial oblateness and causes secular variations in the right ascension of the ascending node and the argument of perigee. J_{22} is associated with the ellipticity of the Earth equatorial plane. This generates the long term (860-day) oscillation of geosynchronous satellites which can be counteracted by periodic stationkeeping maneuvers. While J_2 effects are much more pronounced than lunar and solar gravitational perturbation at low altitudes, the effects of each are about even in GEO.

Earth satellites are affected by the gravitational attractions of other celestial bodies in the solar system. The perturbation, or acceleration, is proportional to the mass of the perturbing body and inversely proportional to the distance between the body and the satellite. Lunar gravitational perturbations are significant because the Moon, though small in mass relative to nearby planets, is the closest body to the Earth-satellite system. Conversely, the Sun's perturbing effects are important due to its great mass. The net result is a precession of the satellite's orbit about an axis normal to the perturbing body's orbital plane. Lunar and solar effects are significant for orbits at high altitudes and those with periods greater than 12 hours [15].

Solar radiation pressure (SRP) induces the yearly variations in eccentricity and argument of perigee for GEO satellites due to the apparent annual motion of the Sun [64]. Eccentricity may vary from 0.001 to 0.004 in six months [15]. The effect is proportional to the satellite's effective area and surface reflectivity and is inversely proportional to satellite mass. Very small particles, such as micrometeoroids and solid rocket effluents, with larger area-to-mass ratios are strongly influenced by this perturbation force.

Equations of motion have been developed for the gravitational effects of Earth's asphericity and nonuniformity in terms of the classic Keplerian elements in the works of Kaula and others [37, 38]. However, in working with near-circular and low inclination orbits, such as those of most objects in GEO and the storage orbits, a nonsingular set of orbital elements may be more appropriate. There are many nonsingular sets available [64], but the equations of motion and perturbing accelerations will need to be derived in the new coordinates. Several published papers feature development of the desired expressions in nonsingular equinoctial elements [8, 10, 11] and other nonsingular sets [44].

Two approaches to determine the maximum periodic effects predicted by the equations of motion are described. The first is a frequency-independent method in which the amplitudes of the periodic effects from each perturbation are simply summed without regard to the various effects' periodic phasing. Special care must be taken to understand the frequency of the periodics when combining the effects to properly calculate the maximum change in satellite altitude. This approach is the more conservative of the two proposed. The second method accounts for the phasing differences in the periodic effects. This approach attempts to maximize the radial rate of change by searching over the orbit orientation elements. A symbolic manipulator software package can be employed to help with the mathematics. Then, based upon the frequencies and phasing of the periodics, the maximum change in radial amplitude can be deduced. These are idealistic ways to deal with very complicated expressions. In practice, methodologies need not completely disregard phasing, but at the opposite end, accounting for all phasing effects may be impractical. For an initial study, something between most desirable and sufficient is appropriate.

Once the maximum altitude of the GEO region and the minimum altitude of objects ejected from SSO collisions are determined, the storage altitude can be evaluated. This altitude is the key parameter to vary in an iterative manner to determine the minimum safe reorbiting distance above GEO.

2.3.3 Numeric Approach

For this problem, a numeric approach can be undertaken as an independent study or in conjunction with an analytic part. Discussion of the latter follows first. Validation of analytic results can be achieved by conducting a numeric analysis using a proven orbit propagator. While special perturbation methods are often the preferred choice for high accuracy numerical studies, they may not be the best choice in this case since individual periodic effects cannot be easily isolated nor broken down into short- and long-periodic components. This is an important capability so that each part of the analytic work can be thoroughly checked. While selecting a propagator, this should be kept in mind.

The other numerical approach can be performed without the analytic portion. This is an important option should analytic approaches fail to give satisfactory results. In this strictly numeric scenario, a genetic search algorithm can be employed with an orbit propagator to determine the minimum radial distance of fragments resulting from collisions in the storage orbit. The search algorithm propagates a set of elements from an element set family prescribed by the breakup model and storage altitude to find the orbit orientation that produces the lowest possible altitude, i.e., to find the worst case scenario. A concern here is the length of time to propagate these orbits. Physics ensure that debris with moderate area-to-mass ratios will reside in the GEO region and SSO for a great many years. However, technology advances in the next 50 years or so may enable the practice of different mitigation measures. It therefore seems unnecessary to look beyond this time frame. So again, special perturbation methods may not be the ideal choice here due to concerns over computation time and efficiency. Semianalytic propagators should be considered for their advantage in this area. It is anticipated that this strictly numeric approach requires significant computing power. Genetic search algorithm may need to be implemented with propagators using

high performance parallel virtual machine architecture [66]. This could be a desirable option if a strictly numerical approach is pursued.

2.4 Chosen Methodology

This research employs an analytic approach complemented with numerical results for validation. The analysis uses a variation of parameters formulation in nonsingular equinoctial elements, the specifics of which are summarized in Chapter 3. SRP is treated like a conservative force with the assumption that objects are continuously sunlit. Some frequency-independent assumptions are made. The analytical study will provide greater physical insight on the perturbation sources and effects than a completely numeric approach. It will also be more general so that it can be applied to a variety of scenarios. For the complementary numerical part, the Cowell numerical integrator and the semianalytic propagator, Draper Semianalytic Satellite Theory (DSST), both contained in the Draper R & D version of the Goddard Trajectory Determination System, were chosen. The Cowell propagator is useful for checking short periodic variations. For longer integration runs, the DSST averaged orbit generator is employed because it allows for specific model tailoring with accuracy comparable to special perturbation methods [7]. The equations of motion in DSST are decomposed into short- and long-periodic contributions with the amount of force modeling configurable at run time [18, 23]. Thus, isolation of the periodic effects is possible.

It is hoped that a clearer understanding of the effects of perturbations on objects in GEO and SSO will be obtained. The end objective is to provide more information for the selection of storage orbits. The uniqueness of this study lies in the inclusion of SSO breakup modeling as a deciding factor. Preliminary studies, using hypervelocity breakup models, suggest that breakups in currently proposed SSO might well be a hazard to GEO [39].

Chapter 3

Perturbation Models

The perturbation models utilized in this research are presented in this chapter. In consideration of space, relevance, and usefulness, only the final, working expressions for Lagrange's Planetary Equations and the various disturbing functions are included here; for detailed derivations, the reader is referred to the listed references. For this background material, the primary reference is Danielson [19], which summarizes the mathematical groundwork for the Draper Semianalytic Satellite Theory (DSST). A large deviation from DSST is that this study does not use the single- and double-averaging techniques employed by DSST. Since averaging can be a tricky and arduous task and it was deemed unnecessary, this study did not employ averaging techniques.

The choice of orbital elements was made based on the class of orbits to be examined: nearly circular with low inclinations in the GEO region. Hence, a nonsingular set is preferred, and of the various sets of nonsingular elements, equinoctial elements were selected. A very tangible advantage of this particular orbital element set is the fact that the perturbation theory based on equinoctial elements has been well-developed, tested, widely published, and implemented in the semianalytic propagator based on DSST.

3.1 Equinoctial Elements

This section provides a brief introduction to the equinoctial elements, with definitions and their relationship to the familiar Keplerian elements. The equinoctial elements are a , h , k , p , q , and

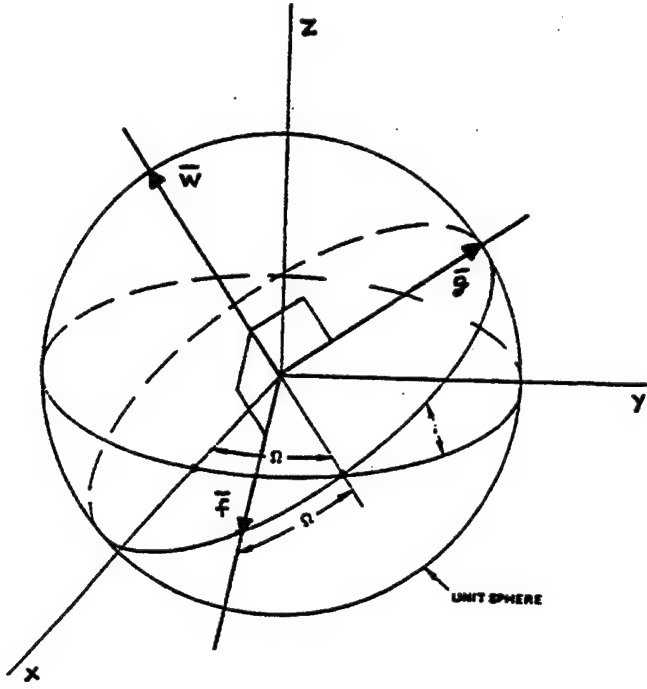


Figure 3.1: Direct Equinoctial Reference Frame

λ . Associated with this orbital set is an equinoctial reference frame $(\hat{f}, \hat{g}, \hat{w})$, which is reproduced in Figure 3.1 from Reference [19] for the direct equinoctial elements. Element a represents semimajor axis, same as in the Keplerian set. Elements k and h are the \hat{f} and \hat{g} components, respectively, of the eccentricity vector, while q and p are the \hat{f} and \hat{g} components, respectively, of the ascending node vector in the equinoctial reference frame. The eccentricity vector points to periapse from the center of mass of the central body and has magnitude equal to the eccentricity of the satellite orbit. Likewise, the ascending node vector points to the ascending node from the central body, with magnitude depending on inclination. The final orbital element is the mean longitude λ .

The conversion from Keplerian to equinoctial elements is given by

$$a = a \quad (3.1)$$

$$h = e \sin(\omega + I\Omega) \quad (3.2)$$

$$k = e \cos(\omega + I\Omega) \quad (3.3)$$

$$p = \left[\tan\left(\frac{i}{2}\right) \right]^I \sin \Omega \quad (3.4)$$

$$q = \left[\tan\left(\frac{i}{2}\right) \right]^I \cos \Omega \quad (3.5)$$

$$\lambda = M + \omega + I\Omega \quad (3.6)$$

where I is the retrograde factor, defined by

$$I = \begin{cases} +1 & \text{for direct equinoctial elements} \\ -1 & \text{for retrograde equinoctial elements} \end{cases} \quad (3.7)$$

It is useful to have also the reverse conversion. Begin by computing an auxiliary angle, ζ :

$$\sin \zeta = \frac{h}{\sqrt{h^2 + k^2}} \quad (3.8)$$

$$\cos \zeta = \frac{k}{\sqrt{h^2 + k^2}} \quad (3.9)$$

Then proceed with

$$a = a \quad (3.10)$$

$$e = \sqrt{h^2 + k^2} \quad (3.11)$$

$$i = \pi \left(\frac{1-I}{2} \right) + 2I \arctan \sqrt{p^2 + q^2} \quad (3.12)$$

$$\sin \Omega = \frac{p}{\sqrt{p^2 + q^2}} \quad (3.13)$$

$$\cos \Omega = \frac{q}{\sqrt{p^2 + q^2}} \quad (3.14)$$

$$\omega = \zeta - I\Omega \quad (3.15)$$

$$M = \lambda - \zeta \quad (3.16)$$

3.2 Equinoctial Reference Frame

From Figure 3.1 on page 25, it is easy to see the main defining points of the equinoctial reference frame:

- $\hat{\mathbf{f}}$ and $\hat{\mathbf{g}}$ are in the satellite orbital plane.
- $\hat{\mathbf{w}}$ is perpendicular to the orbital plane and parallel to the angular momentum vector.
- The right ascension of the ascending node is equal to the angle between $\hat{\mathbf{f}}$ and the ascending node.

Quantitatively, the components of the equinoctial frame basis vectors ($\hat{\mathbf{f}}$, $\hat{\mathbf{g}}$, $\hat{\mathbf{w}}$) in the Earth-centered, nonrotating coordinate system (x, y, z) are given by

$$\hat{\mathbf{f}} = \frac{1}{1+p^2+q^2} \begin{bmatrix} 1-p^2+q^2 \\ 2pq \\ -2Ip \end{bmatrix} \quad (3.17)$$

$$\hat{\mathbf{g}} = \frac{1}{1+p^2+q^2} \begin{bmatrix} 2Ipq \\ (1+p^2-q^2)I \\ 2q \end{bmatrix} \quad (3.18)$$

$$\hat{\mathbf{w}} = \frac{1}{1+p^2+q^2} \begin{bmatrix} 2p \\ -2q \\ (1-p^2-q^2)I \end{bmatrix} \quad (3.19)$$

3.3 Direction Cosines

The expressions for the disturbing forces contain direction cosines as a matter of convenience and tidiness. These are defined by

$$\alpha = \hat{\mathbf{z}}_B \cdot \hat{\mathbf{f}} \quad (3.20)$$

$$\beta = \hat{\mathbf{z}}_B \cdot \hat{\mathbf{g}} \quad (3.21)$$

$$\gamma = \hat{\mathbf{z}}_B \cdot \hat{\mathbf{w}} \quad (3.22)$$

where $\hat{\mathbf{z}}_B$ is the unit vector from the center of mass of the central body to its geographic north pole in the geopotential disturbing function. For third body perturbations, $\hat{\mathbf{z}}_B$ points from the central body to the third body. In the case of solar radiation pressure, for which a disturbing function does exist given the assumption of the satellite being always sunlit, $\hat{\mathbf{z}}_B$ points to the Sun from the central body. Additionally, the direction cosines are related by

$$\alpha^2 + \beta^2 + \gamma^2 = 1 \quad (3.23)$$

3.4 Lagrange's Planetary Equations

Variation of parameters is a method to study the disturbed motion of two bodies. As developed by Lagrange, perturbations modify two-body motion by

$$\frac{d\mathbf{r}}{dt} = \mathbf{v} \quad (3.24)$$

$$\frac{d\mathbf{v}}{dt} + \frac{\mu}{r^3} \mathbf{r} = \left[\frac{\partial \mathcal{R}}{\partial \mathbf{r}} \right]^T \quad (3.25)$$

where \mathcal{R} is the disturbing potential function. Lagrange's Planetary Equations are derived from the above equations. Battin [3, pages 476–484] presents a rigorous derivation of the Planetary Equations using Keplerian elements. This process, when repeated for equinoctial elements, remains essentially unchanged, aside from the use of Poisson brackets instead of Lagrangian brackets [19].

Expressed in equinoctial elements, Lagrange's Planetary Equations are

$$\dot{a} = \frac{2a \partial \mathcal{R}}{A \partial \lambda} \quad (3.26)$$

$$\dot{h} = \frac{B \partial \mathcal{R}}{A \partial k} + \frac{k}{AB} (p \mathcal{R}_{,\alpha\gamma} - Iq \mathcal{R}_{,\beta\gamma}) - \frac{hB}{A(1+B)} \frac{\partial \mathcal{R}}{\partial \lambda} \quad (3.27)$$

$$\dot{k} = -\frac{B \partial \mathcal{R}}{A \partial h} - \frac{h}{AB} (p \mathcal{R}_{,\alpha\gamma} - Iq \mathcal{R}_{,\beta\gamma}) - \frac{kB}{A(1+B)} \frac{\partial \mathcal{R}}{\partial \lambda} \quad (3.28)$$

$$\dot{p} = \frac{C}{2AB} \left[p \left(\mathcal{R}_{,hk} - \mathcal{R}_{,\alpha\beta} - \frac{\partial \mathcal{R}}{\partial \lambda} \right) - \mathcal{R}_{,\beta\gamma} \right] \quad (3.29)$$

$$\dot{q} = \frac{C}{2AB} \left[q \left(\mathcal{R}_{,hk} - \mathcal{R}_{,\alpha\beta} - \frac{\partial \mathcal{R}}{\partial \lambda} \right) - I \mathcal{R}_{,\alpha\gamma} \right] \quad (3.30)$$

$$\dot{\lambda} = -\frac{2a \partial \mathcal{R}}{A \partial a} + \frac{B}{A(1+B)} \left(h \frac{\partial \mathcal{R}}{\partial h} + k \frac{\partial \mathcal{R}}{\partial k} \right) + \frac{1}{AB} (p \mathcal{R}_{,\alpha\gamma} - Iq \mathcal{R}_{,\beta\gamma}) \quad (3.31)$$

where

$$A = \sqrt{\mu a} \quad (3.32)$$

$$B = \sqrt{1 - h^2 - k^2} \quad (3.33)$$

$$C = 1 + p^2 + q^2 \quad (3.34)$$

and the cross-derivative operator is defined by

$$\mathcal{R}_{,\zeta\xi} \equiv \zeta \frac{\partial \mathcal{R}}{\partial \xi} - \xi \frac{\partial \mathcal{R}}{\partial \zeta} \quad (3.35)$$

3.5 Geopotential Disturbing Function

The familiar expression for the geopotential is

$$\mathcal{R}(r, \phi, \psi) = \frac{\mu}{r} \sum_{n=2}^N \sum_{m=0}^{\min(n, M)} \left(\frac{R_{\oplus}}{r} \right)^n P_{nm}(\sin \phi) (C_{nm} \cos m\psi + S_{nm} \sin m\psi) \quad (3.36)$$

where

- μ = gravitational constant of central body
- r = radial distance from central body to satellite
- N = maximum degree
- M = maximum order ($M \leq N$)
- R_{\oplus} = mean equatorial radius of central body
- P_{nm} = associated Legendre function of order m and degree n
- ϕ = geocentric latitude
- C_{nm}, S_{nm} = gravitational coefficients
- ψ = geographic longitude

The conversion of this expression into equinoctial elements involves writing the equation in complex form and two Fourier series expansions, one in true longitude and the other in mean longitude. Danielson [19] goes through the basic derivations steps. Further details that may be helpful are contained in various conference papers [8, 54]. The final product is

$$\mathcal{R} = \operatorname{Re} \left\{ \frac{\mu}{a} \sum_{j=-\infty}^{\infty} \sum_{m=0}^M \sum_{s=-N}^N \sum_{n=\max(2, m, |s|)}^N \left(\frac{R_{\oplus}}{a} \right)^n I^m V_{ns}^m \Gamma_{ns}^m K_j^{-n-1,s} P_l^{vw} (G_{ms}^j + iH_{ms}^j) (C_{nm} - iS_{nm}) \exp[i(j\lambda - m\theta)] \right\} \quad (3.37)$$

where

$$\begin{aligned} \operatorname{Re}\{z\} &= \text{real part of } z \\ I &= \text{retrograde factor, defined by Eq.3.7} \\ V_{ns}^m &= \begin{cases} \frac{(-1)^{\frac{n-s}{2}}}{2^n} \frac{(n+s)!(n-s)!}{(n-m)!\left(\frac{n+s}{2}\right)!\left(\frac{n-s}{2}\right)!} & \text{if } n-s \text{ is even} \\ 0 & \text{if } n-s \text{ is odd} \end{cases} \end{aligned} \quad (3.38)$$

$$\Gamma_{ns}^m = \begin{cases} (-1)^{m-s} 2^s (1 + I\gamma)^{-Im} & \text{if } s \leq -m \\ (-1)^{m-s} 2^{-m} \frac{(n+m)!(n-m)!}{(n+s)!(n-s)!} (1 + I\gamma)^{Is} & \text{if } |s| \leq m \\ 2^{-s} (1 + I\gamma)^{Im} & \text{if } s \geq m \end{cases} \quad (3.39)$$

$K_j^{-n-1,s}$ = kernels of Hansen coefficients

P_l^{vw} = Jacobi polynomials

$$l = \begin{cases} n - m & \text{if } |s| \leq m \\ n - |s| & \text{if } |s| > m \end{cases} \quad (3.40)$$

$$v = |m - s| \quad (3.41)$$

$$w = |m + s| \quad (3.42)$$

$$G_{ms}^j + iH_{ms}^j = \begin{cases} [k + ih \operatorname{sgn}(s-j)]^{|s-j|} (\alpha + iI\beta)^{m-Is} & \text{if } |s| \leq m \\ [k + ih \operatorname{sgn}(s-j)]^{|s-j|} [\alpha - i\beta \operatorname{sgn}(s-m)]^{|s-Im|} & \text{if } |s| \geq m \end{cases} \quad (3.43)$$

$$i = \sqrt{-1}$$

$$\operatorname{sgn}(x) = \begin{cases} +1 & \text{if } x \geq 0 \\ -1 & \text{if } x < 0 \end{cases} \quad (3.44)$$

λ = mean longitude, the sixth equinoctial element

θ = Greenwich sidereal time

For the interested reader, Reference [19] contains alternative methods, including recurrence relations, to calculate V_{ns}^m , G_{ms}^j , and H_{ms}^j .

Two parts of the disturbing function merit further discussion here. The first pertains to the calculation of the kernels $K_j^{-n-1,s}$ of the Hansen coefficients $X_j^{-n-1,s}$. The kernels, functions of eccentricity or h and k , are defined by

$$K_j^{-n-1,s}(e) = e^{-|s-j|} X_j^{-n-1,s}(e) \quad (3.45)$$

They may be obtained in three ways that do not necessarily involve the direct computation of the Hansen coefficients. The first method is for kernels with $j = 0$ and with the first superscript

negative, i.e., $n > -1$:

$$K_0^{-n-1,s} = \begin{cases} 0 & \text{if } n = s \geq 0 \\ \frac{\chi^{1+2s}}{2^s} & \text{if } n = s + 1 \geq 1 \\ \frac{(n-1)\chi^2}{(n+s-1)(n-s-1)} [(2n-3)K_0^{-n,s} - (n-s)K_0^{-n+1,s}] & \text{if } n \geq s + 2 \geq 2 \end{cases} \quad (3.46)$$

where

$$\chi = \frac{1}{\sqrt{1-h^2-k^2}} \quad (3.47)$$

Appropriate initializations are

$$K_0^{0,0} = 1 \quad (3.48)$$

$$K_0^{0,1} = -1 \quad (3.49)$$

The second method of calculating the kernels is by infinite series representation. Note that more than one series have been investigated for use in generating the kernels via the Hansen coefficients [53]. The series of choice is

$$K_j^{-n-1,s} = (1-h^2-k^2)^{-n+\frac{1}{2}} \sum_{\kappa=0}^{\infty} Y_{\kappa+\eta,\kappa+\iota}^{-n-1,s} (h^2+k^2)^{\kappa} \quad (3.50)$$

where

$$Y_{\kappa+\eta,\kappa+\iota}^{-n-1,s} = \text{modified Newcomb operators} \quad (3.51)$$

$$\eta = \max(j-s, 0) \quad (3.51)$$

$$\iota = \max(s-j, 0) \quad (3.52)$$

The modified Newcomb operators recommended for use are calculated by

$$\begin{aligned} 4(\rho+\sigma) Y_{\rho,\sigma}^{\zeta,\xi} &= 2(2\xi-\zeta) Y_{\rho-1,\sigma}^{\zeta,\xi+1} + (\xi-\zeta) Y_{\rho-2,\sigma}^{\zeta,\xi+2} - 2(2\xi+\zeta) Y_{\rho,\sigma-1}^{\zeta,\xi-1} \\ &\quad - (\xi+\zeta) Y_{\rho,\sigma-2}^{\zeta,\xi-2} + 2(2\rho+2\sigma+2+3\zeta) Y_{\rho-1,\sigma-1}^{\zeta,\xi} \end{aligned} \quad (3.53)$$

which are initialized by

$$Y_{0,0}^{\zeta,\xi} = 1 \quad (3.54)$$

The third method is for use in calculating general kernels:

$$\begin{aligned} K_j^{-n-1,s} &= \frac{\chi^2}{(3-n)(1-n+s)(1-n-s)} \left\{ (3-n)(1-n)(3-2n)K_j^{-n,s} - \right. \\ &\quad \left. (2-n) \left[(3-n)(1-n) + \frac{2js}{\chi} \right] K_j^{-n+1,s} + j^2(1-n)K_j^{-n+3,s} \right\} \end{aligned} \quad (3.55)$$

This recurrence relation requires values of four kernels, $K_j^{-n,s}$, $K_j^{-n+1,s}$, $K_j^{-n+2,s}$ and, $K_j^{-n+3,s}$, for initialization. These starter kernels can be obtained by the second method described previously in this section. All kernels for this study were generated with the first two methods since the maximum degree examined is $N = 4$. The third method is useful for higher degree models.

The second portion of the disturbing function that is examined more closely here is the calculation of the Jacobi polynomials. Special Jacobi polynomials with $m = 0$ are calculated by

$$P_{n-s}^{ss}(\gamma) = 2^s \frac{n!}{(n+s)!} (1-\gamma^2)^{-\frac{s}{2}} P_{ns}(\gamma) \quad (3.56)$$

where $P_{ns}(\gamma)$ are associated Legendre functions. In general, the Jacobi polynomials are calculated by

$$\begin{aligned} 2l(l+v+w)(2l+v+w-2)P_l^{vw}(\gamma) = \\ (2l+v+w-1)[(2l+v+w)(2l+v+w-2)\gamma + v^2 - w^2]P_{l-1}^{vw}(\gamma) \\ - 2(l+v-1)(l+w-1)(2l+v+w)P_{l-2}^{vw}(\gamma) \end{aligned} \quad (3.57)$$

and are initialized by

$$P_0^{vw} = 1 \quad (3.58)$$

$$P_{-1}^{vw} = 0 \quad (3.59)$$

3.6 Third Body Disturbing Function

Perturbations caused by a third body, point-mass gravitational field are modeled by the following disturbing function [3, 19]:

$$\mathcal{R}(r, \varphi, t) = \frac{\mu_3}{R_3} \left(\frac{R_3}{|\mathbf{R}_3 - \mathbf{r}|} - \frac{r \cos \varphi}{R_3} \right) \quad (3.60)$$

where

μ_3 = gravitational constant of third body

$\mathbf{R}_3(t)$ = vector from central body to third body

R_3 = magnitude of \mathbf{R}_3

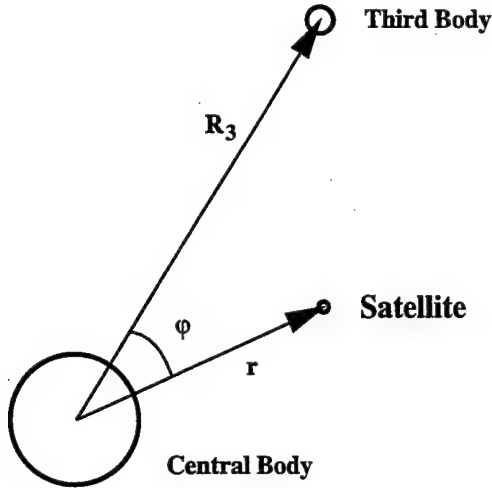


Figure 3.2: Geometry of Third Body Perturbations.

\mathbf{r} = vector from central body to satellite

r = magnitude of \mathbf{r}

φ = angle between \mathbf{r} and \mathbf{R}_3

Figure 3.2 illustrates the geometry of this situation.

The expansion of the third body disturbing functions closely follows that of the geopotential [16, 19]. One exception is the introduction of direction cosines (α, β, γ) which reflect the position of the third body with respect to the satellite. The third body disturbing function in equinoctial elements is

$$\mathcal{R} = \operatorname{Re} \left\{ \frac{\mu_3}{R_3} \sum_{j=-\infty}^{\infty} \sum_{s=0}^N \sum_{n=\max(2,s)}^N (2 - \delta_{0s}) \left(\frac{a}{R_3} \right)^n V_{ns} Y_j^{ns} Q_{ns} [C_s(\alpha, \beta) - iS_s(\alpha, \beta)] \exp(ij\lambda) \right\} \quad (3.61)$$

where

N = maximum power of parallax factor $\frac{r}{R_3}$

δ_{0s} = Kronecker delta

$$V_{ns} = \begin{cases} \frac{(-1)^{\frac{n-s}{2}}}{2^n} \frac{(n-s)!}{(\frac{n+s}{2})! (\frac{n-s}{2})!} & \text{if } n-s \text{ is even} \\ 0 & \text{if } n-s \text{ is odd} \end{cases} \quad (3.62)$$

$$Y_j^{ns} = [k + ih \operatorname{sgn}(s-j)]^{|s-j|} K_j^{ns} \quad (3.63)$$

$\text{sgn}(x) = \text{sign function, defined by Eq.3.44}$

$K_j^{ns} = \text{kernels of Hansen coefficients}$

$$Q_{ns}(\gamma) = \frac{d^s P_n(\gamma)}{d\gamma^s} \quad (3.64)$$

$C_s(\alpha, \beta), S_s(\alpha, \beta) = \text{functions of the direction cosines } \alpha \text{ and } \beta$

Danielson [19] gives recurrence relations for the V_{ns} and Q_{ns} functions for computational efficiency. The Y_j^{ns} functions deserve a few extra comments. Once again, kernels of Hansen coefficients must be calculated, and this is accomplished as described in the geopotential section with one exception. Kernels with $j = 0, s \neq 0$, and the first superscript nonnegative are calculated as follows:

$$K_0^{n,s} = \begin{cases} -\frac{2s-1}{s} K_0^{s-2,s-1} & \text{if } n = s - 1 \geq 1 \\ \frac{2s+1}{s+1} K_0^{s-1,s} & \text{if } n = s \geq 1 \\ \frac{2n+1}{n+1} K_0^{n-1,s} - \frac{(n+s)(n-s)}{n(n+1)\chi^2} K_0^{n-2,s} & \text{if } n \geq s + 1 \geq 2 \end{cases} \quad (3.65)$$

in which χ is defined again by Equation 3.47. Proper initializations are

$$K_0^{0,0} = 1 \quad (3.66)$$

$$K_0^{0,1} = -1 \quad (3.67)$$

The kernels with $j = 0$ and $s = 0$ are calculated along with general kernels, by using the infinite series representation:

$$K_j^{ns} = (1 - h^2 - k^2)^{n+\frac{3}{2}} \sum_{\kappa=0}^{\infty} Y_{\kappa+\eta, \kappa+\iota}^{n,s} (h^2 + k^2)^{\kappa} \quad (3.68)$$

where $Y_{\kappa+\eta, \kappa+\iota}^{n,s}$ are modified Newcomb operators which are calculated, as before, using Equation 3.53.

The $C_s(\alpha, \beta)$ and $S_s(\alpha, \beta)$ functions are defined by [19, page 32]

$$C_s(\alpha, \beta) + iS_s(\alpha, \beta) = (\alpha + i\beta)^s \quad (3.69)$$

and are calculated by the following recursion formulae

$$C_{s+1}(\alpha, \beta) = \alpha C_s(\alpha, \beta) - \beta S_s(\alpha, \beta) \quad (3.70)$$

$$S_{s+1}(\alpha, \beta) = \beta C_s(\alpha, \beta) + \alpha S_s(\alpha, \beta) \quad (3.71)$$

with initializations

$$C_0 = 1 \quad (3.72)$$

$$S_0 = 0 \quad (3.73)$$

3.7 Solar Radiation Pressure Disturbing Function

If the satellite is assumed to be always sunlit, the perturbation from solar radiation pressure (SRP) is a conservative force. Hence, it may be represented by a disturbing potential. For the class of satellites under consideration, this shadowless model seems reasonable, given the situation that GEO satellites enter Earth's shadow only around equinox and then for only a little over an hour during each pass. The disturbing function for SRP effects is given in References [6, 19]:

$$\mathcal{R} = -\frac{\mathcal{T}}{|\mathbf{R}_\odot - \mathbf{r}|} \quad (3.74)$$

for which

$$\mathcal{T} = \frac{C_R A \mathcal{L}}{mc} R_\odot^2 \quad (3.75)$$

C_R = radiation pressure coefficient of satellite

A = cross-sectional area of satellite

m = mass of satellite

\mathcal{L} = mean solar flux at 1 AU

c = speed of light

R_\odot = 1 AU

$\mathbf{R}_\odot - \mathbf{r}$ = vector from satellite to Sun

This disturbing function, when expanded in equinoctial elements, is identical to the third body disturbing function, with two exceptions:

- μ_3 is replaced by $-\mathcal{T}$ and
- n in the summation starts at 1 instead of 2.

Thus, the SRP disturbing function in equinoctial elements is

$$\mathcal{R} = \operatorname{Re} \left\{ -\frac{\tau}{R_{\odot}} \sum_{j=-\infty}^{\infty} \sum_{s=0}^{\mathcal{N}} \sum_{n=\max(1,s)}^{\mathcal{N}} (2 - \delta_{0s}) \left(\frac{a}{R_{\odot}}\right)^n v_{ns} Y_j^{ns} Q_{ns} [C_s(\alpha, \beta) - iS_s(\alpha, \beta)] \exp(ij\lambda) \right\} \quad (3.76)$$

All functions are defined as in the previous section.

Chapter 4

Perturbation Analysis and Results

The perturbation models detailed in Chapter 3 were implemented to study the perturbed motion of uncontrolled objects in geosynchronous (GEO) and supersynchronous (SSO) regions. This chapter describes the methodology employed in the analytical part of the study, validation of the models by numerical integration, and analysis of each perturbation source to determine its effects. Application to the reorbiting problem follows in Chapter 5.

4.1 General Methodology

The methodology is described in two parts. The first concerns the process of transforming the expressions, Lagrange's Planetary Equations, into a form suitable for analysis. This involves obtaining the disturbing potential for each perturbation source in workable form, taking the partial derivatives of the potential with respect to the orbital elements, and substituting these expressions into the Planetary Equations. Some assumptions are introduced to reduce the expressions to manageable sizes. In the second part, the variation equations are examined term by term to determine individual effects which are then summed to calculate the cumulative variations.

4.1.1 Formulation of Lagrange's Planetary Equations

Evaluation of Lagrange's Planetary Equations 3.26–3.31 can be a cumbersome job if conducted manually. In this study, a well-tested and widely available symbolic manipulator, Mathe-

matica, is utilized to handle the expressions and perform somewhat tedious tasks, such as expanding summations and taking partial derivatives of long and complicated expressions. The great advantage of this route is that common errors, such as dropped terms and wrong signs, are confidently avoided. The drawback is that one does not always know all of the ramifications associated with built-in functions and commands; a seemingly straightforward function may produce quite unexpected results in some cases but not others. Blind application will likely produce surprising and erroneous results; therefore, intermediate expressions should be examined carefully.

For each perturbing force, with solar third body and lunar third body treated separately, the associated disturbing potential is modeled in Mathematica. Of particular concern at this juncture is the truncations of the infinite series represented by summations. In general, these limits are set as appropriate for the orbit class under consideration: orbits with GEO-type altitudes and low eccentricities. Further discussion of the truncation decisions for each perturbing force follows in later sections. The orbits of GEO and SSO objects generally have inclinations lower than 15° which dictates that direct equinoctial elements are proper; thus, the retrograde factor I is equal to 1. The disturbing potentials are composed of many custom functions as well as well-known ones, such as Legendre and Jacobi polynomials, which are available from the Mathematica internal library. The custom functions, defined and verified for this study, are fairly straightforward, requiring only familiarity with Mathematica and general programming techniques. After the summations are expanded, the real part of these complex expressions form the disturbing potential. Mathematica performed well, except for one small matter. The factor $\sqrt{1 - h^2 - k^2}$ appears often in the disturbing functions. Not knowing that $h^2 + k^2 < 1$ for elliptical orbits so that the factor is always real, Mathematica treats it as possibly complex, thus generating some extra terms. These terms are easily identified, and discarding them properly from the disturbing potential expressions is a simple matter.

Once the disturbing potentials are available, the Planetary Equations can be formed. This involves taking partial derivatives of the disturbing functions with respect to orbital elements and direction cosines, which Mathematica handles smoothly. Since the study is primarily concerned with orbits in terms of their radial distance, only the Planetary Equations addressing changes in

semimajor axis, Equation 3.26, and eccentricity, i.e., equinoctial elements h and k , Equations 3.27 and 3.28, are of interest. Some of these equations for \dot{a} , \dot{h} , and \dot{k} are quite large, about 40,000–73,000 lines in length with a typical visual editor. Therefore, assumptions are made to reduce the equations to a workable size. The first is a zero inclination assumption which translates to $p = q = 0$ in equinoctial elements. This decision is based on the fact that GEO satellites and those in storage orbits are at relatively low inclinations, with about 15° being the upper limit. Discussion of the effects of this assumption is contained in later sections. Mathematica was employed to implement this assumption. Next, the \dot{a} , \dot{h} , and \dot{k} equations are reduced to first order in eccentricity. This works out to be roughly equivalent to first order in h and k , also, since $h \leq e$, $k \leq e$, and $hk \leq e^2$. First order eccentricity analysis seems appropriate since e remains relatively small for uncontrolled objects in GEO regime. For example, a GEO satellite with initial eccentricity of zero and subjected to perturbations (4x4 geopotential field, solar and lunar gravitation, and solar radiation pressure) will see its eccentricity increase to about 0.0008 over 100 years, according to one study [27]. Among the reorbited objects, again eccentricity remains small [12]. The orbits of collision pieces is another matter. However, if the fragments' orbits have eccentricities larger than, say, 0.0035, for a typical reorbiting altitude, the fragments are likely to be immediately crossing the GEO region. Thus, perturbation analysis is unnecessary in cases of large eccentricity. Removing the higher order terms from the \dot{a} , \dot{h} , and \dot{k} equations was performed manually with the resulting equations fed back into Mathematica to be expanded.

4.1.2 Analysis of Lagrange's Planetary Equations

The models were then transferred to Microsoft Excel worksheets for term by term analysis. At this point, for each perturbation source, there are three expressions, one each for \dot{a} , \dot{h} , and \dot{k} . In order to estimate the amplitudes of the variations in a , h , and k , for individual terms in each expression, analytical integration of a sort is performed. This is generally described as follows. A typical term in the variation equations is of the form

$$\dot{a} = a \cos \theta \quad (4.1)$$

in which \dot{a} represents one term in either the equations for the variations in semimajor axis or in eccentricity. Variables with no secular changes are integrated as constants. Semimajor axis, eccentricity, and inclination experience no secular changes in the GEO regime [12]; thus, the elements a , h , and k are treated as constants. In the example given by Equation 4.1, a is a quantity subject only to periodic variations. Fast variables, θ in the example, are identified and approximated by the product of the variables' secular rates and time:

$$\dot{a} = a \cos \dot{\theta}_{sec} t \quad (4.2)$$

The variables describing the positions of the satellite and the perturbing sources within their orbits are the fast variables. Next, integrate over time. Equation 4.2 becomes

$$\begin{aligned} \Delta a &= \frac{a}{\dot{\theta}_{sec}} \sin \dot{\theta}_{sec} t \\ &= \frac{a}{\dot{\theta}_{sec}} \sin \theta \end{aligned} \quad (4.3)$$

Initial conditions, θ_0 in this example, are ignored because they do not affect the amplitude of Δa and because this particular aspect of the phasing of effects is disregarded.

Two points concerning this analytical integration merits further discussion. The first pertains to the amplitude of the variations. In Equation 4.3, the amplitude of Δa is clearly $a/\dot{\theta}_{sec}$. However, although the integration process assumes a constant "mean" value for semimajor axis and eccentricity, the values actually employed are osculating values. Figure 4.1 illustrates this difference. Point A represents the worst case, in which the osculating value is Δa larger than the mean value. From this point, it is seen that the actual variation is twice the amplitude, or $2\Delta a$. Although at other points, the variation will be overestimated, a worst case bound on the variations is sought here. Therefore, amplitudes are doubled to represent the largest possible variation. A second concern with this analytical integration method is that it ignores variations caused by changes in a , h , and k . For semimajor axis, the variations in a are very small in proportion to the value of a at GEO altitudes. The result is that only minor errors are introduced by ignoring the variations in a . This argument does not work for eccentricity or h and k . In this case, both eccentricity and the variations in eccentricity due to perturbations are small and roughly of the same order of magnitude. Fortunately, the most significant terms in the \dot{a} , \dot{h} , and \dot{k} equations, i.e., the

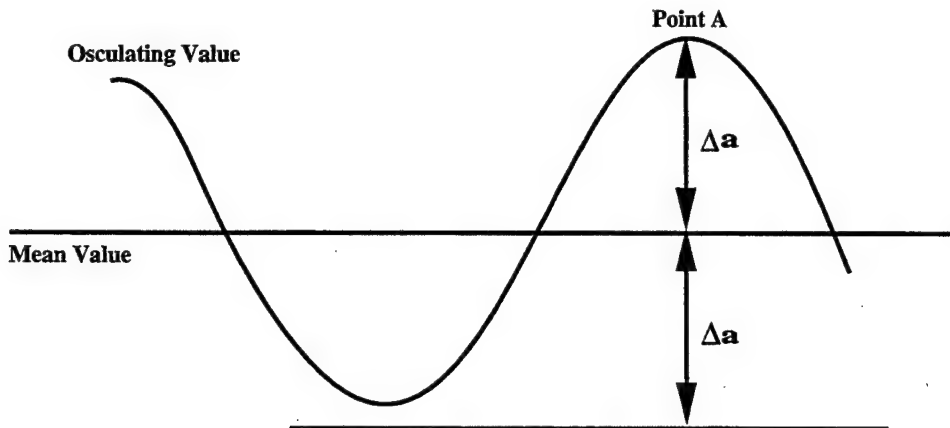


Figure 4.1: Variations from Osculating Values.

terms causing the biggest variations, are independent of h and k . Thus, these terms are not subject to errors caused by assuming a fixed eccentricity. The eccentricity-dependent terms are relatively small and do not seem to adversely affect the calculated maximum variations in semimajor axis and eccentricity.

Details pertaining to each perturbation source are further discussed in following sections. Calculation of the amplitudes of perturbation effects is accomplished using Microsoft Excel, a spreadsheet software. Amplitudes are summed by unique frequencies and by all frequencies. The first allows for the identification of individual effects and the latter, for an upperbound on cumulative effects, since the phasing of the individual frequencies are disregarded. As explained previously, the amplitudes are doubled to approximate actual variations. The equinoctial elements, h and k , are related back to Keplerian eccentricity for physical insight. Examination of associated h and k equations shows terms with similar amplitudes and frequencies. Furthermore, variations in eccentricity are contained separately and fully in either the \dot{h} or \dot{k} equations; evaluation of both equations is been redundant, except for its use in double-checking details. Thus, for each perturbation model, maximum variations in semimajor axis and eccentricity are generated given initial orbital elements and the object's physical characteristics.

The results are validated by comparison with numerical integration. The Draper R & D version of the Goddard Trajectory Determination System (GTDS) contains strictly numerical

integrators as well as the Draper Semianalytic Satellite Theory (DSST) [24, 25, 48]. The Cowell numerical integrator is simple to set up, and it easily handles shorter propagations. Thus, element history plots from Cowell integrations provide the needed information on short-periodic variations. Long-periodic variations are better represented by the DSST average orbit generator (DSST AOG), in which short-periodic terms have been averaged out. The DSST integrations in this study are limited to 20 years because of the limited availability of accurate third body ephemerides. This is deemed sufficient for validation of the analytical models, at least for an initial study. For each perturbation source, the significant short- and long-periodic variation terms in semimajor axis and eccentricity are singled out and compared by both amplitude and frequency using the same test case. Specifics for the propagation runs are given in Table 4.1 in which settings are the same for both Cowell and DSST AOG unless otherwise noted. Section 4.2.2 elaborates on the choice of semimajor axis and eccentricity for the test orbit. Inclination-dependent effects are captured by starting the integrations at 15° for inclination; for other variations, inclination is initially set at zero. Initial values for node, argument of perigee, and mean anomaly are arbitrarily chosen to be zero. Note that the 400-second step size for the Cowell integrator is small enough to allow for over 200 steps/revolution. Finally, cumulative perturbation effects from the analytical and numerical models are compared in three cases with varying semimajor axes.

4.2 Geopotential

Particulars of the methodology concerning only the geopotential are presented first in this section. This includes discussion of the truncation decisions on the infinite series in the disturbing potential, the effects of the assumptions employed in reducing the variation equations, and the term by term analysis by integration. Validation of the geopotential model by numerical integration follows, and this section ends by summarizing the effects on semimajor axis, eccentricity, and minimum radial distance from Earth's nonspherical gravitational forces.

Table 4.1: Setting Descriptions for Propagators in Test Case.

Integrator	12th order summed Cowell/Adams predict-partial correct
Step Size	400 s for Cowell 43200 s for DSST AOG
Geopotential Model	4x4 JGM-2
Third Body Model	Solar/Lunar based on JPL DE 118/200 ephemerides
SRP Model	spherical, conical shadow, single C_R
Semimajor Axis	42194 km
Eccentricity	0.007
Inclination	0, 15 degrees
Ascending Node	0
Arg of Perigee	0
Mean Anomaly	0
Initial Time	midnight on 18Oct98 for Cowell midnight on 18Oct88 for DSST AOG
Final Time	Varies with period of perturbation
C_R	1.2
A/M	1 m ² / 100 kg
Coordinate System	B1950.0

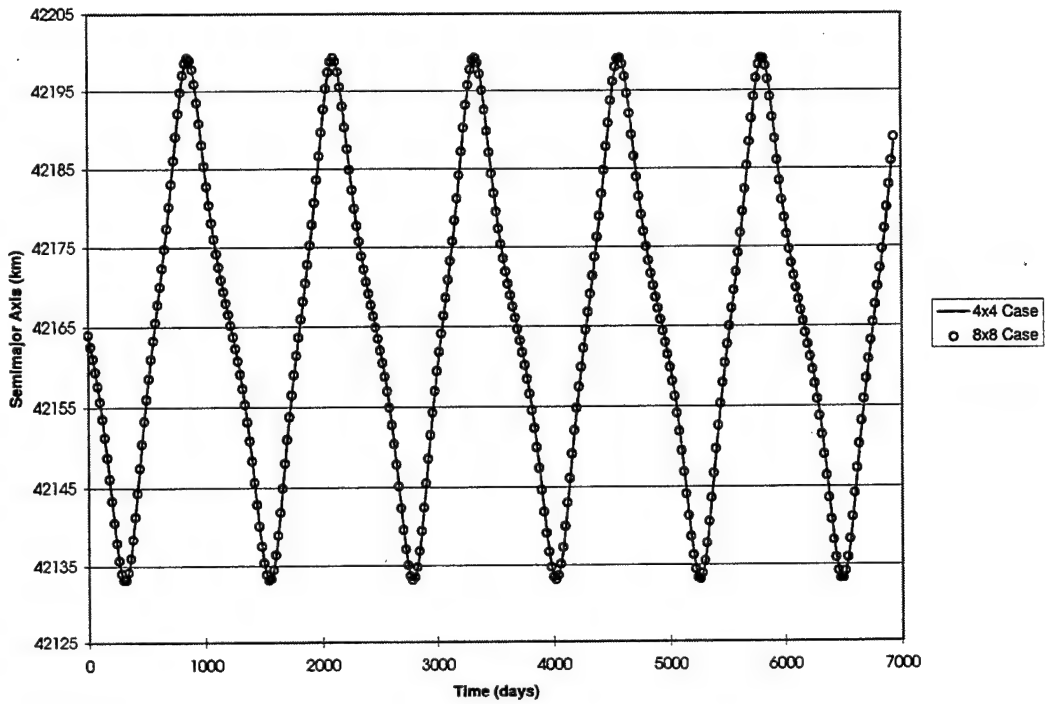


Figure 4.2: Semimajor Axis History for 4x4 and 8x8 Geopotential at GEO.

4.2.1 Geopotential Analysis

A 4x4 Joint Gravity Model-2 is employed, and for the GEO regime, this is deemed sufficient [28]. Figures 4.2 and 4.3 are history plots of semimajor axis and eccentricity, respectively, for both 4x4 and 8x8 gravity fields, as integrated by DSST AOG over 19 years. Clearly, the variations in semimajor axis and eccentricity are very similar for both cases, though the 4x4 model departs a little from the better model at the latter part of the integration, as seen in Figure 4.3. This disparity is due to higher order terms and roughly translates to altitude differences on the order of hundreds of meters. Since perturbations cause overall variations on the order of tens of kilometers, the error introduced by this truncation of the gravity model is acceptable. Further comparison of the two cases indicates that the difference in mean anomaly does drift off. However the position of the objects at any specific time, as given by mean anomaly, is unimportant for the purposes of this study. Thus, the 4x4 gravity field is judged to be appropriate.

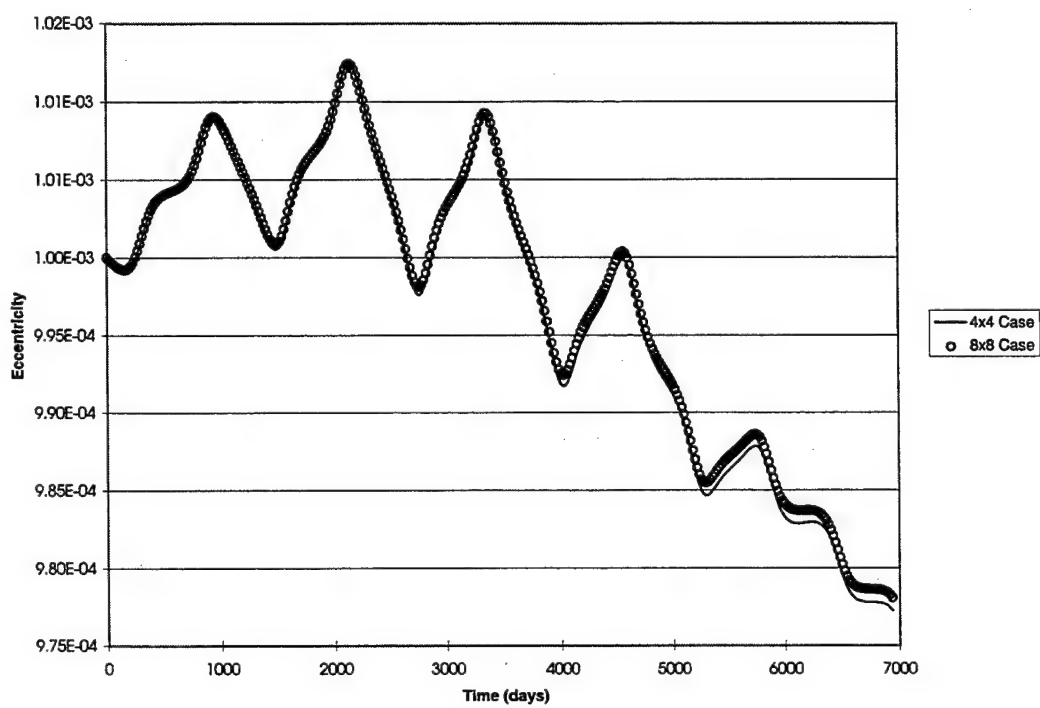


Figure 4.3: Eccentricity History for 4x4 and 8x8 Geopotential at GEO.

Truncation of the j series in the disturbing potential function, Equation 3.37, is not easily related to physical attributes of the orbits on first examination. It is clearly related to eccentricity, but the summation bounds do not allow one to pick out all first order eccentricity terms. It is also related to frequency by generating multiples of λ . Without a better guess, $|j|_{max}$ is initially set to 2, with the hope that all significant terms would be captured. However, from numerical integration plots, the existence of a sizable resonance term for $j = -3, 3$ is concluded. Accordingly, the bound of the j series is extended to $|j|_{max} = 3$. This, together with $N = M = 4$, forms the limits of the basic geopotential model studied.

The Planetary Equations were formed and reduced as described in Section 4.1.1. Incorporated into the variation equations are the direction cosines associated with geopotential perturbations which are

$$\begin{aligned}\alpha &= -\frac{2p}{1+p^2+q^2} \\ \beta &= \frac{2q}{1+p^2+q^2} \\ \gamma &= \frac{1-p^2-q^2}{1+p^2+q^2}\end{aligned}\tag{4.4}$$

Reducing the expressions to first order in eccentricity did not eliminate any important terms. However, implementation of the zero inclination assumption did. Comparison with numerical integration shows two missing inclination-dependent terms that are significant for low, but not zero, inclinations. They are the J_2 short-periodic term in a and the J_3 long-periodic effect in e which were removed by setting $p = q = 0$. Since GEO and SSO objects do range up to 15° in inclination, inclusion of these terms is deemed important. Identifying a missing term is in itself a complicated process. First, information about the term's period and dependence on certain orbital parameters such as eccentricity and inclination and associated gravitational coefficient is gathered. Next, the n , m , s , and j indices in the analytic perturbation model are examined, one by one, to find the ones that will generate the observed characteristics of the missing term. Once identified, it is simple enough to retrieve them with Mathematica and add them to the basic geopotential model.

After the \dot{a} , \dot{h} , and \dot{k} expressions are transferred from Mathematica to Excel spreadsheets, analytical integration, as described in Section 4.1.2, of each term in the equations is carried out. The variations in semimajor axis and eccentricity are then given by expressions for each term which can be evaluated for a given orbit.

The values employed for a , h , and k are partially prescribed by the semimajor axis and eccentricity of the orbit to be studied. However, h and k also depend on the orbit's argument of perigee ω and right ascension of ascending node Ω . Both are left as variables to adjust as necessary to find the largest cumulative variation amplitudes. However, the values for ω and Ω have little effect on the overall perturbing effect because terms containing h or k are small.

The fast variables are the satellite's mean longitude and Greenwich sidereal time which are approximated by the product of a constant value for $\dot{\lambda}_{sec}$ and $\dot{\theta}$, respectively, and time. The secular rates of each are calculated as follows.

The secular variation of λ is approximated by

$$\dot{\lambda} = n + \dot{\omega}_{J_2,sec} + \dot{\Omega}_{J_2,sec} + \dot{\lambda}_{\odot,sec} + \dot{\lambda}_{\oplus,sec} + \dot{\lambda}_{SRP,sec} \quad (4.5)$$

in which

n = mean motion of the satellite

$\dot{\omega}_{J_2,sec}$ = secular variation of ω due solely to J_2

$\dot{\Omega}_{J_2,sec}$ = secular variation of Ω due solely to J_2

$\dot{\lambda}_{\odot,sec}$ = secular variation of λ due solely to solar third body

$\dot{\lambda}_{\oplus,sec}$ = secular variation of λ due solely to lunar third body

$\dot{\lambda}_{SRP,sec}$ = secular variation of λ due solely to SRP

The secular rates of ω and Ω are based on only the effects of J_2 because it is by far the dominant term in the geopotential, larger by several orders of magnitude than the next largest term. The terms $\dot{\lambda}_{\odot,sec}$, $\dot{\lambda}_{\oplus,sec}$, and $\dot{\lambda}_{SRP,sec}$ do not include the mean motion.

Finally, $\dot{\theta}$ is given by

$$\dot{\theta} = \frac{361^\circ \times (\pi/180^\circ)}{86400} \text{ rad/s} \quad (4.6)$$

The dominant term in Equation 4.5 is of course the mean motion, n . However, $n \approx \dot{\theta}$ for objects in GEO and SSO. Therefore, when $j = m$, the smaller terms in $\dot{\lambda}_{sec}$ become important in determining the amplitudes of these long-periodic, resonant effects.

4.2.2 Geopotential Model Validation

The geopotential model is validated through comparison with numerical and semianalytical integration results. Semimajor axis and eccentricity are examined separately, and for each, the significant effects can be classified as either short-periodic (SP) or long-periodic (LP) terms.

One case is employed to validate each of the analytical perturbation models individually. For this study, the semimajor axis, eccentricity, and inclination of the test orbit should reflect those of objects in GEO or SSO regions or of fragments generated by collisions in SSO. In fact, semimajor axis can be chosen to coincide with GEO, but near GEO altitudes, the analytical geopotential model notably exaggerates the variations due to the resonant terms. This is because the analytical integration holds a and therefore, $\dot{\lambda}_{sec}$, constant, forcing a deeper resonance in the equations than is actually experienced by uncontrolled objects in osculating orbits. At around 30 km away from GEO, the geopotential model recovers accuracy. Proposed reorbiting distances are no less than 100 km above GEO; thus, this limitation should not affect the primary objective of this research, studying the effects of collisions in SSO. The problem of defining the GEO region will be handled in Chapter 5.

At GEO+30 km, the resonances are shallow enough for the analytical geopotential model to recover accuracy. Validation is performed for $a = 42194$ km and $e = 0.007$, as listed in Table 4.1, which provides details of the numerical and semianalytical integration settings. The eccentricity is larger than those of most GEO and SSO objects; this value was selected in anticipation that the orbits of collision fragments which will have slightly larger eccentricities.

Table 4.2 summarizes the significant periodic effects for this test orbit as given by the numerical and analytical models. The amplitudes listed have not been doubled and so reflect half variations, as explained in Section 4.1.2. Most terms in the analytical expressions have slightly larger amplitudes than observed amplitudes from plots generated by numerical and semianalytical

Table 4.2: Significant Periodic Effects from Geopotential Perturbations.

	Numerical Amplitude	Analytical Amplitude	Period
Semimajor Axis			
SP	115 m	126 m	12 hr and 24 hr
LP	10 km	11.9 km	0.8 yr, 1.2 yr, and 2.3 yr
Eccentricity			
SP	3.6 e-05	3.7 e-05	24 hr
LP	4.6 e-05	3.8 e-05	28 yr

integration. This is anticipated from employing a mostly frequency-independent method. For this study, however, establishing a bound on the variations in semimajor axis and eccentricity is the primary objective in modeling perturbation effects. While comparison of individual effects is significant to ascertain the reliability of the model, irregularities in individual terms do not matter as much as the performance of the entire model. It is also important to note that though the numerical models are essentially used as truth models, the numerical amplitudes in Table 4.2 are only estimated values, which contain uncertainties from the process of interpretation from plots. Discussion of individual effects follow.

Figure 4.4 is the semimajor axis history plot showing the SP variations. The test case is propagated over two days with the Cowell integrator and initial inclination of 15° . There two periodic effects, one with a 12-hour period and the other, a 24-hour period, captured in the plot. From the analytical model, the 12-hour variation, which is inclination-dependent, is calculated to be almost five times larger than the 24-hour effect. The combined amplitude of these variations is estimated from the plot to be 115 km, as listed in Table 4.2, but the individual amplitudes are more difficult to assess. Long-periodic effects in semimajor axis, resulting from the resonance terms, are seen over 4 years in Figure 4.5. The analytical geopotential model indicates that there are three resonance terms contributing the largest variations in semimajor axis. In the plot, only two can be readily identified: the effects with 2.3- and 1.2-year periods. The third, which has a shorter period of 0.8 years, seems to be masked. According to the analytical model, the 1.2-year effect is by far

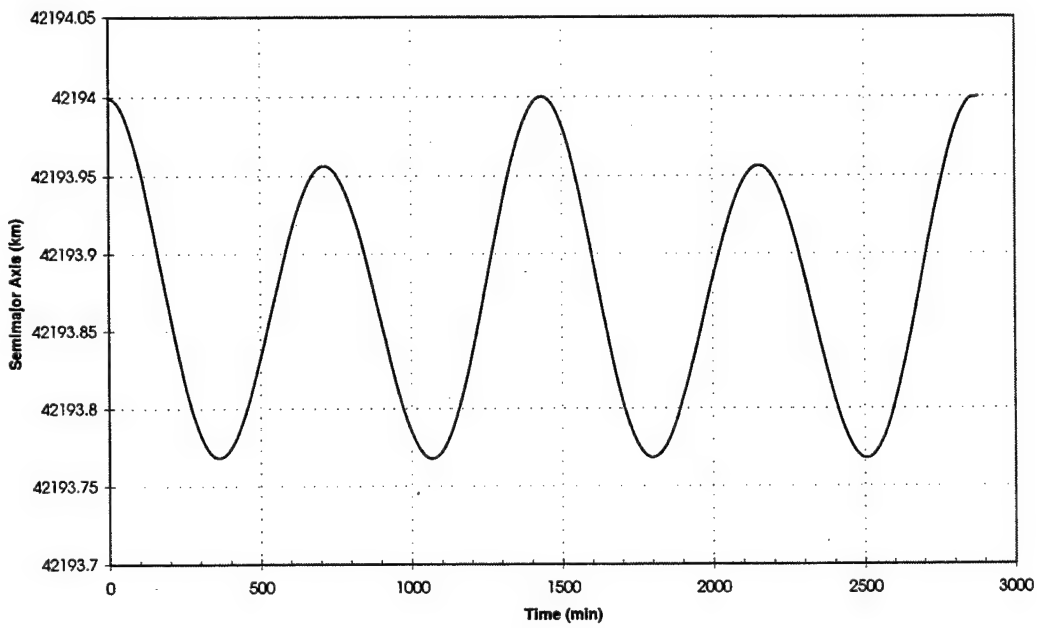


Figure 4.4: Geopotential Short-Periodic Variations in Semimajor Axis.

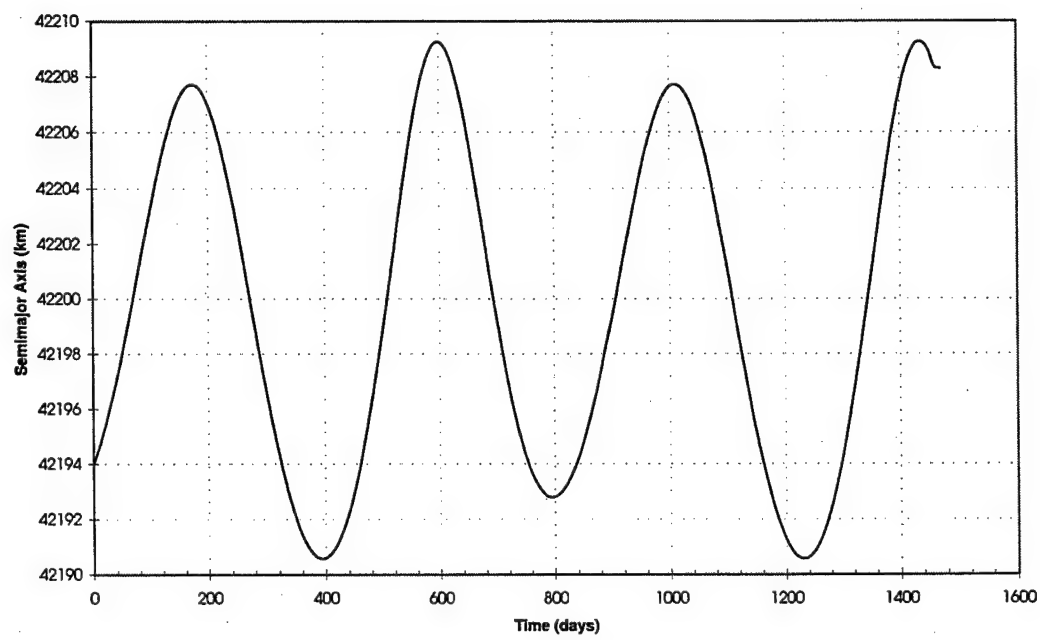


Figure 4.5: Geopotential Long-Periodic Variations in Semimajor Axis.

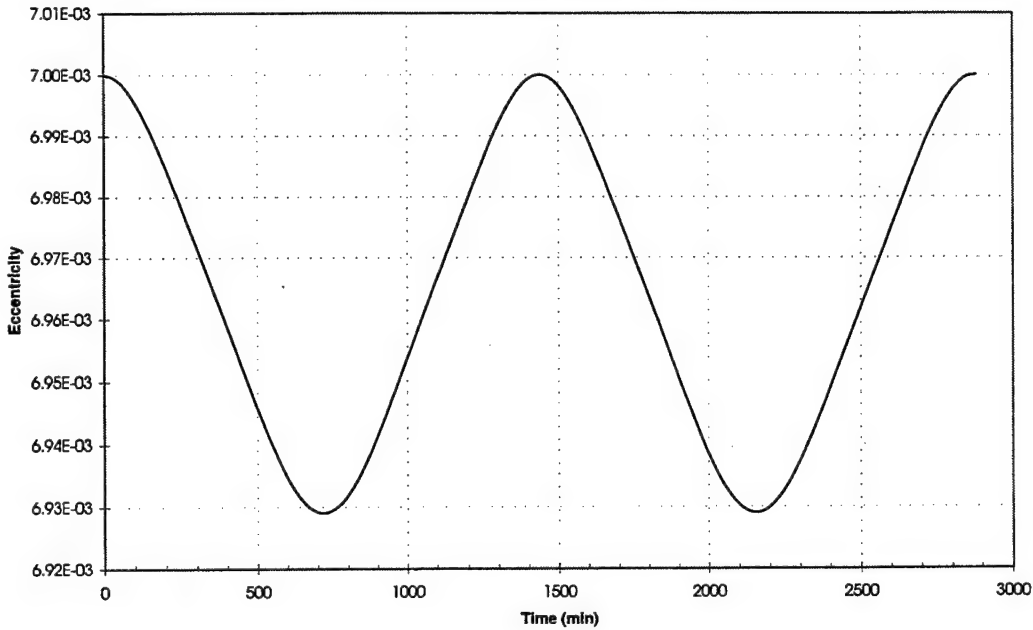


Figure 4.6: Geopotential Short-Periodic Variations in Eccentricity.

the dominant term with amplitude about 10 times greater than those of the other two resonance terms.

J_2 is the force behind the SP variations in eccentricity, shown in Figure 4.6. The plot clearly shows one periodic term which matches the analytical term in amplitude as well as period. The one item in Table 4.2 that may be of concern is the LP variations in eccentricity since the analytical model appears to underestimating. The term in question is a J_3 effect and is known to be dependent on inclination, as illustrated by the following plots. The one in Figure 4.7 corresponds to a zero inclination case, in which the J_3 term does not appear. Multiple effects appear, but none are significant since the variations are on the order of 10^{-7} . At $i = 15^\circ$, however, which is the case shown in Figure 4.8, J_3 has a substantial effect. The variation shown in this plot appears to have a period of about 38 years, though only roughly half of the period is captured by DSST over 20 years. The J_3 term in the analytical model has a period of 28 years which corresponds to the

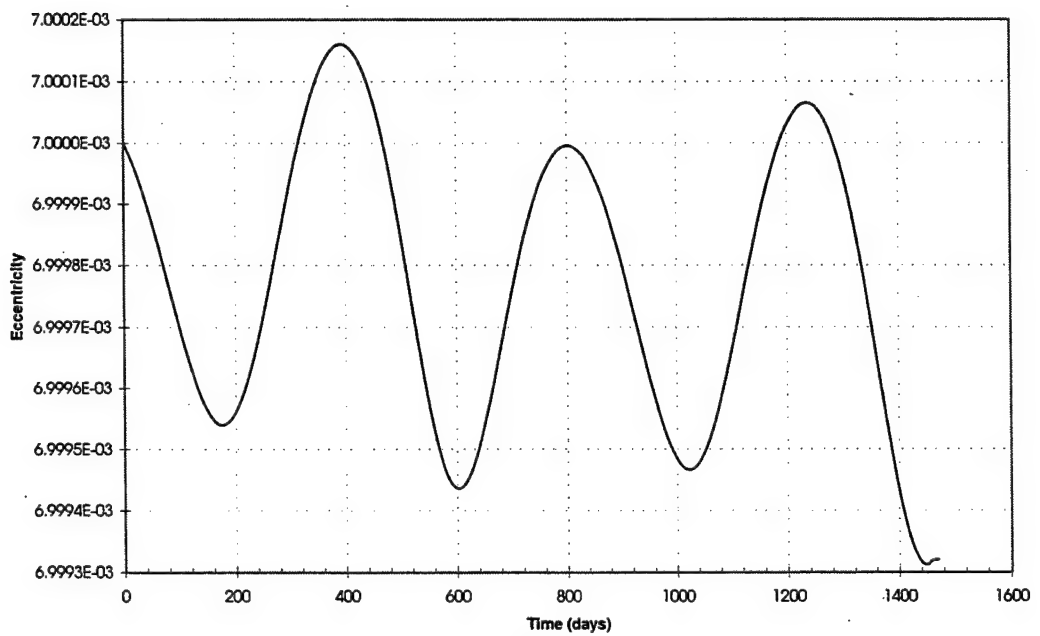


Figure 4.7: Geopotential Long-Periodic Variations in Eccentricity at Zero Inclination.

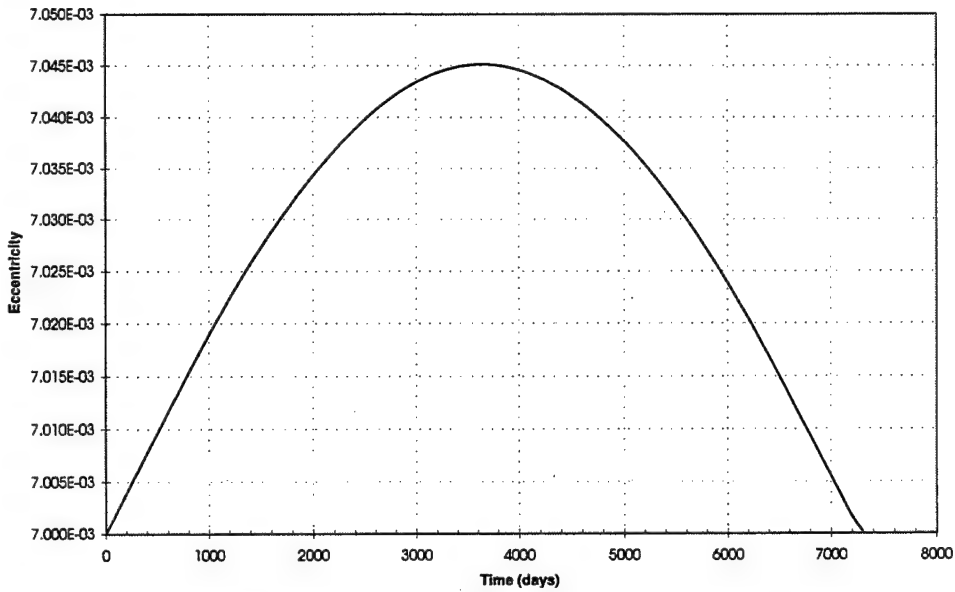


Figure 4.8: Geopotential Long-Periodic Variations in Eccentricity at 15° Inclination.

argument of perigee rate of the satellite. This difference in periods may be due to the fact that the propagator included only geopotential perturbations. The addition of third body and/or SRP effects may influence this effect. For example, inclination history plots for integration with only gravity harmonics in addition to two-body dynamics show that inclination will exceed 16° if the initial inclination is set near 15°. This does not reflect the situation in reality because third body perturbations were not modeled. Another explanation for the discrepancies in amplitude as well as period is that the analytical term is a different term which has not been identified and isolated in numerical plots. This implies that the effect shown in Figure 4.8 is missing in the analytical model. Future work should include further investigation into the LP variations in eccentricity.

4.2.3 Summary of Geopotential Perturbation Effects

Figure 4.9 summarizes the variations due to geopotential perturbations in the radial direction. Data for this plot is generated by the analytical model, except near GEO altitude due to the limitations of the analytical model in that vicinity. The near-GEO data is supplied by DSST.

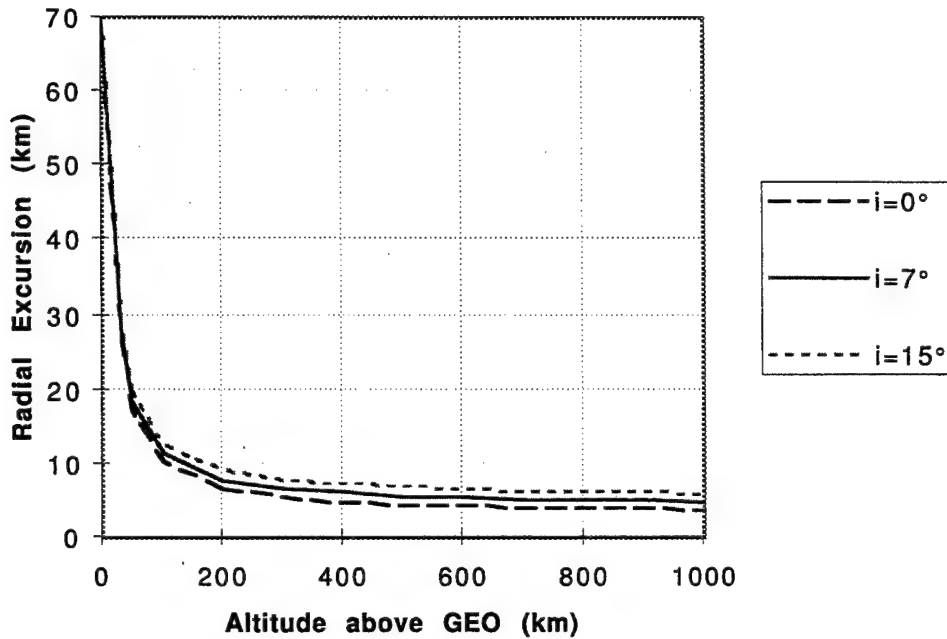


Figure 4.9: Geopotential Induced Variations in Radial Direction.

Recall that total variations in semimajor axis and eccentricity are calculated by summing the individual terms of different frequencies and that amplitudes, such as those in Table 4.2, are doubled to account for the use of osculating instead of mean elements. Let Δa_{geo} and Δe_{geo} represent the total variations. Then, maximum radial excursion is defined and calculated by

$$\begin{aligned}
 \Delta r &= r_1 - r_2 \\
 &= a(1 - e) - (a - \Delta a_{geo})(1 - (e + \Delta e_{geo})) \\
 &= \Delta a_{geo}(1 - e) + a\Delta e_{geo} - \Delta a_{geo}\Delta e_{geo}
 \end{aligned} \tag{4.7}$$

The altitude above GEO is given by $a - 42,164$ km for varying semimajor axes while eccentricity is fixed at 0.007, the value used in the validation process. In Figure 4.9, geopotential perturbations are shown for three different inclinations. At GEO, the 70 km in radial excursion is mostly due to the resonant effects, which decrease sharply as altitude increases above GEO. At GEO+200 km, effects are below 10 km for all three cases. The differences in radial excursion due to inclination are overwhelmed by the resonance terms until around GEO+60 km. They then steadily increase

Table 4.3: Analytical Expressions for Significant Geopotential Terms.

	Term	Period
Semimajor Axis		
SP	$-12\mu^{1/2}R_{\oplus}^2C_{20}a^{-5/2}(1+C)^{-2}[2pq\cos 2\lambda + (p^2 - q^2)\sin 2\lambda]$	12 hr
	$3\mu^{1/2}R_{\oplus}^2C_{20}a^{-5/2}(k\sin \lambda - h\cos \lambda)$	24 hr
LP	$90\mu^{1/2}R_{\oplus}^3a^{-7/2}\{S_{33}\cos[3(\lambda - \theta)] - C_{33}\sin[3(\lambda - \theta)]\}$	0.8 yr
	$12\mu^{1/2}R_{\oplus}^2a^{-5/2}\{S_{22}\cos[2(\lambda - \theta)] - C_{22}\sin[2(\lambda - \theta)]\}$	1.2 yr
	$-30\mu^{1/2}R_{\oplus}^4a^{-9/2}\{S_{42}\cos[2(\lambda - \theta)] - C_{42}\sin[2(\lambda - \theta)]\}$	1.2 yr
	$-3\mu^{1/2}R_{\oplus}^3a^{-7/2}\{S_{31}\cos(\lambda - \theta) - C_{31}\sin(\lambda - \theta)\}$	2.3 yr
Eccentricity		
SP	$-3\mu^{1/2}R_{\oplus}^2C_{20}a^{-7/2}\cos \lambda$	24 hr
LP	$1.5\mu R_{\oplus}^3C_{30}a^{-6}\sin i \sin(2.5\sin^2 i - 1)\sin \omega$	28 yr

until approximately GEO+200 km, at which point the difference between the 0° and 15° cases is about 2.5 km, and the differences appear to cease growing.

Table 4.3 lists the analytical expressions for the largest terms in the geopotential model. The periods are approximate, and they correspond to the validation case orbit with $a = 42,194$ km and $e = 0.007$. All terms are in equinoctial elements, except the LP eccentricity term. This is presented in Keplerian elements because searches for it in equinoctial form were unsuccessful. Explanations for the variables in the analytical expressions are given in Section 3.5 and Equations 3.1–3.6 and 3.34. The variations are mostly independent of eccentricity with the exception of the small J_2 SP semimajor axis term. In general, larger terms have no dependence on eccentricity. The dependence on inclination of the J_2 SP and J_3 LP effects appears in Figure 4.9 and produces about 3 km difference in the radial direction. Resonance terms, the long periodics in semimajor axis, are by far the most significant factor, and they are not functions of eccentricity nor inclination.

4.3 Solar Third Body

Implementation of the solar third body perturbation model follows a similar route to the geopotential model. The potential function and variation equations are much smaller and therefore, easier to manage. A major difference between the third body potential equations and the geopotential analysis is the introduction of new direction cosines which reflect the position of the third body with respect to the satellite. Subtleties in those direction cosines proved to be nontrivial.

4.3.1 Solar Third Body Analysis

The third body disturbing function, Equation 3.61, includes two infinite series which require truncation decisions. For solar perturbations, an appropriate truncation of the parallax factor $\left(\frac{r}{R_3}\right)^N$ is $N = 3$. This conclusion is based on the truncation algorithm programmed into DSST which is summarized in References [19] and [20]. The j series is truncated by $|j|_{max} = 2$ based on preliminary examination of significant frequencies from numerical integration element history plots and also on the order of eccentricity. From the results, it appears that no major terms were left out by the above truncations.

The third body is assumed to be in a circular orbit. Therefore, R_3 is constant and equal to the mean distance between Earth and the Sun [59]:

$$R_3 = 1.0000010178 \text{ AU} \times 149597870 \text{ km/AU} \quad (4.8)$$

This is a reasonable assumption since the actual eccentricity of Earth's orbit about the Sun is small, about 0.0167 [64], and no considerable perturbing effect is left unmodeled as a result. The methodology then traces the same pattern as before. The resulting variation equations are first order in eccentricity with zero satellite inclination assumed.

The direction cosines employed for third body analysis are

$$\begin{aligned} \alpha &= \cos \Omega_3 \cos \theta_3 - \sin \Omega_3 \cos i_3 \sin \theta_3 \\ \beta &= \sin \Omega_3 \cos \theta_3 + \cos \Omega_3 \cos i_3 \sin \theta_3 \\ \gamma &= \sin i_3 \sin \theta_3 \end{aligned} \quad (4.9)$$

where

Ω_3 = right ascension of ascending node of the third body

θ_3 = argument of latitude of the third body

= argument of perigee + true anomaly

i_3 = inclination of the third body

These expressions already reflect the assumption of zero inclination for the satellite; this explains why the satellite's inclination and ascending node do not appear in Equations 4.9. For the Sun [59],

$$\Omega_3 = 0, \text{ by definition} \quad (4.10)$$

$$i_3 = 23^\circ 26' 21.448'' \quad (4.11)$$

and θ_3 is left as the fast variable along with satellite mean longitude, λ . During the model validation process, it became apparent that a significant effect was missing, and the reason for its absence can be attributed to the above direction cosines, Equations 4.9. The period of the missing term is roughly 28 years, about half of the period of the satellite's node rate. As perturbation effects increase the inclination of the satellite, the node is no longer undefined. The satellite node is a secularly but slowly varying quantity. Thus, it is generally masked in the equations by the faster variables, except in a few terms. The missing effect is recovered by isolating the suspected term, in this case $n = s = 2$ and $j = 0$, and substituting direction cosines with the node of the satellite restored:

$$\begin{aligned} \alpha &= \cos(\Omega_3 - \Omega) \cos \theta_3 - \sin(\Omega_3 - \Omega) \cos i_3 \sin \theta_3 \\ \beta &= \sin(\Omega_3 - \Omega) \cos \theta_3 + \cos(\Omega_3 - \Omega) \cos i_3 \sin \theta_3 \\ \gamma &= \sin i_3 \sin \theta_3 \end{aligned} \quad (4.12)$$

The analysis of the solar third body model again involves term by term integration. Unlike the geopotential expressions, the secularly varying variables do not conveniently appear together in the argument of one trigonometric function per term. Trigonometric identities are employed to expand the variation expressions, and luckily, Mathematica has the capability to perform this

tedious process. Values are needed for $\dot{\lambda}_{sec}$, $\dot{\theta}_{3,sec}$, and $\dot{\Omega}_{sec}$. Calculation of $\dot{\lambda}_{sec}$ is covered in Section 4.2.1. For solar third body, $\dot{\theta}_{3,sec}$ is given by

$$\begin{aligned}\dot{\theta}_{3,sec} &= \dot{\omega}_{3,sec} + \dot{f}_{3,sec} \\ &\approx \dot{f}_{3,sec} \\ &\approx \frac{2\pi}{31557600} \text{ rad/s}\end{aligned}\tag{4.13}$$

where $\dot{\omega}_{3,sec}$ is ignored because it is extremely small [59]. The secular rate of f_3 is an average rate based on one revolution per 365.25 days. The satellite secular node rate is the sum of three components:

$$\dot{\Omega}_{sec} = \dot{\Omega}_{J_2,sec} + \dot{\Omega}_{\odot,sec} + \dot{\Omega}_{\oplus,sec}\tag{4.14}$$

in which

$$\begin{aligned}\dot{\Omega}_{J_2,sec} &= \text{secular variation of } \Omega \text{ due solely to } J_2 \\ \dot{\Omega}_{\odot,sec} &= \text{secular variation of } \Omega \text{ due solely to solar third body} \\ \dot{\Omega}_{\oplus,sec} &= \text{secular variation of } \Omega \text{ due solely to lunar third body}\end{aligned}$$

Again, since J_2 dominates the geopotential, inclusion of the effects of higher zonals is unnecessary. The secular variation due to SRP is also ignored in Equation 4.14 because it is negligible.

4.3.2 Solar Third Body Model Validation

Though the solar model is sound near GEO altitudes, validation is carried out at GEO+30 km to preserve uniformity. Orbital elements and numerical integration specifics for the test case are summarized in Table 4.1. The significant effects of the solar third body perturbations are listed in Table 4.4, from which it can be seen that the agreement between analytical and numerical models is good. Individual effects are discussed next.

The SP variations in semimajor axis are shown in Figure 4.10. Short-periodic effects from solar third body perturbations are generated numerically as the difference between a solar with J_2 model and a J_2 -only model. Hence, the values for the semimajor axis are sometimes negative and are on the order of hundreds of meters. The 12-hour periodic effect is clearly seen over two days. Its

Table 4.4: Significant Periodic Effects from Solar Third Body Perturbations.

	Numerical Amplitude	Analytical Amplitude	Period
Semimajor Axis			
SP	470 m	473 m	12 hr
LP	none		
Eccentricity			
SP	1.45 e-05	2 e-05	24 hr
LP	3.3 e-05	3.3 e-05	6 mo
	1.5 e-04	1.5 e-04	28 yr

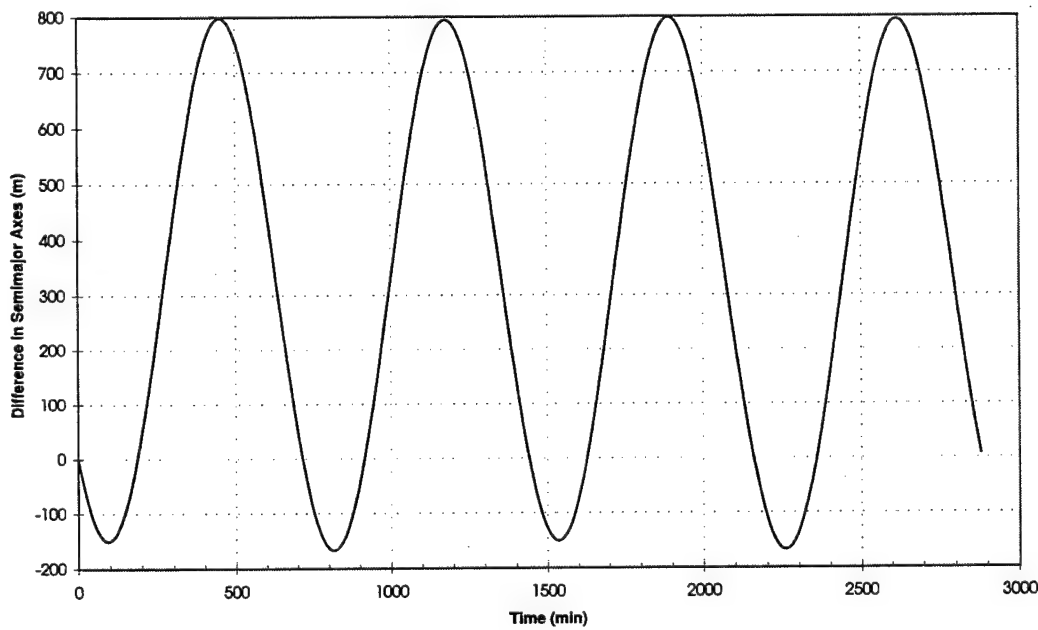


Figure 4.10: Solar Third Body Short-Periodic Variations in Semimajor Axis.

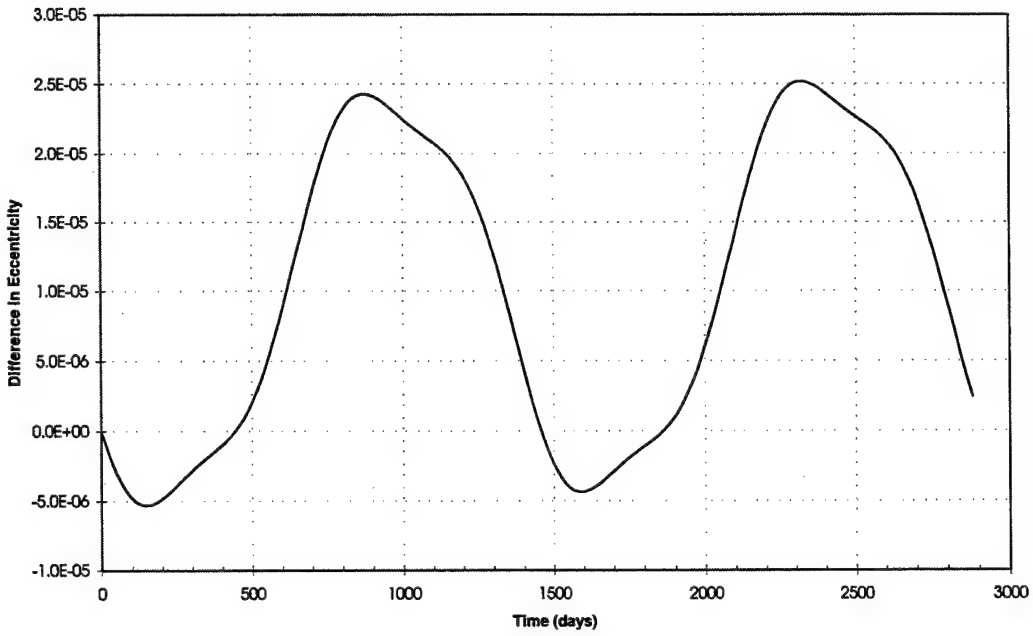


Figure 4.11: Solar Third Body Short-Periodic Variations in Eccentricity.

amplitude is somewhat larger than the SP effects due to geopotential. There are no long-periodic terms for semimajor axis.

For eccentricity, the SP effects are captured in Figure 4.11. Again, some values for eccentricity are negative because the plot shows the difference between two models, as explained in the previous paragraph. The primary effect shown in the figure has a period of about 24 hours. The difference between analytical and numerical amplitudes in Table 4.4 may be due to the location of the third body during numerical integration and the phasing that this introduces between the different components of the terms forming the total amplitude. Finally, Figure 4.12 features the LP variations in eccentricity. This is a DSST AOG plot of a solar plus J_2 model. The plot shows rapid oscillations on top of a larger periodic term. The periods are difficult to estimate, but estimations from the history plot do correlate fairly well with the information from the analytical model. The oscillations are about 6 months in period while the larger variation is estimated to have

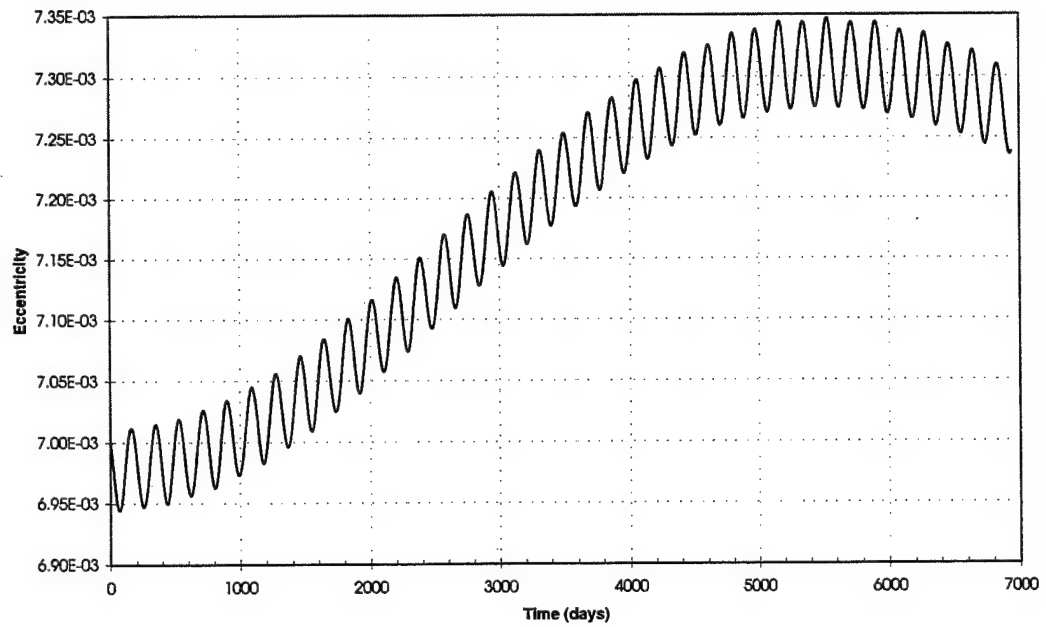


Figure 4.12: Solar Third Body Long-Periodic Variations in Eccentricity.

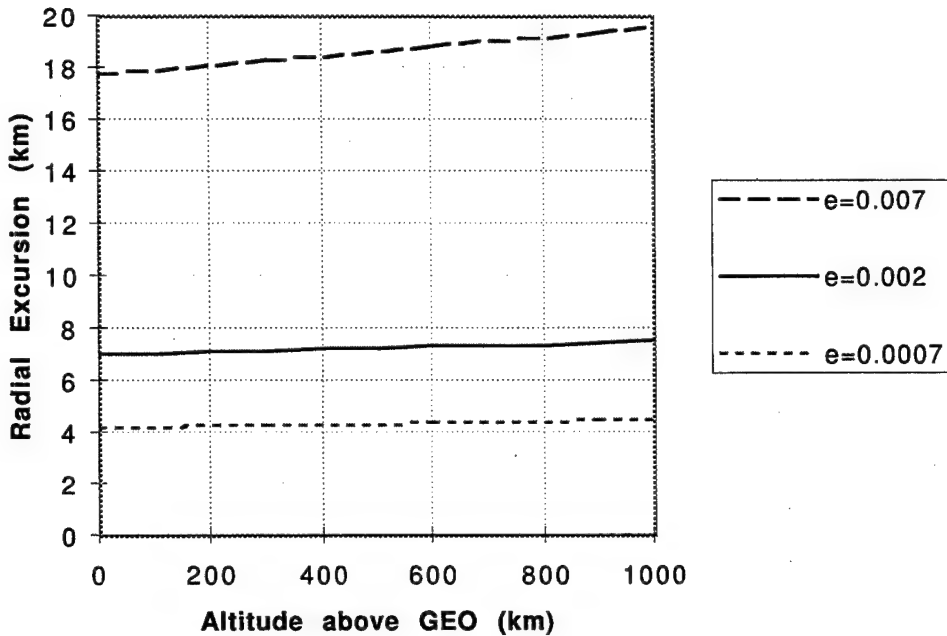


Figure 4.13: Solar Third Body Induced Variations in Radial Direction.

a 28-year period. Future work should examine the possibility of significant inclination-dependent terms. Some eccentricity plots from long propagations suggest that these effects are likely to exist.

4.3.3 Summary of Solar Third Body Perturbation Effects

The solar third body effects as given by the analytical model are shown in Figure 4.13. It is evident that for different values of eccentricity, solar effects vary greatly. The effects increase linearly with altitude in all cases, and the increase is greater with larger eccentricities. Radial excursions are under 20 km in the range of eccentricity and semimajor axis that this study anticipates.

The analytical expressions for the significant terms in the solar third body model are listed in Table 4.5. Periods of the terms are based on the validation case and are shown primarily to relate these expressions to the amplitudes given in Table 4.4. In general, for large eccentricities, beyond the range of Figure 4.13, the eccentricity-dependent long-periodic eccentricity variations are dominant. The short-periodic effects on both semimajor axis and eccentricity are not dependent on eccentricity, and none of these terms are affected by inclination.

Table 4.5: Analytical Expressions for Significant Solar Third Body Terms.

	Term	Period
Semimajor Axis		
SP	$-1.4902 \cdot 10^{-17} a^{5/2} \sin 2\lambda$	12 hr
	$-1.7314 \cdot 10^{-16} a^{5/2} \sin[2(\lambda - \theta_3)]$	12 hr
LP	none	
Eccentricity		
SP	$-3.5119 \cdot 10^{-17} a^{3/2} \cos \lambda$	24 hr
	$-1.3358 \cdot 10^{-16} a^{3/2} \cos(\lambda - 2\theta_3)$	24 hr
	$-3.9659 \cdot 10^{-18} a^{3/2} \cos(\lambda + 2\theta_3)$	24 hr
LP	$1.9074 \cdot 10^{-16} a^{3/2} k \cos 2\theta_3$	6 mo
	$2.1602 \cdot 10^{-16} a^{3/2} h \sin 2\theta_3$	6 mo
	$2.9504 \cdot 10^{-20} a^{3/2} (h \sin 2\Omega - k \cos 2\Omega)$	28 yr

4.4 Lunar Third Body

Analysis of the lunar third body disturbing function closely parallels that of the solar third body model. However, because the lunar orbit is complicated and somewhat eccentric, greater care must be taken in making simplifying assumptions which may exclude important effects. Additionally, the parallax factor is larger in the lunar case, thus forcing the infinite series to be truncated at a larger \mathcal{N} . This results in very large expressions for the potential function and variation equations.

4.4.1 Lunar Third Body Analysis

Like the solar model, there are two infinite series in the lunar disturbing potential for which truncation decisions are needed. The first is the parallax factor. For the lunar model, $\mathcal{N} = 8$. This conclusion is based on DSST built-in truncation algorithms [19, 20]. The j series is again truncated by $|j|_{max} = 2$. Following the method employed in the solar case, this decision rests upon the frequencies appearing in the element history plots from numerical integration and the order of eccentricity desired. From the results, it seems that these truncations are appropriate.

The Moon is assumed to be in a circular orbit. Hence, R_3 is constant. From Reference [55], the mean distance between Earth and the Moon is

$$R_3 = 384400 \text{ km} \quad (4.15)$$

Unlike in the solar case, this assumption is generous, given that the actual eccentricity of the lunar orbit is about 0.0549 [64]. However, handling varying values of R_3 analytically, as dictated by an eccentric orbit, is a difficult matter. Keeping in mind that significant terms can be retrieved later, if missing from the model, this assumption was made. It unfortunately led to the omission of the most significant effect in eccentricity variations. This particular term frustratingly evaded all searches for it in the equinoctial formulation with current treatments of the direction cosines. It was instead found in Kaula's third body model [64] which is in Keplerian orbital elements and was added to this lunar model. The term is a 9.1-year effect due to the lunar argument of perigee rate. The zero satellite inclination and first order eccentricity assumptions do not add further difficulties.

The direction cosines initially employed in the lunar model are given in Equations 4.9. The lunar node has a period of about 6798 days [59], much smaller than the periods of θ_3 and λ , and therefore, is hidden in most terms. The inclination of the Moon with respect to Earth's equatorial plane varies from 18.28° to 28.28° with the same period as that of the node [2]. However, the inclination does not vary secularly and thus was held constant through the analytical integration. The values assigned to lunar node and inclination, 45° and 18.28° , respectively, maximizes the perturbation effects. Once more, θ_3 and the satellite mean longitude λ are the fast variables.

Analytical integration of the lunar third body model follows the procedure described for the solar model. The value for lunar $\dot{\theta}_{3,sec}$ is calculated by the following expression [59] which is similar to Equation 4.13:

$$\begin{aligned}\dot{\theta}_{3,sec} &= \dot{\omega}_{3,sec} + \dot{f}_{3,sec} \\ &\approx \dot{f}_{3,sec} \\ &\approx \frac{2\pi}{2360591.51} \text{ rad/s}\end{aligned}\quad (4.16)$$

Again, $\dot{\omega}_{3,sec}$ is ignored because its period, about 3232 days, is much longer than the true anomaly, about 27.321661 days [59].

4.4.2 Lunar Third Body Model Validation

The orbit for validation purposes is set once more at semimajor axis equal to 42194 km and eccentricity of 0.007. Table 4.6 itemizes the largest effects. Numerical integration employed the option settings detailed in Table 4.1. Generally, the semimajor axis variations correlate much better than those of eccentricity. Long periodics appear only in eccentricity.

Figures 4.14 and 4.15 show the short-periodic variations in semimajor axis and eccentricity, respectively. These plots, like those featuring SP effects in the solar case, depict differences between a lunar with J_2 model and a J_2 -only model. Two periodics are evident in the semimajor axis variations, a large 12-hour effect in combination with a smaller 24-hour periodic. The eccentricity plot shows only 24-hour terms. The discrepancy in the amplitudes of the SP eccentricity variations may be due to position of the Moon, as it represented differently by numerical and analytical models.

Table 4.6: Significant Periodic Effects from Lunar Third Body Perturbations.

	Numerical Amplitude	Analytical Amplitude	Period
Semimajor Axis			
SP	1 km	1.019 km	12 hr and 24 hr
LP	none		
Eccentricity			
SP	3.1 e-05	4.5 e-05	24 hr
LP	3 e-04	2.5 e-04	9.1 yr

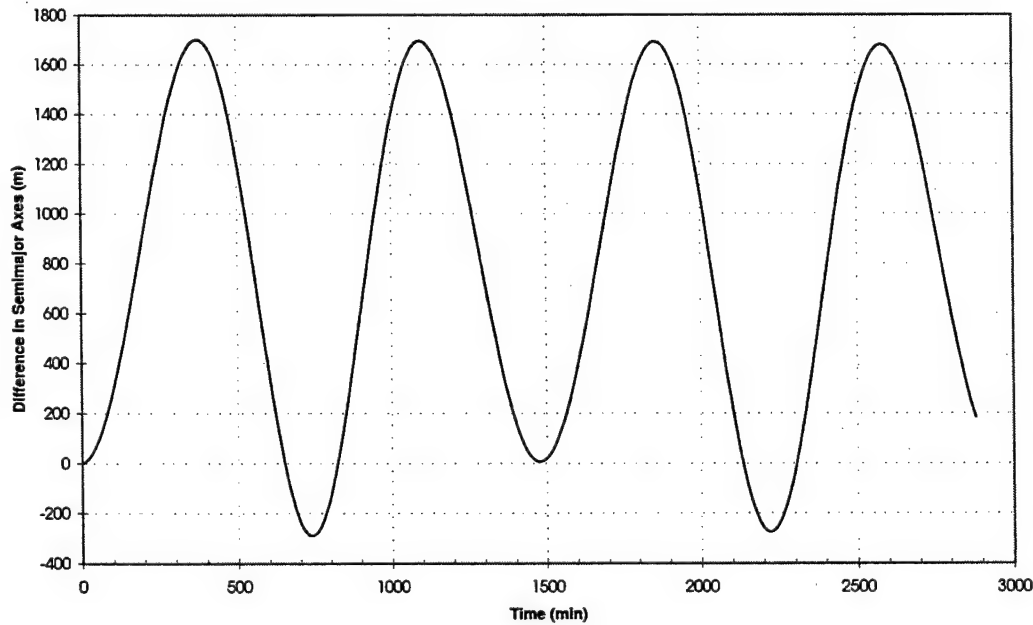


Figure 4.14: Lunar Third Body Short-Periodic Variations in Semimajor Axis.

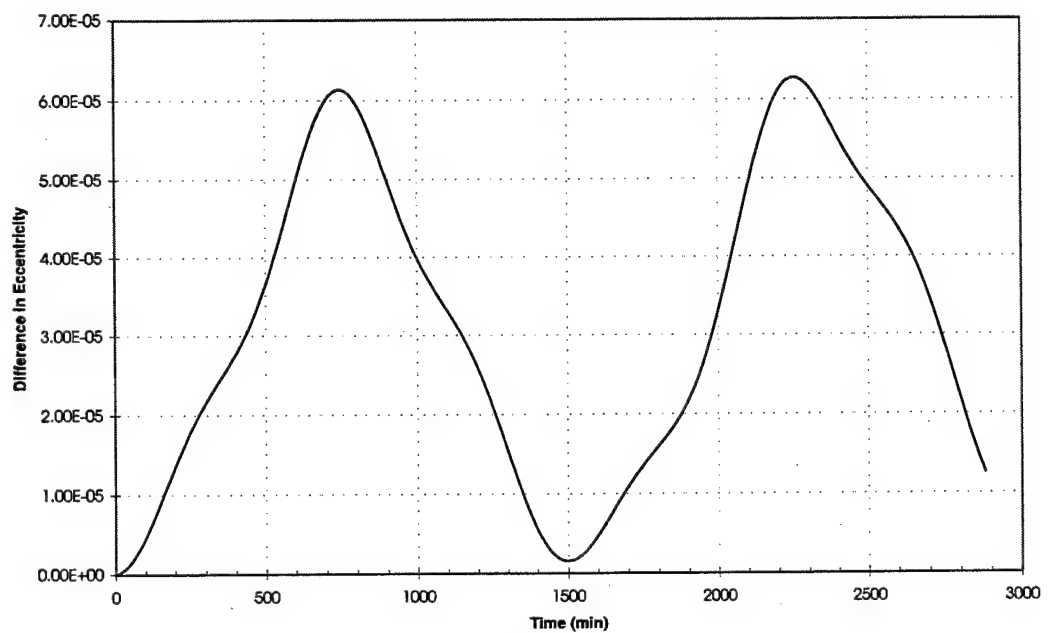


Figure 4.15: Lunar Third Body Short-Periodic Variations in Eccentricity.

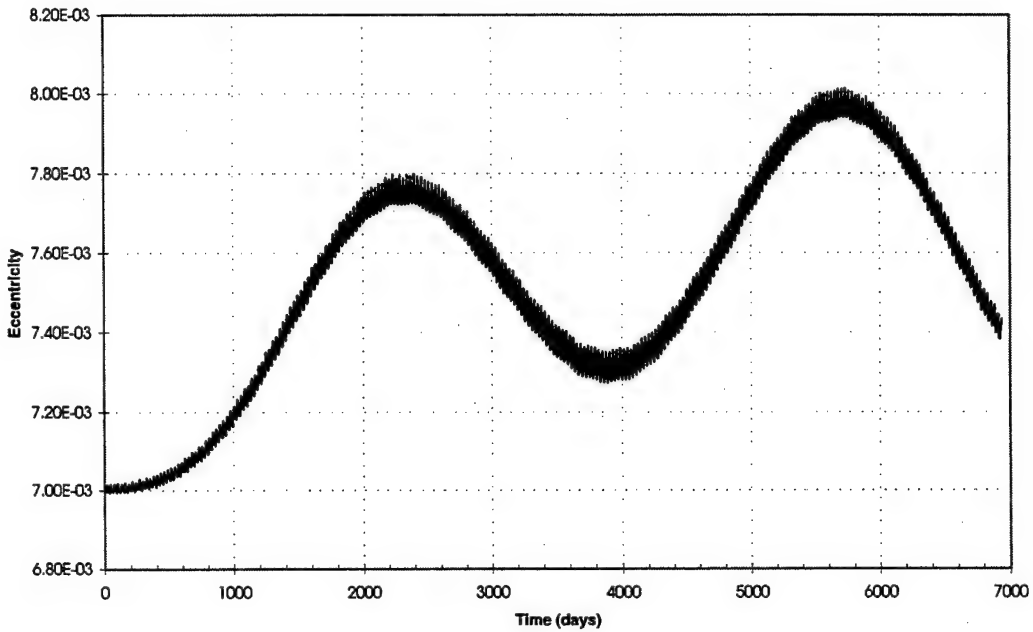


Figure 4.16: Lunar Third Body Long-Periodic Variations in Eccentricity.

Numerical integration employs accurate third body ephemerides, which are directly dependent on the epochs of integrations, while the analytical model fixes the third body in the orientation that results in the largest radial variations. Hence, the analytical model is expected to overestimate and bound the maximum possible variations.

The lunar analytical model is somewhat uncertain in the LP effects on eccentricity. Figure 4.16 is a DSST AOG plot from a lunar plus J_2 model. The 9.1-year variation may be mismodeled in the analytical expressions. The frequency of the analytical term does not quite match that seen in the plot, and there is also a considerable difference in the amplitudes of the numerical and analytical terms. Additionally, a 36-year, long-periodic effect is suggested by the plot; this term is not in the current analytical model. Importantly, however, the bound on eccentricity variations, as determined by the analytical model, is still larger than observed variations. Consequently, the lunar model, while functioning well enough for present purposes, can certainly bear further investigation.

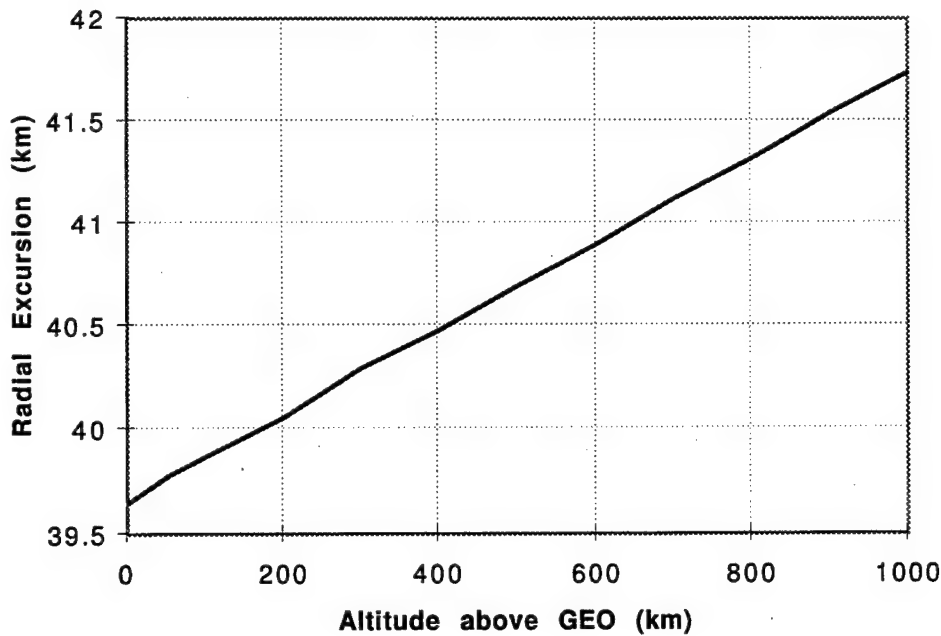


Figure 4.17: Lunar Third Body Induced Variations in Radial Direction.

4.4.3 Summary of Lunar Third Body Perturbation Effects

The lunar third body effects on radial excursion from the analytical model are plotted in Figure 4.17. Radial excursion appears to increase linearly with altitude. In the altitude region of interest in this study, the net result is about 40–42 km. There are no eccentricity nor inclination dependence in the major effects, seen in Table 4.7. Short-periodic terms are numerous. There are dozens of terms with the same order of magnitude, and no one term clearly dominates. The ones listed in Table 4.7 have larger amplitudes for the particular case chosen for validation. There are also instances in which multiple terms of the same frequency with have large amplitudes individually but with opposite signs such that they cancel out one another. Again, the periods listed in the table corresponds to the test case. Lunar effects are, in fact, the largest perturbations aside from deep resonance near GEO and from cases involving large eccentricity or area-to-mass ratios.

Table 4.7: Analytical Expressions for Significant Lunar Third Body Terms.

	Term	Period
	Semimajor Axis	
SP	$4.1015 \cdot 10^{-16} a^{5/2} \cos i_3 \cos \Omega_3 \sin \Omega_3 \cos[2(\theta_3 - \lambda)]$	12 hr
	$2.0508 \cdot 10^{-16} a^{5/2} \cos^2 i_3 \cos \Omega_3 \sin \Omega_3 \cos[2(\theta_3 - \lambda)]$	12 hr
	$1.3337 \cdot 10^{-22} a^{7/2} [\sin \Omega_3 \cos(\theta_3 - \lambda) + \cos \Omega_3 \sin(\theta_3 - \lambda)]$	24 hr
LP	none	
	Eccentricity	
SP	$3.0762 \cdot 10^{-16} a^{3/2} \cos i_3 \cos \Omega_3 \sin \Omega_3 \sin(2\theta_3 - \lambda)$	24 hr
	$45\mu_3 a e_3 / (96nR_3^4) [5(1 - \cos i_3) - (1 + \cos i_3)] \sin \omega_3$	9.1 yr

4.5 Solar Radiation Pressure

The SRP disturbing potential, as noted in Section 3.7, is nearly identical to that of third body perturbations. It is no surprise then that the methodology for SRP analysis is very similar that for solar third body. Unlike the other perturbation models, this one required no patchwork; all significant terms were captured in the basic model.

4.5.1 SRP Analysis

First, in order to obtain a disturbing potential function for SRP, the assumption that the satellite is always sunlit was necessary. For GEO altitudes, this is not unreasonable and will be justified in the next section. The truncation decisions for the infinite series as described in Section 4.3.1 apply here without changes, though the decision for the maximum parallax factor employed is no longer based on truncation algorithms embedded in DSST. The reason for this is that DSST uses a shadow model similar to the Cowell integrator and does not assume that objects are always sunlit. Instead, the maximum parallax factor, $N = 2$, is implemented simply from experience with the solar model.

The perturbing source is again assumed to be in a circular orbit, and so R_3 is constant and equal to the mean distance between Earth and the Sun. The factors comprising the parameter \mathcal{T} , as given in Equation 3.75, are fully adjustable in the SRP model. Default values for validation and application purposes are

$$C_R = 1.2$$

$$A/m = 1 \cdot 10^{-8} \text{ km}^2/\text{kg}$$

$$\mathcal{L}/c = 4.51 \cdot 10^{-3} \text{ kg}/(\text{s}^2\text{km})$$

$$R_3 = 1 \text{ AU}$$

The first order eccentricity and zero satellite inclination assumptions in the variation equations met with no adverse consequences. Similarly, the direction cosines, Equation 4.9, with the values assigned in Equations 4.10 and 4.11, worked well for this model. Finally, analytical integration followed the same lines as the solar third body, and the validation process shows that all significant effects are reflected in this SRP model.

4.5.2 SRP Model Validation

The validation case is the same one used for the other three perturbation models. The significant effects due to SRP are clear-cut, and they are listed in Table 4.8. Correlation between analytical and numerical results are very good. Short-periodic effects are small in semimajor axis and negligible in eccentricity, but agreement between the analytical and numerical model is excellent. Plots for SP variations are unnecessary because of their minimal contribution to overall SRP effects.

Figure 4.18 shows that long-periodic variations in semimajor axis are on the submeter level. The twice-yearly blips in the plot are due to eclipsing effects. This small variation in semimajor axis validates the always-sunlit assumption that enables the formulation of a SRP disturbing potential function. The plot was generated by DSST AOG using a SRP with J_2 model, as was the plot in Figure 4.19 for the LP variations in eccentricity. A simple 1-year effect in eccentricity is captured in this plot. This term represents the only large SRP effect.

Table 4.8: Significant Periodic Effects from SRP Perturbations.

	Numerical Amplitude	Analytical Amplitude	Period
Semimajor Axis			
SP	20 m	20 m	24 hr
LP	none		
Eccentricity			
SP	1 e-08	1 e-08	12 hr
LP	1.165 e-04	1.3 e-04	1 yr

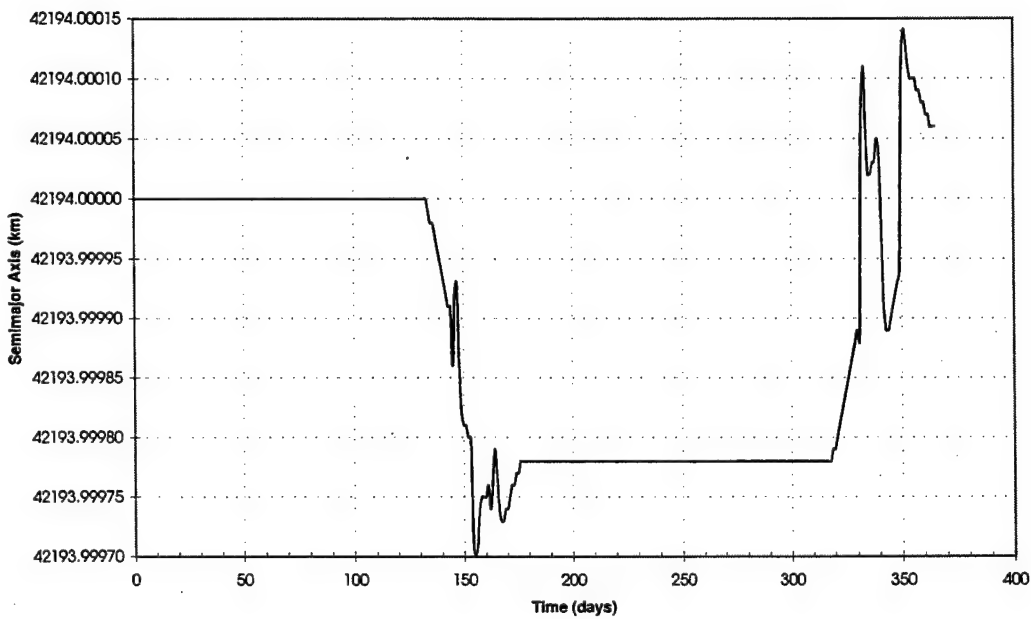


Figure 4.18: SRP Long-Periodic Variations in Semimajor Axis.

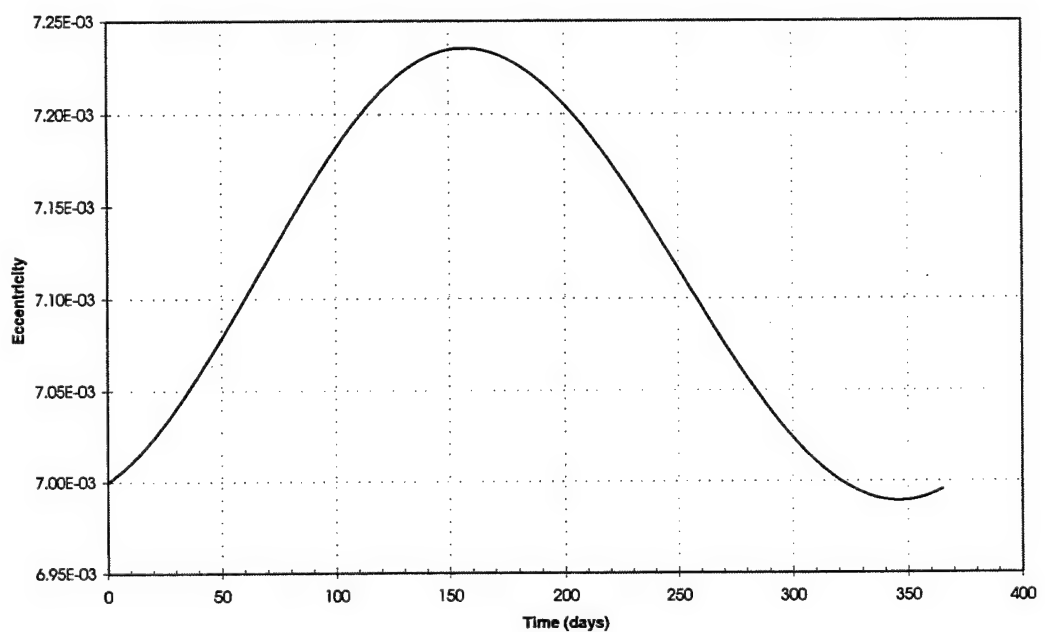


Figure 4.19: SRP Long Periodic Variations in Eccentricity.

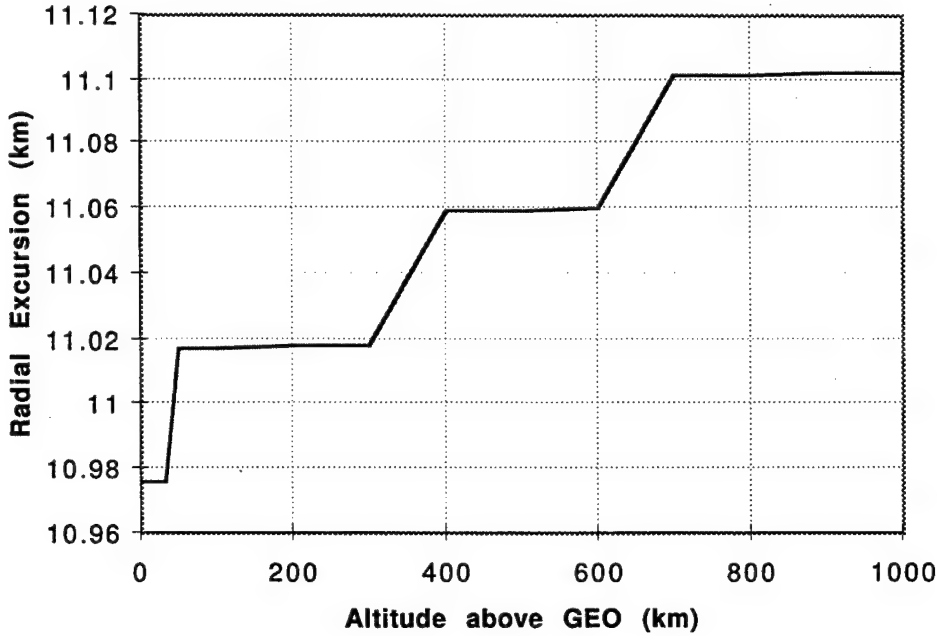


Figure 4.20: SRP Induced Variations in Radial Direction.

4.5.3 Summary of SRP Perturbation Effects

SRP perturbation effects in the radial direction are plotted in Figure 4.20. As noted before, the short-periodic variations are small, in fact accounting for only about 40 m out of total radial excursions on the order of 11 km. The rather interesting curves in the plot are due to manual truncation of the total variations in semimajor axis and eccentricity, as given by the analytical model.

Analytical expressions for the significant terms in the SRP model are included in Table 4.9. The argument of latitude θ_{\odot} of the perturbing body is the same as θ_3 in Section 4.3.1. Likewise, its secular rate is calculated by Equation 4.13. The only large effect, the yearly long periodic in eccentricity, dominates the SRP model. The magnitude of this term is linear with the factor C_{RA}/m . In Figure 4.20, $C_{RA}/m = 1.2 \cdot 10^{-8} \text{ km}^2/\text{kg}$ for which the radial excursion is roughly 11 km. For cases in which this factor is large, SRP could be the most important perturbation effect. None of the significant terms display dependence on eccentricity nor inclination.

Table 4.9: Analytical Expressions for Significant SRP Terms.

	Term	Period
Semimajor Axis		
SP	$1.3571 \cdot 10^{-19} a^{3/2} \mathcal{T} \sin(\lambda - \theta_{\odot})$	24 hr
	$5.8402 \cdot 10^{-21} a^{3/2} \mathcal{T} \sin(\lambda + \theta_{\odot})$	24 hr
LP	none	
Eccentricity		
SP	$-3.3924 \cdot 10^{-20} a^{1/2} \mathcal{T} \cos(2\lambda - \theta_{\odot})$	12 hr
	$-1.4601 \cdot 10^{-21} a^{1/2} \mathcal{T} \cos(2\lambda + \theta_{\odot})$	12 hr
LP	$1.0616 \cdot 10^{-19} a^{1/2} \mathcal{T} \cos \theta_{\odot}$	1 yr

4.6 Cumulative Effects

After studying the individual perturbation models, the combined effects of all perturbation models were investigated. The cumulative effects are based on total variations from each component which are then summed. Figure 4.21 summarizes the cumulative effects on radial excursion over a range of altitudes above GEO. This plot uses the parameters of the test case with zero satellite inclination. It is seen that geopotential perturbations dominate until about GEO+20 km, at which point the lunar effects become the principal player. By GEO+100 km, geopotential effects are the smallest, falling below the SRP curve. The cumulative curve seems to follow the general pattern of the geopotential curve until about GEO+400 km. While geopotential effects continue to decrease, the other perturbation effects are increasing enough to allow the total curve to begin an upward slope.

Numerical integration results for the validation case with all perturbation models turned on are plotted in Figures 4.22 and 4.23 for zero inclination and in Figures 4.24 and 4.25 for 15° inclination over 20 years. The total semimajor axis variation for both inclination cases is about 23 km. The dominant effects, at $a = \text{GEO} + 30$ km, are the resonance terms. For eccentricity, the

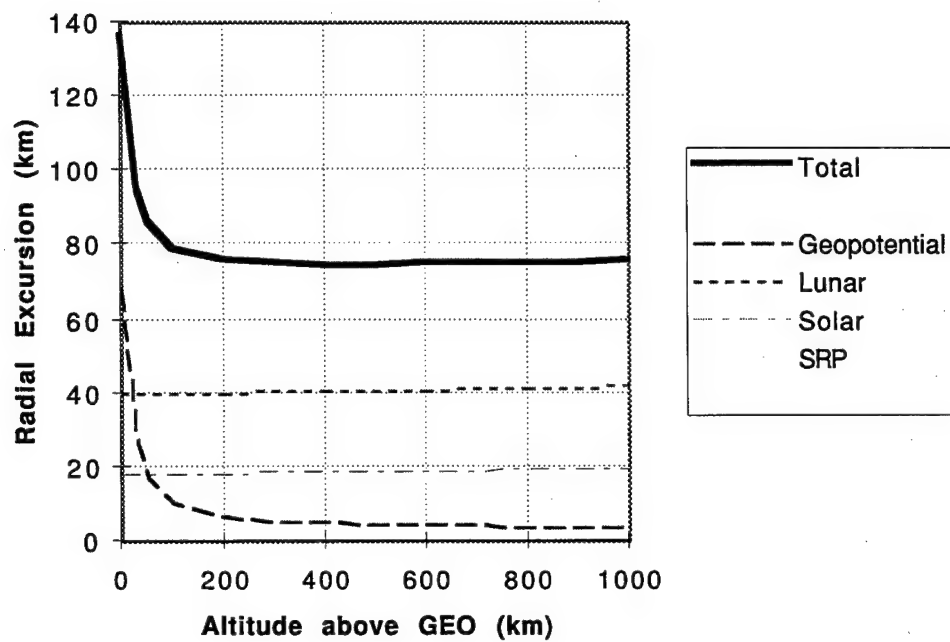


Figure 4.21: Cumulative Effect: Variations in Radial Direction.

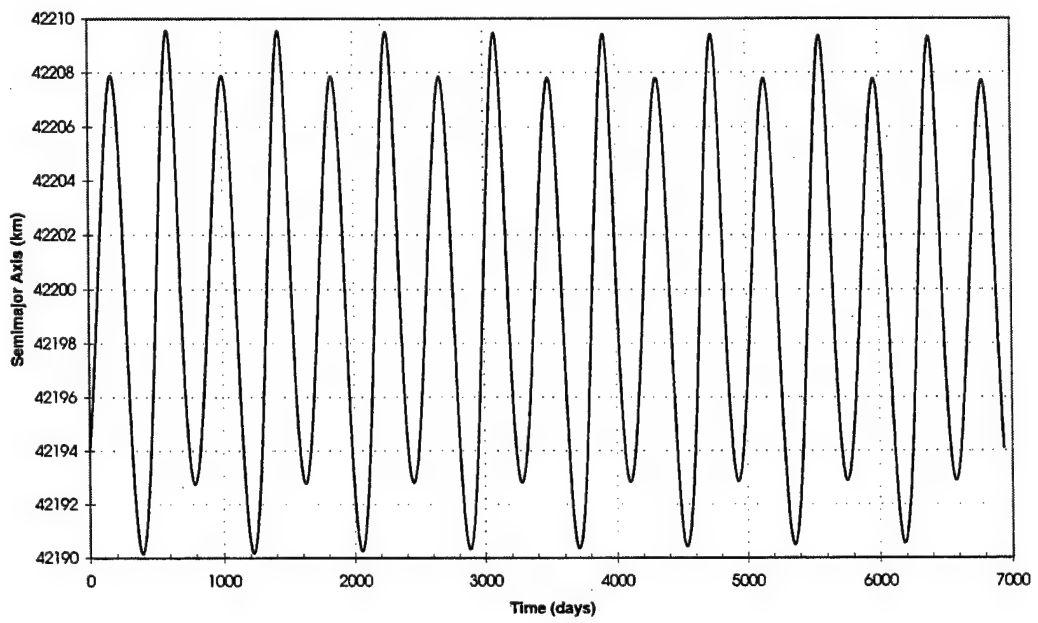


Figure 4.22: Total Perturbation LP Effects in Semimajor Axis at Zero Inclination.

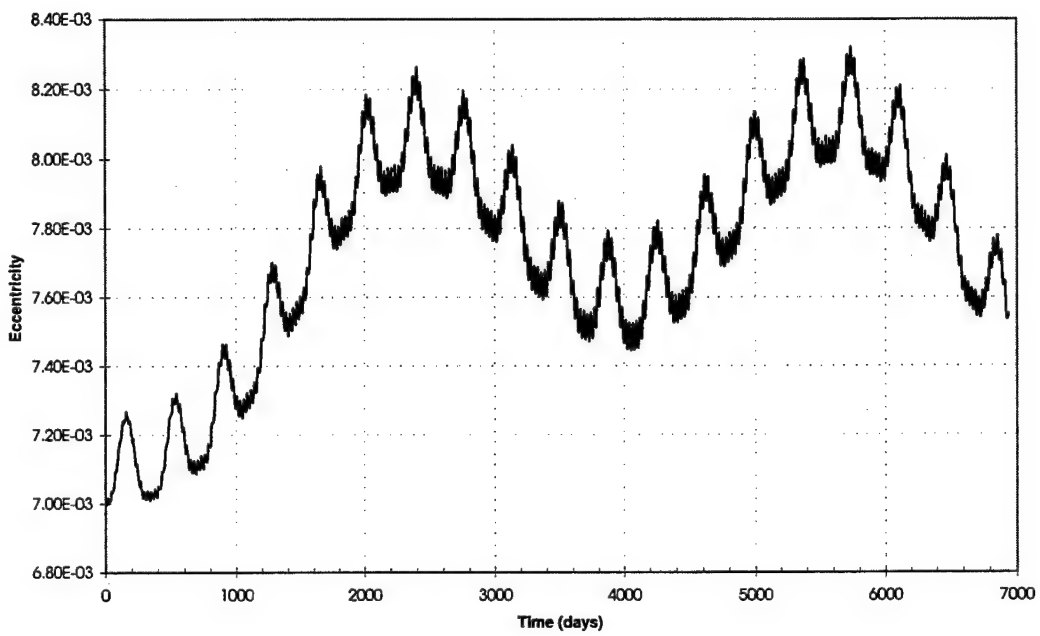


Figure 4.23: Total Perturbation LP Effects in Eccentricity at Zero Inclination.

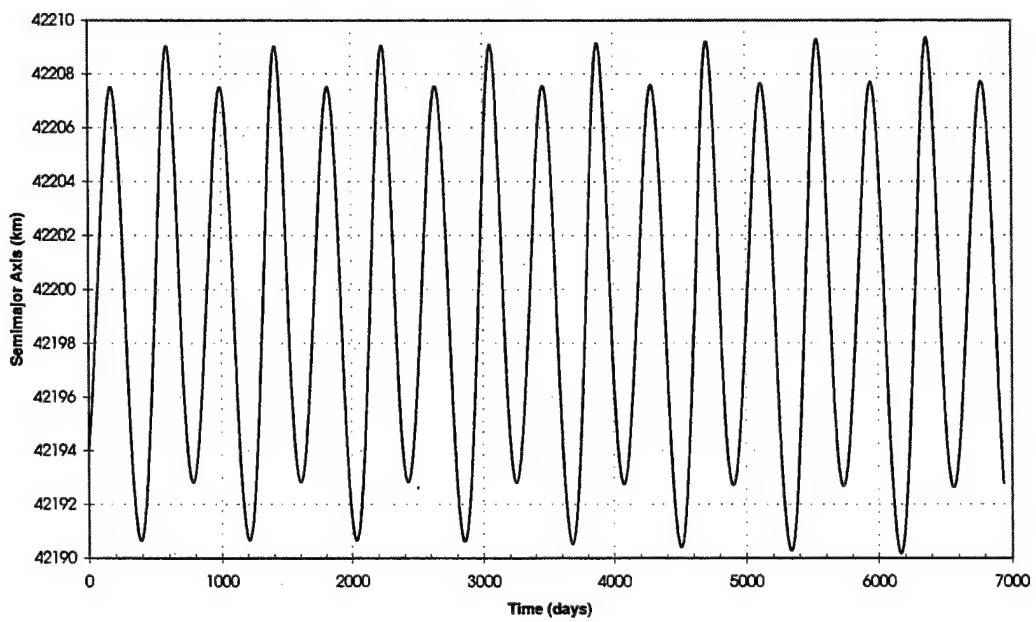


Figure 4.24: Total Perturbation LP Effects in Semimajor Axis at 15 Degrees Inclination.

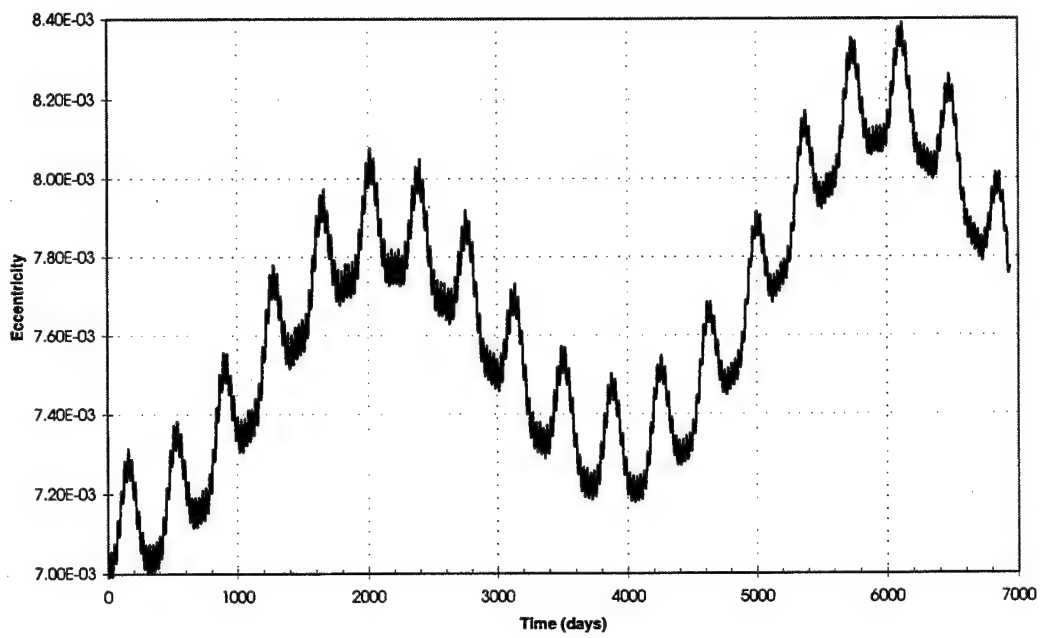


Figure 4.25: Total Perturbation LP Effects in Eccentricity at 15 Degrees Inclination.

Table 4.10: Comparison of Models at Different Altitudes.

Altitude	Numerical	Analytical
GEO	104 km	136 km
GEO+30 km	78 km	95 km
GEO+300 km	67 km	75 km

zero inclination case shows total variations on the order of $1.4 \cdot 10^{-3}$, and $1.55 \cdot 10^{-3}$ for the 15° case, both primarily due to lunar perturbations. These variations result in total radial excursions of no more than 78 km for the zero inclination case and 88 km for the other one. The numbers for radial excursion are estimated from these DSST AOG plots in conjunction with Cowell plots showing SP variations. Total variations are differences between the largest and smallest values on the plots. The analytical model as plotted in Figure 4.21 estimates the total value at 90 km for zero satellite inclination.

Finally, Table 4.10 summarizes the comparison of the analytical against the numerical models at three different altitudes with all four perturbation sources modeled. The quantities are maximum radial excursion for cases with inclinations as large as 15° . As anticipated, the analytical model consistently estimates more conservatively than numerical results. A positive trend is that agreement between the models improves as the altitude increases. The reason for this is unclear. It has been seen that lunar effects dominate at higher altitudes, but this study notes that the analytical model for lunar third body perturbations contains the greatest uncertainty. This seeming paradox is left to future investigations.

Chapter 5

Application to the Reorbiting Problem

The study of collisions in SSO and its attending implications in the determination of the reorbiting distance from GEO requires two tools. One is a breakup model which is described in the next section. The other, a perturbation analysis model, is summarized in Chapters 3 and 4. The application of these tools toward the reorbiting problem is final objective of the research.

5.1 Breakup Model

At the time of this research, a validated breakup model suitable for the GEO regime is not available. However, the purpose of the research is not to build a low-velocity collision model but to study short- and long-term orbital parameters in conjunction with the SSO collisions scenario. Hence, the only alternative is to find a reasonable and available breakup model. Such a model need not be specifically tailored for nonhypervelocity collisions, but the model needs to provide values for the delta-velocity (Δv) imparted to the fragmentation pieces. A value, associated with an average piece, is consequently used to determine the new orbit of that piece. Then the perturbation model is applied, and the region, in terms of radial distance that the representative piece may occupy, is established. The reorbiting problem seeks to control the placement of that region.

The first candidate examined was the statistical breakup model in ODESI, which is described in Section 2.3.1. The environmental model ODESI employed the assumption that the imparted Δv to the collision fragments is equal to the collision velocity, i.e., the relative velocity between the parent objects [43], and this assumption seemed to be a reasonable starting point. It was understood at the outset that this procedure would produce inflated values for Δv . However, after the numbers were calculated, it was clear that this assumption is unacceptable. For instance, a creditable worst case scenario is the collision between one object at near zero inclination and the other at 15° . (Cases of collisions between objects with ascending node 180° apart are not treated in this study because they represent implausible events.) If both objects are assumed to be in circular orbits, the relative velocity is

$$v_{rel} = 0.26105 \sqrt{\frac{\mu}{a}} \quad (5.1)$$

where μ is the gravitational parameter, and a , the semimajor axis, is allowed to vary. Assuming then that the Δv is also given by Equation 5.1 and also that it is applied in plane and at a full 180° from the velocity direction of one of the parent objects, the new semimajor axis and eccentricity of the fragment can be determined. These orbital elements in turn allow for the calculation of the minimal radial distance of the fragment before perturbations affects its orbit. Under these assumptions, a collision occurring at 70,000 km above GEO, produces breakup pieces that cross GEO altitudes. These results are unrealistic due to the large value for imparted Δv .

Another possibility involves somehow scaling the results from a hypervelocity collision model. This may be an abuse of the model as it was not intended for low-speed encounters, but on the flip side, research has not conclusively shown that such models are indeed inappropriate out of the hypervelocity realm. This alternative approach begins with the data generated from the simulation of a collision between a satellite in GEO and a debris piece in geosynchronous transfer orbit [21]. The relative velocity is on the order of 1.4 km/s. This simulation is based on a hypervelocity model, and conservation of mass and energy is confirmed [17]. Subjective approximations from graphed data of the spatial distribution of collision debris provides orbital information for a selected average piece, which is discussed in further detail later. The semimajor axis is estimated, and with the assumption of a full retrograde, in-plane impulse, the orbit is taken as being elliptical

with the apogee height at the GEO parent object's initial altitude. The difference between the velocity of the parent object's circular orbit and the velocity of the fragment at apogee is the Δv imparted by the collision. This is calculated to be 20 m/s. A linear scaling function is employed to adjust the Δv for different impact velocities:

$$\Delta v = \Delta v_{1.4} \frac{v_{rel}}{1.4} \quad (5.2)$$

$$= 0.014286 v_{rel} \quad (5.3)$$

All quantities are in units of km/s.

The average piece chosen for this approach is the median data point in the set of debris pieces whose semimajor axis is smaller than that of the GEO parent object. Since the direction component of imparted Δv is completely random, roughly half of the fragmentation debris are flung in a prograde direction while the rest experience retrograde impulses. The debris size distribution of these two sets should be nearly identical. The relation between debris size and imparted Δv is more complicated. Naturally, the smaller pieces are more likely to experience larger Δv . Therefore, a reasonable claim may be made that, as the chosen piece is a median point, roughly one quarter of the collision fragments will be orbits lower than the representative piece, regardless of the breakup mass distribution, and that these fragments will be the smaller fragments.

With the relation in Equation 5.3, the assumption on the direction of the impulse, and two-body orbital equations, the orbit geometry of the fragment can be calculated for given collision altitudes. For collisions between objects in circular orbits of the same semimajor axis and separated by 15° in inclination, data for varying collision altitudes are presented in Table 5.1. Eccentricity of the fragment in its initial orbit after the breakup is 0.00744 for all reorbiting altitudes, and r_{min} is the minimal radial distance, based on two-body perigee distance. For this study, the collision altitude is taken to be equal to reorbiting altitudes. A more moderate case is summarized in Table 5.2 for collisions between circular orbits separated by 7.5° . The eccentricity of the fragment is smaller, 0.00373, due to the smaller imparted Δv . In both cases, semimajor axis for GEO is 42,164 km.

It is important to note that the minimal radial distances in Tables 5.1 and 5.2 are based only on two-body equations without perturbations effects taken into account. The numbers themselves,

Table 5.1: Data From Collisions Between Objects 15 Degrees Apart.

Reorbiting Altitude [km]	Δv [km/s]	New Orbit of Fragment	
		a [km]	r_{min} [km]
300	0.0114	42150	41836
400	0.0114	42249	41935
500	0.0114	42349	42033
600	0.0114	42448	42132
633	0.0114	42481	42164
700	0.0114	42547	42230
800	0.0114	42647	42329
900	0.0113	42746	42428

Table 5.2: Data From Collisions Between Objects 7.5 Degrees Apart.

Reorbiting Alt [km]	Δv [km/s]	New Orbit of Fragment	
		a [km]	r_{min} [km]
300	0.00573	42306	42148
317	0.00572	42323	42165
400	0.00572	42406	42247
500	0.00571	42505	42347
600	0.00571	42605	42446
700	0.00570	42705	42545

however, are consistent with expectations. It is no surprise that collisions occurring at 300 km above GEO will produce debris that crosses GEO. This breakup model cannot be validated by any available means at this time due to the lack of empirical data. However, a methodology is established such that a different model may be substituted for this one, should it prove to be better. This tool can now be applied in conjunction with the perturbation models to study reorbiting altitudes.

5.2 Reorbiting Altitudes

Six cases were studied in which the definition of the GEO region and the inclination between the colliding objects varied. The GEO region is defined in three ways:

- Case 1: Restricted to GEO altitude, 42,164 km
- Case 2: Covers the region traversed by uncontrolled GEO objects, GEO+104 km
- Case 3: Includes drifting and operational regions and a modest buffer, GEO+200 km

The first case represents the absolutely minimal reorbiting requirement: keeping most debris clear of operational satellites. In reality, functional GEO satellites occupy various altitudes around the GEO altitude, but this case is meant to illustrate an extreme definition of the GEO region. The next case involves a moderate definition. The region occupied by drifting GEO satellites was determined by long-term semianalytical integration, modeling a 4x4 JGM-2 gravity field, lunisolar perturbations, and SRP effects for $A/m = 0.01 \text{ m}^2/\text{kg}$. The last definition for the GEO region is conservative by some standards because it includes a buffer, the value for which is generally not based upon physics or facts but is set by individual estimations.

For each of the three GEO region cases, two collision scenarios are examined. Since uncontrolled objects in the GEO regime generally have inclinations between 0° and 15° , a worst case and a more typical case are studied. The worst case is defined by collisions between objects separated by the full 15° . Recognizing that this is an extreme case and that preventive measures might be geared more toward typical situations, collisions between objects separated by 7.5° in inclination are also surveyed. There are then six distinct cases discussed in the following sections.

Table 5.3: GEO Region Case 1 with Collisions Between Objects 15 Degrees Apart.

GEO region	42164 km	
Before collision		
Semimajor axis	42884 km	
Rerbiting distance	720 km	
After collision		
Semimajor axis	42567 km	
Eccentricity	0.0074447	
Perturbations	Δa [km]	Δe
Geopotential	1.9715	0.0001286
Solar 3rd body	1.0043	0.0004434
Lunar 3rd body	2.4114	0.0009382
SRP	0.0506	0.0003199
Total	5.4378	0.0018601
Min radial distance	42167 km	

5.2.1 15 Degrees Inclination Case

Each definition of the GEO region specifies an altitude that the representative fragment should not dip below. Using the breakup model described in Section 5.1 and the analytical perturbation models developed in this research, the collision altitude, which is also the rerbiting altitude, is adjusted manually until the models show that the fragment will not enter the specified region. A 5 km tolerance is allowed. Tables 5.3, 5.4, and 5.5 summarize the results for the three differently defined GEO regions.

The semimajor axis before the collision is the parameter sought. The rerbiting distance is the difference of this value and 42,164 km. Recall that the breakup model assumes that the parent objects are initially in circular orbits before the collision. The perturbation models uses the semimajor axis and eccentricity calculated by the breakup model and in turn, gives the maximum

Table 5.4: GEO Region Case 2 with Collisions Between Objects 15 Degrees Apart.

GEO region	42268 km	
Before collision		
Semimajor axis	42989 km	
Reorbiting distance	825 km	
After collision		
Semimajor axis	42671 km	
Eccentricity	0.0074447	
Perturbations	Δa [km]	Δe
Geopotential	1.6133	0.0001278
Solar 3rd body	1.0141	0.0004468
Lunar 3rd body	2.4358	0.0009429
SRP	0.0510	0.0003203
Total	5.1143	0.0018379
Min radial distance	42270 km	

Table 5.5: GEO Region Case 3 with Collisions Between Objects 15 Degrees Apart.

GEO region	42364 km	
Before collision		
Semimajor axis	43089 km	
Reorbiting distance	925 km	
After collision		
Semimajor axis	42771 km	
Eccentricity	0.0074447	
Perturbations	Δa [km]	Δe
Geopotential	1.3866	0.0001272
Solar 3rd body	1.0236	0.0004501
Lunar 3rd body	2.4593	0.0009473
SRP	0.0513	0.0003207
Total	4.9208	0.0018453
Min radial distance	42368 km	

variations in semimajor axis, Δa , and in eccentricity, Δe . The minimal radial distance is calculated by

$$r_{min} = (a_{new} - \Delta a)(1 - (e_{new} + \Delta e)) \quad (5.4)$$

where

a_{new} = the fragment's semimajor axis after the collision

e_{new} = the fragment's eccentricity after the collision

This expression is based upon the two-body equation for periapse.

Tables 5.3, 5.4, and 5.5 indicate that the reorbiting distance is largely driven by the Δv from the breakup model. Unfortunately, there is much uncertainty in this model, and therefore, the estimates for reorbiting distance should be treated carefully. Of the perturbation effects, several trends are noted. For all disturbing forces except geopotential, the associated Δa and Δe increase with altitude. The geopotential effects decrease with increasing altitude, as expected from the results in Chapter 4. Increases in reorbiting altitude seem to hold a linear relationship with the varying definitions for the GEO protected region. If some faith is placed in the breakup model, then to protect the barest GEO region, Case 1, current reorbiting guidelines need to be doubled at the least. The economic penalties may not be reasonable.

5.2.2 7.5 Degrees Inclination Case

The same procedure is repeated for the more moderate collision case of 7.5° inclination difference between the objects. Results are given in Tables 5.6, 5.7, and 5.8. As expected, the reorbiting distances are smaller in these cases. However, the least expensive option, Case 1, still requires a reorbiting distance that is 30% larger than the current guidelines of 300 km. Previously noted trends in the models are applicable here as well. Unlike in the extreme cases summarized in Section 5.2.1, the reorbiting requirements shown here may not be considered unreasonable. The most conservative case, for a GEO+200 km protected region, indicates that 590 km may be a sufficient reorbiting distance. AUSSAT at one time suggested reorbiting up to 1110 km above GEO [13].

Table 5.6: GEO Region Case 1 with Collisions Between Objects 7.5 Degrees Apart.

GEO region	42164 km	
Before collision		
Semimajor axis	42554 km	
Reorbiting distance	390 km	
After collision		
Semimajor axis	42396 km	
Eccentricity	0.0037338	
Perturbations	Δa [km]	Δe
Geopotential	3.2381	0.0001293
Solar 3rd body	0.9773	0.0002411
Lunar 3rd body	2.3394	0.0008070
SRP	0.0499	0.0003193
Total	6.6046	0.0014966
Min radial distance	42167 km	

Table 5.7: GEO Region Case 2 with Collisions Between Objects 7.5 Degrees Apart.

GEO region	42268 km	
Before collision		
Semimajor axis	42659 km	
Reorbiting distance	495 km	
After collision		
Semimajor axis	42500 km	
Eccentricity	0.0037338	
Perturbations	Δa [km]	Δe
Geopotential	2.2938	0.0001285
Solar 3rd body	0.9870	0.0002430
Lunar 3rd body	2.3632	0.0008115
SRP	0.0503	0.0003197
Total	5.6943	0.0015027
Min radial distance	42272 km	

Table 5.8: GEO Region Case 3 with Collisions Between Objects 7.5 Degrees Apart.

GEO region	42364 km	
Before collision		
Semimajor axis	42754 km	
Reorbiting distance	590 km	
After collision		
Semimajor axis	42595 km	
Eccentricity	0.0037338	
Perturbations	Δa [km]	Δe
Geopotential	1.8349	0.0001278
Solar 3rd body	0.9958	0.0002447
Lunar 3rd body	2.3850	0.0008157
SRP	0.0506	0.0003200
Total	5.2663	0.001508
Min radial distance	42366 km	

Chapter 6

Conclusions and Future Work

The goal of this research appeared clear-cut at the outset and likewise, the path to achieve it seemed simple at first glance. At the beginning, the target of these studies looked to be a single number, the minimum safe reorbiting distance. Such was the naïveté that optimistically colored early decisions and projections. The low-velocity breakup models available at the time that research began seemed unsuitable, but there was confidence that better models would be ready in the near future. Two years later, an unvalidated model is incorporated into this study. The reorbiting problem, as addressed in Chapter 5, did not have a single number as its answer. Instead, summaries filling six tables attempt to describe different aspects of a situation fraught with many alternatives and uncertainties. This study provides an initial, and perhaps too simplistic, look at the effects of collisions in SSO. Refinement possibilities are numerous.

6.1 Conclusions

This research may be divided into three components, and each are now addressed separately. The first part concerns the perturbation models. Though analytical methods sometime produce unwieldy expressions, the gains include physical insight, and specific information on the relationship between individual effects and orbital parameters, such as semimajor axis, eccentricity, and inclination, and that between effects and physical characteristics of the satellite. Furthermore, the variation expressions are applicable to a whole class of orbits. All of this is unavailable from

numerical methods, except through inference. An additional advantage comes from the ease with which the analytical perturbation model interfaces with the breakup model. Results for the reorbiting problem equaling years of propagation are produced in mere seconds. Amplitudes and frequencies of individual effects are more accurately estimated analytically than through orbital element history plots showing multiple effects enmeshed together.

The results of the model validation demonstrate that the majority of the perturbation effects are accurately captured by the variation equations. Short-periodic terms are generally modeled better in the analytical models since they are better suited to the analytical integration method of holding certain slower-varying quantities constant. On the other hand, some long-term propagations indicate that further investigation into the long-periodic effects is warranted. In spite of this, the results of the analytical models presented in this study do bound all variations over 20-year propagations. In fact, Table 4.10 shows that the analytical models do their best in the currently recommended SSO region in the vicinity of GEO+300 km.

The second component is the breakup model. From the earlier descriptions of the model employed, it is easy to conclude that much of the uncertainty in the reorbiting analysis stems from use of this unvalidated model. While it produced seemingly reasonable numbers, estimating the error bounds is impossible because there is no truth model for comparison. Nonhypervelocity breakup dynamics is a largely unexplored area; the first steps sometimes must be taken on faith. A better model, when it becomes available, can easily be substituted in for the current one.

With the methodology established and given reliable tools, the reorbiting analysis can be accomplished swiftly. Table 6.1 summarizes the reorbiting distance for the six cases examined in Chapter 5. The accuracy of this analysis hinges greatly on the breakup model's accuracy. The reorbiting distance is driven mostly by the collision, with perturbations adding less than 100 km. Since definitions for the desired protected GEO region may vary, the relationship between the GEO region and the reorbiting distance is explored. It appears to be no worse than a linear relation. The importance of the breakup model indicates that future work on the reorbiting problem should focus there. If the results of the current analysis are taken at face value, current reorbiting practices are probably not sufficient to protect the GEO region, any definition of it, in the event

Table 6.1: Summary of Reorbiting Analysis.

Collision Case	GEO Region	Reorbiting Distance
15 Degrees	GEO only	720 km
15 Degrees	GEO+104 km	825 km
15 Degrees	GEO+200 km	925 km
7.5 Degrees	GEO only	390 km
7.5 Degrees	GEO+104 km	495 km
7.5 Degrees	GEO+200 km	590 km

of collisions. Furthermore, the safe reorbiting distances, as calculated in this study, are probably beyond reasonable cost penalties in the 15° cases. The 7.5° cases may also be considered extreme. Current technology may not permit consideration of collisions in SSO.

6.2 Future Work

If the analytical approach is continued, improvements can be made in three particular areas. The first concerns the geopotential and lunar third body models. As stated previously, long-periodic effects on eccentricity are suspected to be missing or mismodeled in the current analytical model. Based on eccentricity histories from semianalytical orbit propagations for the lunar case, effects with very long periods, about 36 years, are present but not included in the current model. The long-periodic term in the geopotential model has notably poor correlation between analytical and semianalytical estimates of the amplitude and frequency. Additionally, nonzero inclination terms are generally ignored, except for a few of the largest terms. Recovery of these terms, perhaps especially in the solar model, would help to refine the perturbation models. Finally, the singularity of the geopotential model near GEO altitudes should be addressed, if only for completeness. The handling of resonance terms which are responsible for this difficulty require a fresh approach. However, the primary issue of this research concerns the SSO region so future investigations need not focus too heavily on perturbations of GEO which has also been studied by many.

A completely numerical approach to perturbation analysis would require longer propagation capabilities in order to view longer periodic effects. To shorten integration times, double averaging theories could provide a great advantage [9]. A numerical study of the reorbiting problem also requires a search algorithm to confirm maximum variation bounds.

There is much room for improvement in the low-speed collision model. A better model would provide typical fragment characteristics, such as average area-to-mass ratios, as well as more accurate mass and velocity distributions. For validation of the model, empirical data from ground tests is essential. On-orbit breakup data would require more sensitive detection capabilities than the current 1-meter diameter limit. Due to the great importance of the breakup model in the reorbiting analysis, emphasis in future work is placed in this area.

Finally, the reorbiting analysis could be improved by incorporating the breakup and perturbation models to form one easy-to-use analysis tool. This in turn can be a part of a comprehensive GEO environmental model. The user would be able to set his own definition of the GEO region, select any combination of perturbation models, and even determine the collision scenario, if information on the orbits of objects predicted for a near-approach is available. Though the analytical perturbation models address general classes of orbits, the breakup model should be able to evaluate specific cases and therefore, be of use in risk assessments as well as debris mitigation studies.

References

- [1] E. A. Ashurkov et al. Protection of the geostationary orbit region against space debris. In *Proceedings of the Second European Conference on Space Debris*, pages 697–698, March 1997.
- [2] Roger R. Bate, Donald D. Mueller, and Jerry E. White. *Fundamentals of Astrodynamics*. Dover Publications, Inc., 1971.
- [3] Richard H. Battin. *An Introduction to the Mathematics and Methods of Astrodynamics*. AIAA Education Series. American Institute of Aeronautics and Astronautics, Inc., Washington, DC, 1987.
- [4] Enrico Beruto et al. Debris shielding development for the Columbus Orbital Facility. In *Proceedings of the Second European Conference on Space Debris*, pages 509–517, March 1997.
- [5] A. G. Bird, J. de Lafontaine, E. van der Wenden, H-J. Guenther, and C. Carnebianca. An investigation into the disposal orbit for geostationary spacecraft. In *Space Dynamics*, pages 65–84. CNES, November 1989.
- [6] P. Cefola. Simplified analytical model for the solar radiation pressure for use in the averaged orbit generator. Intralab Memorandum AOD/SD-020-15Z-PJC, Charles Stark Draper Laboratory, October 1982.
- [7] P. Cefola et al. Precision orbit determination from GPSR navigation solutions. In *AIAA/AAS Astrodynamics Specialist Conference, San Diego, CA*, July 1996. AIAA Paper 96-3605.

- [8] P. J. Cefola. A recursive formulation for the tesseral disturbing function in equinoctial variables. In *AIAA/AAS Astrodynamics Specialist Conference, San Diego, CA*, August 1976. AIAA Paper 76-839.
- [9] P. J. Cefola. The long-term orbital motion of the desynchronized Westar II. In *AAS/AIAA Astrodynamics Specialist Conference, Kalispell, MT*, August 1987. AAS Paper 87-446.
- [10] P. J. Cefola and R. Broucke. On the formulation of the gravitational potential in terms of equinoctial variables. In *AIAA 13th Aerospace Sciences Meeting, Pasadena, CA*, January 1975. AIAA Paper 75-9.
- [11] P. J. Cefola et al. The long-term prediction of artificial satellite orbits. In *AIAA 12th Aerospace Sciences Meeting, Washington, DC*, 1974. AIAA Paper 74-170.
- [12] C. C. Chao. Geosynchronous disposal orbit stability. Technical Report TOR-97(1106)-7, The Aerospace Corporation, El Segundo, CA, September 1997.
- [13] V. A. Chobotov. Disposal of spacecraft at end of life in geosynchronous orbit. *Journal of Spacecraft and Rockets*, 27(4):433–437, July–August 1990.
- [14] Vladimir A. Chobotov. Classification of orbits with regard to collision hazard in space. *Journal of Spacecraft and Rockets*, 20(5):484–490, September–October 1983.
- [15] Vladimir A. Chobotov, editor. *Orbital Mechanics*. AIAA Education Series. American Institute of Aeronautics and Astronautics, Inc., Washington, DC, 1991.
- [16] Sean Kevin Collins. *Long Term Prediction of High Altitude Orbits*. PhD thesis, Massachusetts Institute of Technology, March 1981.
- [17] Richard Crowther, June 1998. Personal communication to author.
- [18] D. A. Danielson et al. Semianalytic Satellite Theory (SST): Mathematical algorithms. Technical Report NPS-MA-94-001, Naval Postgraduate School, 1994.
- [19] D. A. Danielson et al. Semianalytic Satellite Theory. Technical Report NPS-MA-95-002, Naval Postgraduate School, 1995.

[20] D. A. Danielson and C. P. Sagovac. Semianalytic Satellite Theory: Truncation algorithms. In *AAS/AIAA Spaceflight Mechanics Meeting, Albuquerque, NM*, February 1995. AAS Paper 95-225.

[21] J. Dick and R. Crowther. Modelling of satellite breakup and fragment detection. In *Proceedings of the 1994 Space Surveillance Workshop*, volume 1, pages 113–119, April 1994. MIT Lincoln Laboratory, Project Report STK-221.

[22] W. Flury, February 1996. Personal communication to author.

[23] D. J. Fonte and C. Sabol. Optimal DSST input decks for various orbit types. Technical Report PL-TR-95-1072, US Air Force Phillips Laboratory, June 1995.

[24] Daniel J. Fonte, Jr. PC based orbit determination. In *AIAA/AAS Astrodynamics Conference, Scottsdale, AZ*, August 1994. AIAA Paper 94-3776.

[25] Daniel J. Fonte, Jr. et al. Comparison of orbit propagators in the Research and Development Goddard Trajectory Determination System (R & D GTDS)–Part I: Simulated data. *Advances in the Astronautical Sciences*, 90:1949–1966, 1996. AAS Paper 95-431.

[26] Larry Jay Friesen, Albert A. Jackson IV, Herbert A. Zook, and Donald J. Kessler. Analysis of orbital perturbations acting on objects in orbits near geosynchronous earth orbit. *Journal of Geophysical Research*, 97(E3):3845–3863, March 1992.

[27] Larry Jay Friesen, Albert A. Jackson IV, Herbert A. Zook, and Donald J. Kessler. Results in orbital evolution of objects in the geosynchronous region. *Journal of Guidance and Control*, 15(1):263–267, January–February 1992.

[28] Larry Jay Friesen, Donald J. Kessler, and Herbert A. Zook. Reduced debris hazard resulting from a stable inclined geosynchronous orbit. *Advanced Space Research*, 13(8):(8)231–(8)241, July–August 1993.

[29] The International Academy of Astronautics. Position paper on orbital debris. *Acta Astronautica*, 30:167–191, October 1993. Compiled by an Ad hoc Expert Group of the IAA Committee on Safety, Rescue, and Quality.

[30] G. Janin. Log of objects near the geostationary ring, March 1997. Issue 17; Compiled at the European Space Operations Centre.

[31] Nicholas Johnson. Recent satellite fragmentation investigations. *The Orbital Debris Quarterly News*, January 1998.

[32] Nicholas L. Johnson and Darren S. McKnight. *Artificial Space Debris*. Orbit. Krieger Publishing Company, Malabar, FL, 1991.

[33] Ahmed Kamel and Richard Tibbitts. Some useful results on initial node locations for near-equatorial circular satellite orbits. *Celestial Mechanics*, 8:45–73, 1973.

[34] A. Kato. Current status of NASDA Orbital Debris Mitigation Standards. In *Proceedings of the 46th International Astronautical Congress, Oslo, Norway*, October 1995. IAA.-95-IAA.6.5.02.

[35] A. Kato. NASDA Space Debris Mitigation Standard. In *Proceedings of the 47th International Astronautical Congress, Beijing, China*, October 1996. IAF-96-V.6.06.

[36] A. Kato. NASDA Space Debris Mitigation Standard. In *Proceedings of the 34th Session of the Scientific and Technical Subcommittee of the UN COPUOS*, February 1997. Agenda Item 8: Space Debris.

[37] W. Kaula. Development of the lunar and solar disturbing functions for a close satellite. *The Astronomical Journal*, 67(5), June 1962.

[38] William M. Kaula. *Theory of Satellite Geodesy*. Blaisdell Publishing Co. (Ginn and Co.), Waltham, MA, 1966.

[39] Donald J. Kessler. Orbital debris environment. In *Proceedings of the First European Conference on Space Debris*, pages 251–262, April 1993.

- [40] Donald J. Kessler and Burton G. Cour-Palais. Collision frequency of artificial satellites: The creation of a debris belt. *Journal of Geophysical Research*, 83(A6):2637–2646, June 1978.
- [41] Joseph P. Loftus, Jr. Orbital debris issues in geosynchronous orbit. In *Summary Minutes of the NASA/DOD Technical Coordination Workshop on Orbital Debris, Colorado Springs, CO*, pages 188–200, July 1992. Presentation Slides; Summary minutes prepared by Kaman Sciences Corporation.
- [42] Darren S. McKnight and Nicholas Johnson. *Artificial Space Debris: Technical and Policy Issues, A Short Course*. AIAA Professional Studies Series. American Institute of Aeronautics and Astronautics, Inc., Washington, DC, April 1994.
- [43] Roger P. McNamara. *The Investigation of Space Debris Generation and Associated Long-Term Effects in the Geosynchronous Region*. PhD thesis, University of Colorado, 1995.
- [44] P. E. Nacozy and S. S. Dallas. The geopotential in nonsingular orbital elements. *Celestial Mechanics*, 15:453–466, 1977.
- [45] The National Aeronautics and Space Administration. NASA Safety Standard: Guidelines and assessment procedures for limiting orbital debris. Office of Safety and Mission Assurance, Washington, DC, August 1995. NSS 1740.14.
- [46] The National Research Council. *Orbital Debris: A Technical Assessment*. National Academy Press, Washington, DC, 1995.
- [47] The National Research Council. *Protecting the Space Station from Meteoroids and Orbital Debris*. National Academy Press, Washington, DC, 1997.
- [48] B. Neta and D. A. Danielson. R & D GTDS SST: Code flowcharts and input. Technical Report NPS-MA-95-009, Naval Postgraduate School, 1995.
- [49] The Office of Science and Technology Policy. Interagency report on orbital debris, November 1995. Drafted by the National Science and Technology Council, Committee on Transportation Research and Development.

[50] A. F. Pensa, G. E. Powell, E. W. Rork, and R. Sridharan. Debris in geosynchronous orbits. In *AAS/AIAA Space Flight Mechanics Meeting, Austin, Texas*, February 1996. Paper AAS 96-118.

[51] Andrew J. Petro. Techniques for orbital debris control. *Journal of Spacecraft and Rockets*, 29(2):260–263, March-April 1992.

[52] David S. F. Portree and Joseph P. Loftus, Jr. Orbital debris and near-earth environmental management: A chronology. NASA Reference Publication 1320, National Aeronautics and Space Administration, December 1993.

[53] R. J. Proulx and W. D. McClain. Series representations and rational approximations for Hansen coefficients. *Journal of Guidance and Control*, 11(4):313–319, July–August 1988.

[54] R. J. Proulx, W. D. McClain, L. W. Early, and P. J. Cefola. A theory for the short-periodic motion due to the tesseral harmonic gravity field. In *AAS/AIAA Astrodynamics Specialist Conference, Lake Tahoe, NV*, August 1981. AAS Paper 81-180.

[55] John E. Prussing and Bruce A. Conway. *Orbital Mechanics*. Oxford University Press, 1993.

[56] Dietrich Rex, Heiner Klinkrad, and Jörg Bendisch. The ESA Space Debris Mitigation Handbook. In *Proceedings of the Second European Conference on Space Debris*, pages 733–736, March 1997.

[57] Keith A. Ryden and David G. Fearn. End-of-life disposal of satellites using electric propulsion: An aid to mitigation of the space debris problem. In *Proceedings of the 46th International Astronautical Congress, Oslo, Norway*, October 1995. IAF-95-IAA.6.5.04.

[58] Chris Sabol, Richard Burns, and Scott Wallace. Analysis of the Telstar-401/GOES-10 close approach using the Raven telescope. In *AAS/AIAA Space Flight Mechanics Meeting, Monterey, CA*, February 1998. AAS Paper 98-118.

[59] Kenneth Seidelmann. *Explanatory Supplement to the Astronomical Almanac*. University Science Books, Mill Valley, CA, 1992.

- [60] Victor J. Slabinski. INTELSAT spacecraft disposal: Orbit raising considerations. In *Proceedings of the First European Conference on Space Debris*, page 663, April 1993.
- [61] David H. Suddeth. Debris in the geostationary orbit ring, the endless shooting gallery: The necessity for a disposal policy. In *NASA Conference Publication 2360*, pages 349–364, July 1982.
- [62] Jill L. Tabor and John D. Vedder. Long-term evolution of uncontrolled geosynchronous orbits: Orbital debris implications. *The Journal of the Astronautical Sciences*, 40(3):407–418, July–September 1992.
- [63] Paul F. Uhlir. Orbital debris mitigation techniques: Technical, legal, and economic aspects. Special Project SP-016-1992, American Institute of Aeronautics and Astronautics, Inc., 1992.
- [64] David A. Vallado. *Fundamentals of Astrodynamics and Applications*. Space Technology Series. McGraw Hill, 1997.
- [65] Faith Vilas, Michael F. Collins, Paul C. Kramer, G. Dickey Arndt, and Jerry Suddath. Collision warning and avoidance considerations for the space shuttle and space station freedom. In *Proceedings of the AIAA/NASA/DOD Orbital Debris Conference*, April 1990. AIAA Paper 90-1337.
- [66] S. T. Wallace et al. Parallel orbit propagation and the analysis of satellite constellations. In *AAS/AIAA Astrodynamics Specialists Conference, Halifax, Nova Scotia, Canada*, August 1995. AAS Paper 95-428.
- [67] T. Yasaka, T. Hanada, and T. Matsuoka. Model of the geosynchronous debris environment. In *Proceedings of the 47th Congress of the International Astronautical Federation, Beijing, China*, October 1996. IAA-96-IAA.6.3.08.
- [68] Tetsuo Yasaka and Toshiya Hanada. Low velocity impact test and its implications to object accumulation model in GEO. *Advances in the Astronautical Sciences*, 91:1029–1038, 1996. AAS Paper 95-648.

[69] Tetsuo Yasaka and Nobuaki Ishii. Breakup in geostationary orbit: A possible creation of a debris ring. In *Proceedings of the 42nd Congress of the International Astronautical Federation, Montreal, Canada*, October 1991. IAA-91-596.

DISTRIBUTION LIST

AUL/LSE
Bldg 1405 - 600 Chennault Circle
Maxwell AFB, AL 36112-6424 1 cy

DTIC/OCP
8725 John J. Kingman Rd, Suite 0944
Ft Belvoir, VA 22060-6218 2 cys

AFSAA/SAI
1580 Air Force Pentagon
Washington, DC 20330-1580 1 cy

AFRL/PSTL
Kirtland AFB, NM 87117-5776 2 cys

AFRL/PSTP
Kirtland AFB, NM 87117-5776 1 cy

AFRL/VS/Dr Fender
Kirtland AFB, NM 87117-5776 1 cy

AFRL/VSSS/Dr David Spencer
Kirtland AFB, NM 87117-5776 1 cy

AFRL/VSSS/Dr Jesse Leitner
Kirtland AFB, NM 87117-5776 1 cy

AFRL/VSSS/Mr Richard Burns
Kirtland AFB, NM 87117-5776 1 cy

AFRL/VSSS/Dr Chris Sabol
Kirtland AFB, NM 87117-5776 1 cy

AFRL/VSSS/Dr Craig McLaughlin
Kirtland AFB, NM 87117-5776 1 cy

AFRL/VSSS/Capt Scott Carter
Kirtland AFB, NM 87117-5776 1 cy

AFRL/VSSS/Lt Megan Bir
Kirtland AFB, NM 87117-5776 1 cy

Mike Gabor
1831 Wells Branch Pkwy #734
Austin, TX 78728 1 cy

Col Salvatore Alfano
N/SPAN
250 South Peterson Blvd, Ste 116
Peterson AFB, CO 80914-3180 1 cy

Lt Col David Vallado
N/SPAN
250 South Peterson Blvd, Ste 116
Peterson AFB, CO 80914-3180 1 cy

Tim Payne
HQ AFSPC/AE
730 Irwin Ave, Ste 83
Falcon AFB, CO 80912-7383 1 cy

Vladimir Chobotov
The Aerospace Corporation
Mail Code M4-946
2350 E El Segundo Blvd
El Segundo, CA 90245-4691 1 cy

C. C. Chao
The Aerospace Corporation
Mail Code M4-948
2350 E El Segundo Blvd
El Segundo, CA 90245-4691 1 cy

Alan Jenkin
The Aerospace Corporation
Mail Code M4-946
2350 E El Segundo Blvd
El Segundo, CA 90245-4691 1 cy

W. Spencer Campbell
PO Box 9045
Albuquerque, NM 87119 1 cy

Marlon Sorge
PO Box 9045
Albuquerque, NM 87119 1 cy

Paul Cefola
Draper Lab, MS 86
555 Technology Square
Cambridge, MA 02139-3563 1 cy

Ron Proulx
Draper Lab, MS 86
555 Technology Square
Cambridge, MA 02139-3563 1 cy

Wayne McClain
Draper Laboratory
555 Technology Square
Cambridge, MA 02139-3563 1 cy

Nguyen X. Vinh
University of Michigan
3001 FXB
1320 Beal
Ann Arbor, MI 48109-2140 1 cy

Don Danielson
Code MA/Dd
Naval Postgraduate School
Monterey, CA 93943 1 cy

Robert Culp
Aerospace Engineering Sciences
Campus Box 429
Boulder, CO 80309-0429 1 cy

Kira Jorgensen
Colorado Center for Astrodynamics
Campus Box 431
Boulder, CO 80309-0431 1 cy

Ronald Madler
Department of Aerospace Engineering
Embry-Riddle Aeronautical University
3200 Willow Creek Rd
Prescott, AZ 86301-3720 1 cy

Nicholas Johnson
NASA/JSC, SN3
Houston, TX 77058 1 cy

Joseph Loftus
NASA/JSC, SA
Houston, TX 77058

1 cy

Walter Flury
ESOC
Robert-Bosch-Str 5
D-64293 Darmstadt
Germany

1 cy

Dietrich Rex
TU Braunschweig
Hans-Sommer-Str 5
38106 Braunschweig
Germany

1 cy

Frank Schäfer
Ernst-Mach-Institut
Eckerstr 4
D-79104 Freiburg
Germany

1 cy

Toshiya Hanada
Department of Aeronautics and Astronautics
Kyushu University
6-10-1 Hakozaki
Higashi-ku, Fukuoka 812-81
Japan

1 cy

Akira Kato
NASDA
Office of Research and Development
2-1-1 Sengen
Tsukuba-city Ibaraki 305
Japan

1 cy

Yoshinori Arimoto
Communications Research Laboratory
4-2-1 Nukui-kita
Koganei-shi, Tokyo 184
Japan

1 cy

Richard Crowther
DERA Space
Arthur C Clarke Building
Farnborough, Hants GU14 0LX
United Kingdom 1 cy

Hedley Stokes
DERA Space
Arthur C Clarke Building
Farnborough, Hants GU14 0LX
United Kingdom 1 cy

Official Record Copy
AFRL/VSSS/Dr Kim Luu 5 cys